

**Best Available
Copy
for all Pictures**

AD-775 719

MATERIALS PROCESSING OF RARE
EARTH-COBALT PERMANENT MAGNETS

Paul J. Jorgensen, et al

Stanford Research Institute

Prepared for:

Air Force Materials Laboratory
Advanced Research Projects Agency

January 1974

DISTRIBUTED BY:

NTIS

National Technical Information Service
U. S. DEPARTMENT OF COMMERCE
5285 Port Royal Road, Springfield Va. 22151

ACCESSION FOR	
NTIS	White Section <input checked="" type="checkbox"/>
DOC	Ball Section <input type="checkbox"/>
UNANNOUNCED	<input type="checkbox"/>
JUSTIFICATION	
BY	
DISTRIBUTION/AVAILABILITY CODES	
DISC.	AVAIL. '800/07 SPECIAL
A	

NOTICE

When Government drawings, specifications, or other data are used for any purpose other than in connection with a definitely related Government procurement operation, the United States Government thereby incurs no responsibility nor any obligation whatsoever; and the fact that the government may have formulated, furnished, or in any way supplied the said drawings, specifications, or other data, is not to be regarded by implication or otherwise as in any manner licensing the holder or any other person or corporation, or conveying any rights or permission to manufacture, use, or sell any patented invention that may in any way be related thereto.

Copies of this report should not be returned unless return is required by security considerations, contractual obligations, or notice on a specific document.

Unclassified

Security Classification

AD 775 719

DOCUMENT CONTROL DATA - R & D

Security classification of title, body of abstract and indexing annotation must be entered when the overall report is classified

1. ORIGINATING ACTIVITY (Corporate author) Stanford Research Institute 333 Ravenswood Avenue Menlo Park, California 94025		2a. REPORT SECURITY CLASSIFICATION Unclassified	
3. REPORT TITLE MATERIALS PROCESSING OF RARE EARTH-COBALT PERMANENT MAGNETS		2b. GROUP	
4. DESCRIPTIVE NOTES (Type of report and inclusive dates) Final Report			
5. AUTHOR(S) (First name, middle initial, last name) Paul J. Jorgensen Robert W. Bartlett		Reproduced by NATIONAL TECHNICAL INFORMATION SERVICE U S Department of Commerce Springfield VA 22151	
6. REPORT DATE December 1973	7a. TOTAL NO. OF PAGES 142	7b. NO. OF REFS 70	
8a. CONTRACT OR GRANT NO. F33615-70-C-1624	9a. ORIGINATOR'S REPORT NUMBER(S) PYU-8731		
b. PROJECT NO. ARPA Order No. 1617	9b. OTHER REPORT NO(S) (Any other numbers that may be assigned this report) AFML-TR-74-2		
c. Program Code No. OD10	d.		
10. DISTRIBUTION STATEMENT Approved for public release; distribution unlimited.			
11. SUPPLEMENTARY NOTES		12. SPONSORING MILITARY ACTIVITY Air Force Materials Laboratory Wright-Patterson Air Force Base Ohio 45433	
13. ABSTRACT The oxidation of SmCo_5 is an unusual example of selective internal oxidation in which the subscale formed consists of a composite microstructure containing samarium oxide fibers and β -cobalt. The oxide fiber size increases with oxidation temperature, and the orientation of the fibers is generally perpendicular to the subscale-alloy interface. The unusual structure results because of the high concentration of samarium in the intermetallic compound, coupled with a low solubility of samarium in metallic cobalt. Growth of the subscale follows the parabolic oxidation law between 100 and 1125°C. The kinetics are too fast to be explained by lattice diffusion in either the oxide or the cobalt phases, and oxygen diffusion down the cobalt-oxide fiber interface appears to be the rate controlling transport mechanism. The solubility of oxygen in SmCo_5 at 1130°C (sintering temperature) in excess of the 800°C solubility was determined to be 3500 ± 550 ppm. The source of oxygen during sintering is the samarium oxide subscale. Submicron oxide particles precipitate within SmCo_5 grains on cooling from the sintering temperature. Oxidation also causes depletion of samarium and precipitation of $\text{Sm}_2\text{Co}_{17}$ particles within SmCo_5 grains. Both inclusions may be sources of domain wall nucleation. The oxide inclusions can be removed by a thermal aging treatment that collects the oxide into a few large grains outside the SmCo_5 grains by a solution/precipitation mechanism involving grain boundary transport of samarium. The $\text{Sm}_2\text{Co}_{17}$ inclusions are not affected by thermal aging, but they can be prevented from occurring by including excess samarium in the sintered compact, to replenish the			

DD FORM 1 NOV 66 1473

(PAGE 1)

S/N 0101-807-6801

Unclassified

Security Classification

136

Security Classification

14

KEY WORDS

LINK A

LINK D

LINK C

ROLE

WT

NAME	ROLE
1. [Name]	[Role]
2. [Name]	[Role]
3. [Name]	[Role]
4. [Name]	[Role]
5. [Name]	[Role]
6. [Name]	[Role]
7. [Name]	[Role]
8. [Name]	[Role]
9. [Name]	[Role]
10. [Name]	[Role]
11. [Name]	[Role]
12. [Name]	[Role]
13. [Name]	[Role]
14. [Name]	[Role]
15. [Name]	[Role]
16. [Name]	[Role]
17. [Name]	[Role]
18. [Name]	[Role]
19. [Name]	[Role]
20. [Name]	[Role]
21. [Name]	[Role]
22. [Name]	[Role]
23. [Name]	[Role]
24. [Name]	[Role]
25. [Name]	[Role]
26. [Name]	[Role]
27. [Name]	[Role]
28. [Name]	[Role]
29. [Name]	[Role]
30. [Name]	[Role]
31. [Name]	[Role]
32. [Name]	[Role]
33. [Name]	[Role]
34. [Name]	[Role]
35. [Name]	[Role]
36. [Name]	[Role]
37. [Name]	[Role]
38. [Name]	[Role]
39. [Name]	[Role]
40. [Name]	[Role]
41. [Name]	[Role]
42. [Name]	[Role]
43. [Name]	[Role]
44. [Name]	[Role]
45. [Name]	[Role]
46. [Name]	[Role]
47. [Name]	[Role]
48. [Name]	[Role]
49. [Name]	[Role]
50. [Name]	[Role]
51. [Name]	[Role]
52. [Name]	[Role]
53. [Name]	[Role]
54. [Name]	[Role]
55. [Name]	[Role]
56. [Name]	[Role]
57. [Name]	[Role]
58. [Name]	[Role]
59. [Name]	[Role]
60. [Name]	[Role]
61. [Name]	[Role]
62. [Name]	[Role]
63. [Name]	[Role]
64. [Name]	[Role]
65. [Name]	[Role]
66. [Name]	[Role]
67. [Name]	[Role]
68. [Name]	[Role]
69. [Name]	[Role]
70. [Name]	[Role]
71. [Name]	[Role]
72. [Name]	[Role]
73. [Name]	[Role]
74. [Name]	[Role]
75. [Name]	[Role]
76. [Name]	[Role]
77. [Name]	[Role]
78. [Name]	[Role]
79. [Name]	[Role]
80. [Name]	[Role]
81. [Name]	[Role]
82. [Name]	[Role]
83. [Name]	[Role]
84. [Name]	[Role]
85. [Name]	[Role]
86. [Name]	[Role]
87. [Name]	[Role]
88. [Name]	[Role]
89. [Name]	[Role]
90. [Name]	[Role]
91. [Name]	[Role]
92. [Name]	[Role]
93. [Name]	[Role]
94. [Name]	[Role]
95. [Name]	[Role]
96. [Name]	[Role]
97. [Name]	[Role]
98. [Name]	[Role]
99. [Name]	[Role]
100. [Name]	[Role]

WT

ROLE

W T

Phase Diagram

10

Unclassified
Security Classification

(Abstract, concluded)

samarium lost by oxidation. The initial sintering kinetics of stoichiometric SmCo_5 powder containing a samarium-rich sintering addition (60 wt% Sm plus 40 wt% Co) have been investigated as a function of amount of liquid phase, time, temperature, and particle size. The shrinkage as a function of time exhibits the classical three stages of liquid-phase sintering; i.e., rearrangement, solution-precipitation, and solid phase. The rate-controlling step during the solution-precipitation stage corresponds to a phase boundary (solid/liquid) reaction leading to dissolution. Evidence for this conclusion is based on the effect of time, temperature and particle size on the shrinkage kinetics. The solid phase sintering kinetics of SmCo_5 have been investigated as functions of stoichiometry, time and temperature. The shrinkage or densification kinetics are not affected by changes in stoichiometry; therefore no correlation exists between densification kinetics and subsequent magnetic properties. The data obtained indicate that more than one atomic transport process is operative during the solid phase sintering process, and because of this complication, the sintering mechanisms can only be tentatively identified without an assessment of their individual magnitudes. We speculate that the atomic transport process responsible for the solid state sintering of SmCo_5 are grain boundary diffusion and surface diffusion.

MATERIALS PROCESSING OF RARE EARTH COBALT PERMANENT MAGNETS

P. J. Jorgensen
R. W. Bartlett

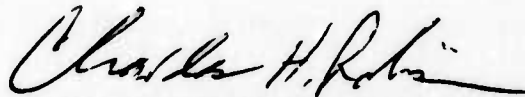
Approved for public release; distribution unlimited.

FOREWORD

This is the final technical report of the research program "Materials Processing of Rare Earth-Cobalt Permanent Magnets" under Contract F33615-70-C-1624. Previous technical reports printed are AFML-TR-71-30, AFML-TR-71-188, AFML-TR-72-47, AFML-TR-72-255, and AFML-TR-73-60. Stanford Research Institute project number is PYU-8731. This project is being conducted by the Materials Laboratory of Stanford Research Institute. Dr. Paul J. Jorgensen, Manager of the Ceramics Group, is the project supervisor. Dr. Robert W. Bartlett of Stanford University is project consultant. The research described in this report is part of the contractual research program of the Electromagnetic Materials Division, Air Force Materials Laboratory, Air Force Systems Command, Wright-Patterson AFB, Ohio. Mr. Harold J. Garrett (AFML/LPE) is the project monitor. It was sponsored by the Advanced Research Project Agency, ARPA Order No. 1617, Program Code No. OD10.

This report covers research conducted between January 1 and September 30, 1974 and was submitted in December 1973.

This technical report has been reviewed and is approved.



CHARLES H. ROBISON, Major, USAF
Chief, Solid State Materials Branch
Electromagnetic Materials Division
Air Force Materials Laboratory

ABSTRACT

The oxidation of SmCo_5 is an unusual example of selective internal oxidation in which the subscale formed consists of a composite microstructure containing samarium oxide fibers and β -cobalt. The oxide fiber size increases with oxidation temperature, and the orientation of the fibers is generally perpendicular to the subscale-alloy interface. The unusual structure results because of the high concentration of samarium in the intermetallic compound, coupled with a low solubility of samarium in metallic cobalt. Growth of the subscale follows the parabolic oxidation law between 100 and 1125°C. The kinetics are too fast to be explained by lattice diffusion in either the oxide or the cobalt phases, and oxygen diffusion down the cobalt-oxide fiber interface appears to be the rate controlling transport mechanism.

The solubility of oxygen in SmCo_5 at 1130°C (sintering temperature) in excess of the 800°C solubility was determined to be 3500 ± 550 ppm. The source of oxygen during sintering is the samarium oxide subscale. Submicron oxide particles precipitate within SmCo_5 grains on cooling from the sintering temperature. Oxidation also causes depletion of samarium and precipitation of $\text{Sm}_2\text{Co}_{17}$ particles within SmCo_5 grains. Both inclusions may be sources of domain wall nucleation. The oxide inclusions can be removed by a thermal aging treatment that collects the oxide into a few large grains outside the SmCo_5 grains by a solution/precipitation mechanism involving grain boundary transport of samarium. The $\text{Sm}_2\text{Co}_{17}$ inclusions are not affected by thermal aging, but they can be prevented from occurring by including excess samarium in the sintered compact, to replenish the samarium lost by oxidation.

The initial sintering kinetics of stoichiometric SmCo_5 powder containing a samarium-rich sintering addition (60 wt% Sm plus 40 wt% Co) have been investigated as a function of amount of liquid phase, time, temperature, and particle size. The shrinkage as a function of time exhibits the classical three stages of liquid-phase sintering; i.e., rearrangement, solution-precipitation, and solid phase.

The rate-controlling step during the solution-precipitation stage corresponds to a phase boundary (solid/liquid) reaction leading to dissolution. Evidence for this conclusion is based on the effect of time, temperature and particle size on the shrinkage kinetics.

The solid phase sintering kinetics of SmCo_5 have been investigated as functions of stoichiometry, time and temperature. The shrinkage or densification kinetics are not affected by changes in stoichiometry; therefore no correlation exists between densification kinetics and subsequent magnetic properties. The data obtained indicate that more than one atomic transport process is operative during the solid phase sintering process, and because of this complication, the sintering mechanisms can only be tentatively identified without an assessment of their individual magnitudes. We speculate that the atomic transport processes responsible for the solid state sintering of SmCo_5 are grain boundary diffusion and surface diffusion.

CONTENTS

I	METHODS OF PREPARATION OF MAGNET POWDERS AND RESULTING PROPERTIES	1
	A. Ball Milling in a Nonreactive Liquid	1
	B. Plasma Spheroidization and Plasma Annealing	5
	1. Plasma Spheroidization	7
	2. Plasma Annealed RECo ₅ Particles	16
	3. Magnetic Properties of Plasma-Treated Particles	17
	C. Electrodeposition	20
	D. Metallothermic Reduction of Alloy Sponge	21
	REFERENCES	24
II	OXIDATION OF RECo ₅	27
	Introduction	27
	Experimental Program	27
	Oxidation Products: Subscale Microstructure and Composition	28
	Kinetics of Internal Oxidation	34
	Discussion of the Oxidation Mechanism	38
	CONCLUSIONS	49
	REFERENCES	50

CONTENTS (Continued)

III	MICROSTRUCTURAL CHANGES IN SmCo_5 CAUSED BY OXYGEN SINTER-ANNEALING AND THERMAL AGING	51
	INTRODUCTION	51
	EXPERIMENTAL	52
	RESULTS	53
	A. Oxide Subscale/ SmCo_5 Reaction at Sintering Tempera- tures	53
	B. Oxygen Solubility and Samarium Oxide Precipitation in SmCo_5	57
	C. Precipitation of $\text{Sm}_2\text{Co}_{17}$ in SmCo_5	64
	DISCUSSION OF Sm_2O_3 AND $\text{Sm}_2\text{Co}_{17}$ INCLUSIONS AND THE INTRINSIC COERCIVITY OF SmCo_5	70
	CONCLUSIONS	73
	REFERENCES	74
IV	LIQUID PHASE SINTERING OF SmCo_5	75
	Introduction	75
	Experimental Procedure and Results	78
	Discussion of Results	86
	Conclusions	92
	REFERENCES	93
V	SOLID-PHASE SINTERING OF SmCo_5	95
	Introduction	95
	Experimental Procedure	97
	Results	100

CONTENTS (Concluded)

Discussion	105
Conclusions	107
REFERENCES	108
VI MATERIALS PROCESSING OF $\text{Sm}_2\text{Co}_{17}$ ALLOYS FOR PERMANENT MAGNETS	109
Introduction	109
Experimental Procedure	109
Results and Discussion	110
Conclusions	112
VII CONTRIBUTION TO THE SAMARIUM COBALT PHASE DIAGRAM . . .	115
REFERENCES	119
APPENDIX -- METHODS OF CHARACTERIZATION OF RARE EARTH COBALT ALLOYS AND MAGNET MATERIALS	121
1. Chemical Analysis of Rare Earth, Cobalt, and Rare Earth-Cobalt Alloys	121
a. Reagents	121
b. Procedure	122
c. Calculations	122
2. Procedure for Producing Magnetometer Test Specimens of Powders	123

LIST OF ILLUSTRATIONS

Section I

METHODS OF PREPARATION OF MAGNET POWDERS AND RESULTING PROPERTIES

1.	Magnetization Curve for Sintered SmCo_5 --Specimen SL-51 . . .	4
2.	Argon Jet Particle Dispenser	6
3.	Scanning Electron Micrographs Before and After Plasma Spheroidization of SmCo_5	8
4.	Spheroidized SmCo_5 in Section (Bright Field)	9
5.	Metallographic Cross Section of Spheroidized Sm-Co Alloy Particles (Primarily SmCo_5)	10
6.	Variation in Praseodymium Content of Spheroidized Particles From Melt 22; 32.4% Pr	15
7.	Ball Milled SmCo_5 Alloy Particles Reduced by Calcium	25

Section II

OXIDATION OF RECo_5

8.	Fibrous Structure of Samarium Oxide in the Oxide/Cobalt Composite Subscale Grown at 1125°C	29
9.	Subscale/ SmCo_5 Interface and Intersecting "Grains" Within the Subscale Structure	31
10.	Porosity in the Oxide Scale Resulting From Oxidation of SmCo_5 (SEM)	33
11.	Parabolic Kinetics of the Selective Internal Oxidation of SmCo_5 in Air	35
12.	Arrhenius Plot for the Internal Oxidation Rate	36

ILLUSTRATIONS (Continued)

13.	Arrhenius Plot for the Internal Oxidation Rate Extended to Lower Temperatures	39
14.	Oxygen Depleted Gap Between the Original Subscale Grown on SmCo_5 and the Samarium-Rich Alloy	43
15.	Subscale Thickness as a Function of Oxygen Content and Particle Diameter in SmCo_5 Magnet Powder	48

Section III

MICROSTRUCTURAL CHANGES IN SmCo_5 CAUSED BY OXYGEN, SINTERING, AND AGING AT INTERMEDIATE TEMPERATURES

16.	Scanning Electron Micrograph of the Subscale/ SmCo_5 Interface; Oxidized 1125°C , 2 min; etched 50 HNO_3 , 30 H_2SO_4 , 20 H_2O	54
17.	Boundary of the Oxide Depleted Zone (Right Side) Within the Subscale After Annealing at 1125°C	55
18.	Samarium-Cobalt Phase Diagram After Buschow and Van Der Goot (5)	56
19.	Boundary Between the Oxide Depleted Zone and the SmCo_5 Core	58
20.	Oxide Precipitates in the SmCo_5 Grains After Oxygen Saturation at 1125°C and Aging at 800°C	60
21.	SmCo_5 Quenched From 1125°C to Room Temperature in Argon--Showing Small Scale Oxide Inclusions	62
22.	Polished Section of a Commercial SmCo_5 Powder Magnet Sintered with Excess Samarium	63
23.	Samarium Oxide Particles in a Sintered SmCo_5 Magnet Exposed by Etching (SEM)	65
24.	Scanning Electron Micrograph of $\text{Sm}_2\text{Co}_{17}$ Precipitates in SmCo_5	65

ILLUSTRATIONS (Continued)

25. SmCo_5 Quenched from 1125°C to Room Temperature and Aged at 800°C --Showing $\text{Sm}_2\text{Co}_{17}$ Inclusions 68

Section IV

LIQUID PHASE SINTERING OF SmCo_5

26. Isothermal Time Dependence of Shrinkage of SmCo_5 Compacts at 1123°C 79
27. Corrected Isothermal Time Dependence of Shrinkage of SmCo_5 Compacts at Several Temperatures for only the Solution-Precipitation Stage of Sintering Using 1.5 wt% Liquid Phase 80
28. Corrected Isothermal Time Dependence of Shrinkage of SmCo_5 Compacts at Several Temperatures for only the Solution-Precipitation Stage of Sintering Using 1.5 wt% Liquid Phase 81
29. Shrinkage Isotherms of SmCo_5 for only the Solution-Precipitation Stage of Sintering using 11.8 wt% Liquid Phase 82
30. SmCo_5 Shrinkage Data obtained at 1120°C using 13.8 wt% Liquid Phase, and an Average Particle Size of $7.4\ \mu\text{m}$. . . 83
31. Shrinkage Isotherms for 11.8 wt% Liquid Phase and an Average Particle Size of $19.6\ \mu\text{m}$ 84
32. SmCo_5 Shrinkage Isotherms for 11.8 wt% Liquid Phase and an Average Particle Size of $19.6\ \mu\text{m}$ 85
33. Arrhenius Plot of the Shrinkage Rate Versus Reciprocal Temperature 87
34. Plot of the Sintering Rate of SmCo_5 Versus the Grain Size at a Temperature of 1123°C 91

ILLUSTRATIONS (Concluded)

Section V

SOLID PHASE SINTERING OF SmCo_5

35.	Linear Thermal Expansion of Polycrystalline Randomly Oriented SmCo_5	99
36.	Samarium-Cobalt Shrinkage Isotherms for an Alloy Containing 29.3 wt% Sm	101
37.	Samarium-Cobalt Shrinkage Isotherms for an Alloy Containing 32.9 wt% Sm	102
38.	Samarium-Cobalt Shrinkage Isotherms for Alloys Containing 34.3 and 34.8 wt% Sm	103
39.	Arrhenius Plot of the Shrinkage Rate Versus Reciprocal Temperature	104
40.	Photograph of Neck Region of SmCo_5 Particles Sintered at 1000 C	106

Section VI I

CONTRIBUTION TO THE SAMARIUM COBALT PHASE DIAGRAM

41.	Samarium-Cobalt Phase Diagram	117
-----	---	-----

LIST OF TABLES

Section I

METHODS OF PREPARATION OF MAGNET POWDERS AND RESULTING PROPERTIES

I	Semiquantitative Analysis of Initial and Spheroidized SmCo ₅ - Run 7 (wt%)	12
II	Magnetic Properties of Plasma Spheroidized and Plasma Annealed Powder	18
III	Magnetic Properties of Sintered Magnets Fabricated from Plasma Spheroidized and Plasma Annealed Materials	19

Section III

MICROSTRUCTURAL CHANGES IN SmCo₅ CAUSED BY OXYGEN, SINTERING AND AGING AT INTERMEDIATE TEMPERATURES

IV	Some Effects Involving Magnetic Coercivity in SmCo ₅ and Their Possible Causes	72
----	--	----

Section IV

LIQUID PHASE SINTERING OF SmCo₅

V	Typical Shrinkage Isotherm Exponents	88
VI	Sintering Model Particle Size Dependence	89

Section V

SOLID PHASE SINTERING OF SmCo₅

VII	Sintering Constants for Equation (4)	96
-----	--	----

LIST OF TABLES (Concluded)

Section VI

MATERIALS PROCESSING OF $\text{Sm}_2\text{Co}_{17}$ ALLOYS
FOR PERMANENT MAGNETS

VIII	Intrinsic Coercive Force of As Ground Powders	111
IX	Intrinsic Coercive Force of Sintered $\text{Sm}_2\text{Co}_{17}$ Magnets . . .	113
X	Intrinsic Coercive Force of Annealed $\text{Sm}_2\text{Co}_{17}$ Magnets . . .	114

I METHODS OF PREPARATION OF MAGNET POWDERS AND RESULTING PROPERTIES

The RECo_5 intermetallic compounds, where RE stands for one of the light rare earths, show a high magnetic saturation and very high magnetocrystalline anisotropy. These properties make them promising materials for fabricating permanent magnets from fine particles by powder pressing and sintering techniques. Although these materials show attractive magnetic properties, coercivities of fine particles have usually been far short of the theoretical potential and are extremely sensitive to particle preparation and subsequent treatment. Successful RECo_5 magnetic particles have previously been produced only by jet milling of arc melted alloys.

During the present program, alternative materials processing techniques were investigated in an effort to develop improved powder preparation methods. The methods investigated were (1) ball milling in a nonreactive liquid, (2) plasma spheroidization of alloy particles, (3) plasma annealing without melting alloy particles, (4) electrodeposition of rare earth-cobalt alloys, and (5) metallothermic reduction of rare earth-cobalt alloys. The primary material used in this study was SmCo_5 but studies were also made on PrCo_5 and MMCo_5 containing major amounts of cerium. *Details of ball milling of SmCo_5 are discussed in detail.*

A. Ball Milling in a Nonreactive Liquid

All starting alloys were made by melting 99.99% cobalt and a pure form of the rare earth (distilled samarium) in a copper hearth furnace under titanium-gettered helium. Compositions were adjusted empirically to account for samarium loss by vaporization. Alloy button sizes were

typically 100 grams. The buttons were annealed at 1100°C in argon and crushed to approximately -30 mesh. In some instances, after blending, the crushed alloy was remelted to improve homogeneity.

Steel mills with steel balls were used for grinding the rare earth-cobalt alloys using hexane as a milling fluid. The hexane was stored in contact with sodium, and the ball mills were loaded in an argon-filled glove box to inhibit oxidation during grinding. (Ceramic mills and alumina grinding balls cause alumina contamination of the alloys.)

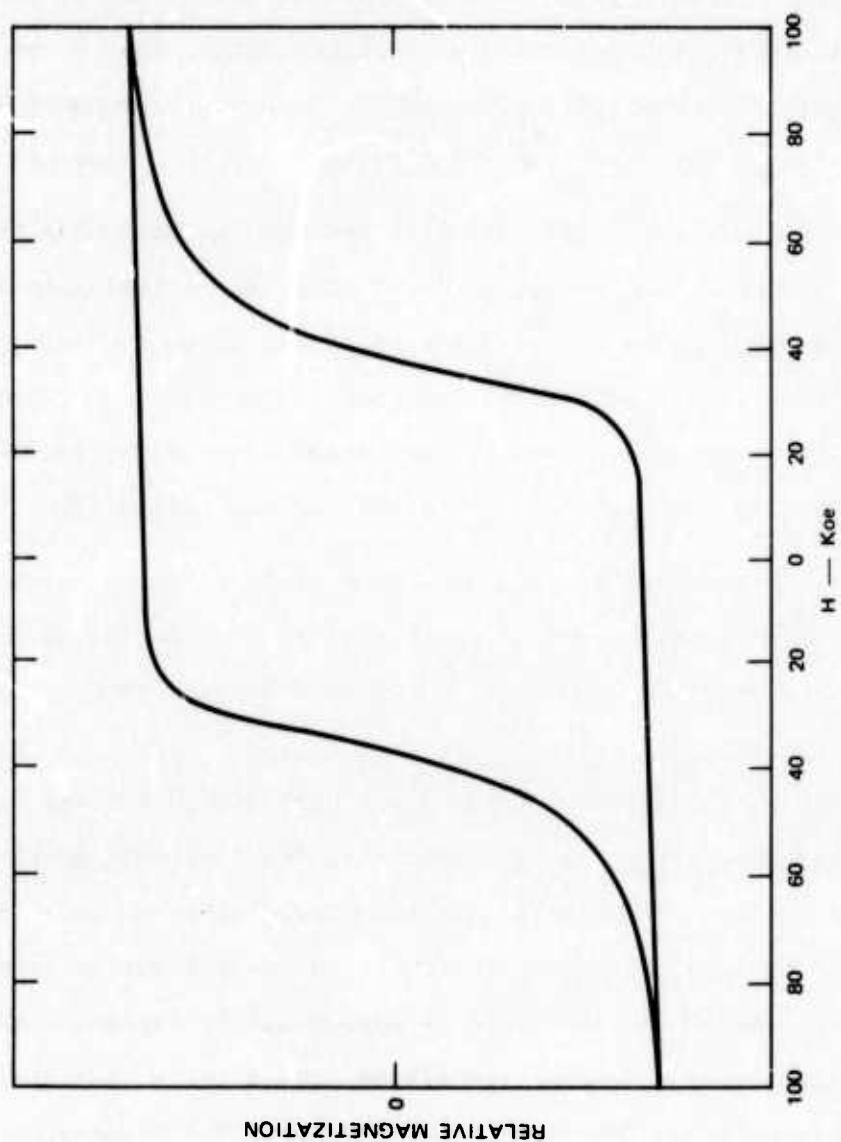
Ball milling is capable of producing SmCo_5 particles with intrinsic coercivities in excess of 20,000 oersteds with good batch-to-batch reproducibility. Only one out of ten ball mill runs on ten separate alloy melts yielded powder with an intrinsic coercivity below 20,000 Oe, and the coercivity of that powder was 18,400 Oe. It is apparent that ball-milled powders, and therefore mechanically stressed particles, can have consistently high coercivities. Exposure in air for 6 days at room temperature did not degrade the coercivity of ball-milled powders tested. However, high temperature annealing in air or under attainable vacuum is deleterious. For example, heating a powder with an intrinsic coercivity of 21,000 Oe in a calcium gettered vacuum to 700°C lowered the intrinsic coercivity to 1500 Oe. It is apparent that either the thermal treatment itself or very small amounts of residual gas have a drastic effect on the nucleation of new domains in this material.

The effect of particle size on the intrinsic coercivity of ball-milled SmCo_5 and PrCo_5 powders was studied. Ball milling SmCo_5 for three hours after crushing to pass a 30-mesh screen yields particles having an average particle size of 4 to 5 μm and an average intrinsic coercive force of 22,000 Oe. Increasing the milling time to ten hours decreased the particle size to 2 to 3 μm and raised the intrinsic coercivity to 26,000 Oe. The average sizes were determined using a Fisher sub-sieve analyzer.

Ball milled PrCo_5 shows a lower intrinsic coercivity when milled 10 hours (2 to 3 μm) than when milled only 3 hours (about 5 μm). This overgrinding effect for PrCo_5 is substantially in agreement with the results using jet milling that have been reported by Strnat and coworkers¹ and by Becker.² However, the reduction in coercivity may be caused by further surface reaction as grinding proceeds rather than by mechanical stress. Intrinsic coercivities obtained with powders produced by ball milling depend on the care taken to eliminate oxygen during grinding.

The magnetic results obtained with sintered magnets made from ball-milled powders show that intrinsic coercivity can be increased during sintering, provided that a samarium-rich liquid phase sintering aid is used. The sintering procedure is outlined in the Appendix. The sintering aid was a 60% samarium-40% cobalt alloy which was ball milled 6 hours and then added to -30 mesh SmCo_5 prior to further ball milling.

Magnetic hysteresis loops measured on sintered magnets fabricated from ball milled powders were often asymmetric when subjected to a magnetizing field of 64 kG. However, a 100 kG field appeared to saturate these samples, and the hysteresis loops were symmetrical. A typical hysteresis loop of a sintered magnet from ball milled powders is shown in Figure 1. For this particular specimen, the intrinsic coercive force is 37,000 Oe. The highest value obtained for a sintered SmCo_5 magnet produced in our laboratory using ball milled powders was an intrinsic coercive force of 43,000 Oe. This is approximately twice the values of the intrinsic coercive forces typically measured for ball-milled powders prior to sintering, 20,000 to 25,000 Oe. The magnet temperature during this measurement was approximately 235^o K.



TA-8731-46

FIGURE 1 MAGNETIZATION CURVE FOR SINTERED SmCo_5 —SPECIMEN SL-51

B. Plasma Spheroidization and Plasma Annealing

Interest in spheroidization of magnet particles stemmed from the possibility that fracture stresses during grinding were inducing imperfections into magnet particles that were sources of heterogeneous nucleation of reverse domains, and hence lowered coercive force. Jagged edges on a fractured particle were also considered to be possible sources of easy domain nucleation.

Quenching liquid droplets in an inert atmosphere is usually a simple and effective method for generating fine spherical particles. The liquidus temperatures of the rare earth-cobalt materials of interest are near 1200°C , which is not an excessive temperature for metal spheroidization. To some extent, plasma heating avoids the problem of contamination that results when chemical flame heating is employed. Particles suspended in a plasma can be melted and quenched without agglomeration, and heat transfer to the particles is very rapid because of the high plasma temperatures. Although it is comparatively easy to melt SmCo_5 in a plasma environment, the high vapor pressure of samarium causes some of the samarium to be vaporized from the droplet.

An arc jet plasma was used for the spheroidization and plasma annealing studies. This apparatus included a four-foot quenching chamber and a 40 kW power supply. A schematic drawing of the apparatus is shown in Figure 2. Argon passed over hot calcium chips was used for both the plasma and carrier gas used to inject particles into the plasma. The feed particles were ball-milled particles which entered the plasma from a screw feeder and gas jet particle disperser. Particles were introduced normal to the plasma flow direction. Fortunately, agglomeration of the magnetic particles on leaving the jet disperser prior to entering the plasma was not a serious problem. The sensible heat that the particles acquired would be controlled within a limited range by varying the power level and point of particle injection.

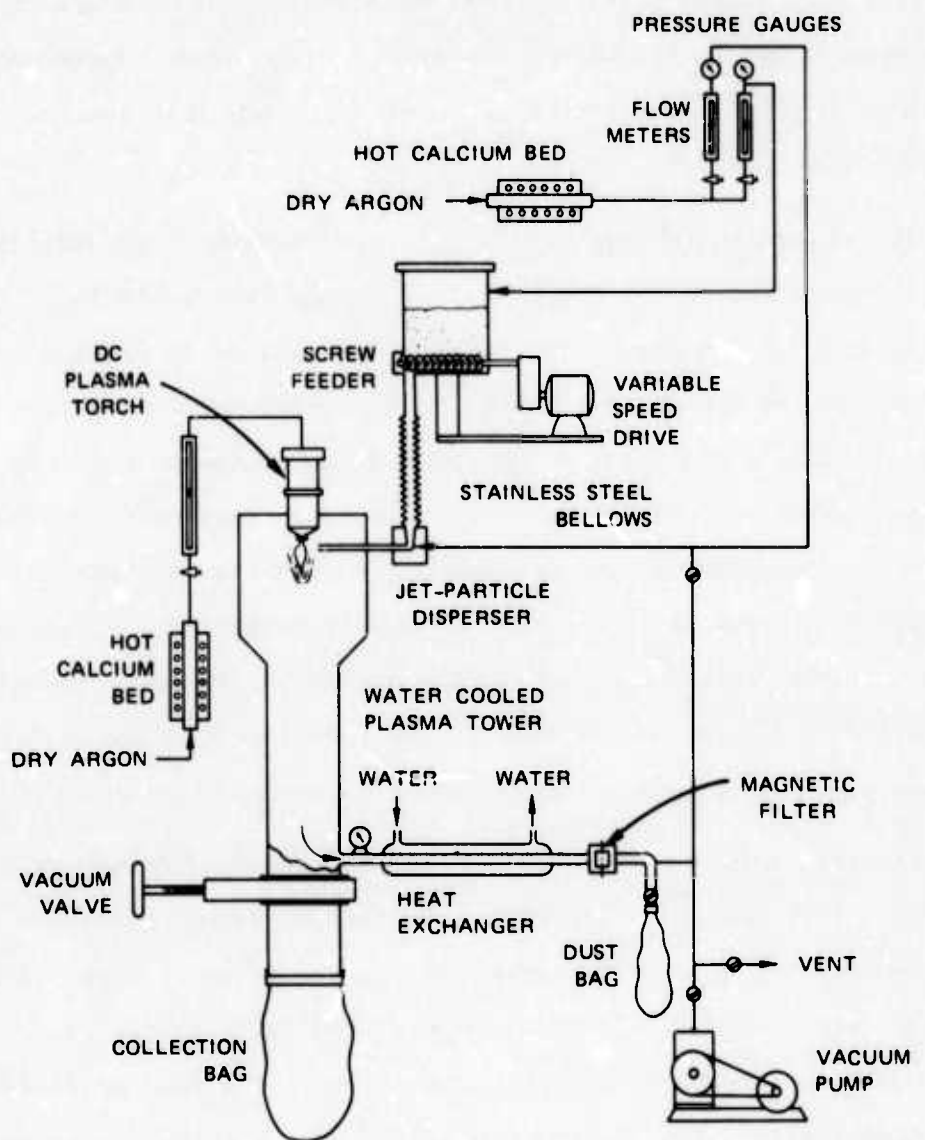


FIGURE 2 ARGON JET PARTICLE DISPERSER

The oxygen partial pressure in the gettered argon inlet stream was monitored with a high temperature zirconia electrochemical cell, and was usually observed to be 10^{-16} atm. or lower. The effluent argon from the plasma chamber generally contained 10^{-22} atm. oxygen partial pressure. Hence, almost all of the residual oxygen was absorbed by the particles during spheroidization, but the total amount of oxygen was negligible. Electron beam microprobe analyses indicated that when oxygen was picked up, it was confined primarily to the samarium fume formed by the evaporation and condensation of samarium from the primary liquid alloy droplet.

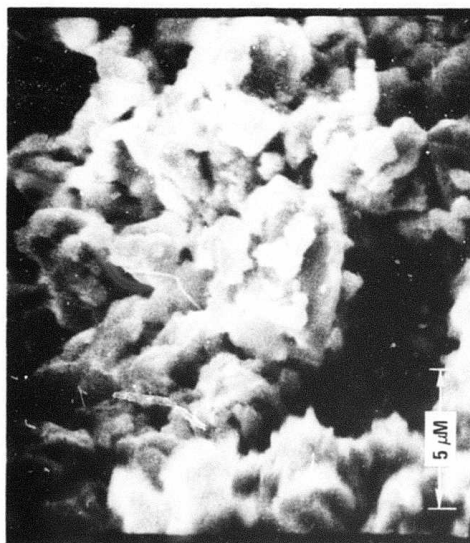
Most of the plasma-treated particles attached to the chamber walls after passing through the plasma, and therefore the plasma chamber was rigged as a vacuum glove box so that these particles could be dislodged into a container attached to the plasma chamber through a vacuum port. After each plasma run, the particles were removed and transported to another glove box without air contamination.

1. Plasma Spheroidization

Plasma melting and spheroidization have been investigated for cobalt alloys of samarium and praseodymium. A minor amount of work has been done on misch metal alloys. Alloys with the RECo_5 and RE_2Co_7 compositions have been used. All of the particles are spheroidized, and solid rather than hollow spheres are formed. The particle size distribution of the spheres is essentially the same as the particle size distribution of the feed, as evidenced by optical and scanning electron microscopy, see Figure 3. Sectioned and polished spheroidized particles are shown in Figure 4. After etching, grain boundaries within the particles are seen, as in Figure 5. The solidification of polycrystalline spherical particles, rather than single crystals, is a major drawback to the use of spheroidization as a method of producing magnetic powders, since complete crystallographic orientation within a magnetic field cannot be achieved. Consequently,



SPHEROIDIZED



COMMINUTED

TA-8731-9

FIGURE 3 SCANNING ELECTRON MICROGRAPHS BEFORE AND AFTER PLASMA
SPHEROIDIZATION OF SmCo_5

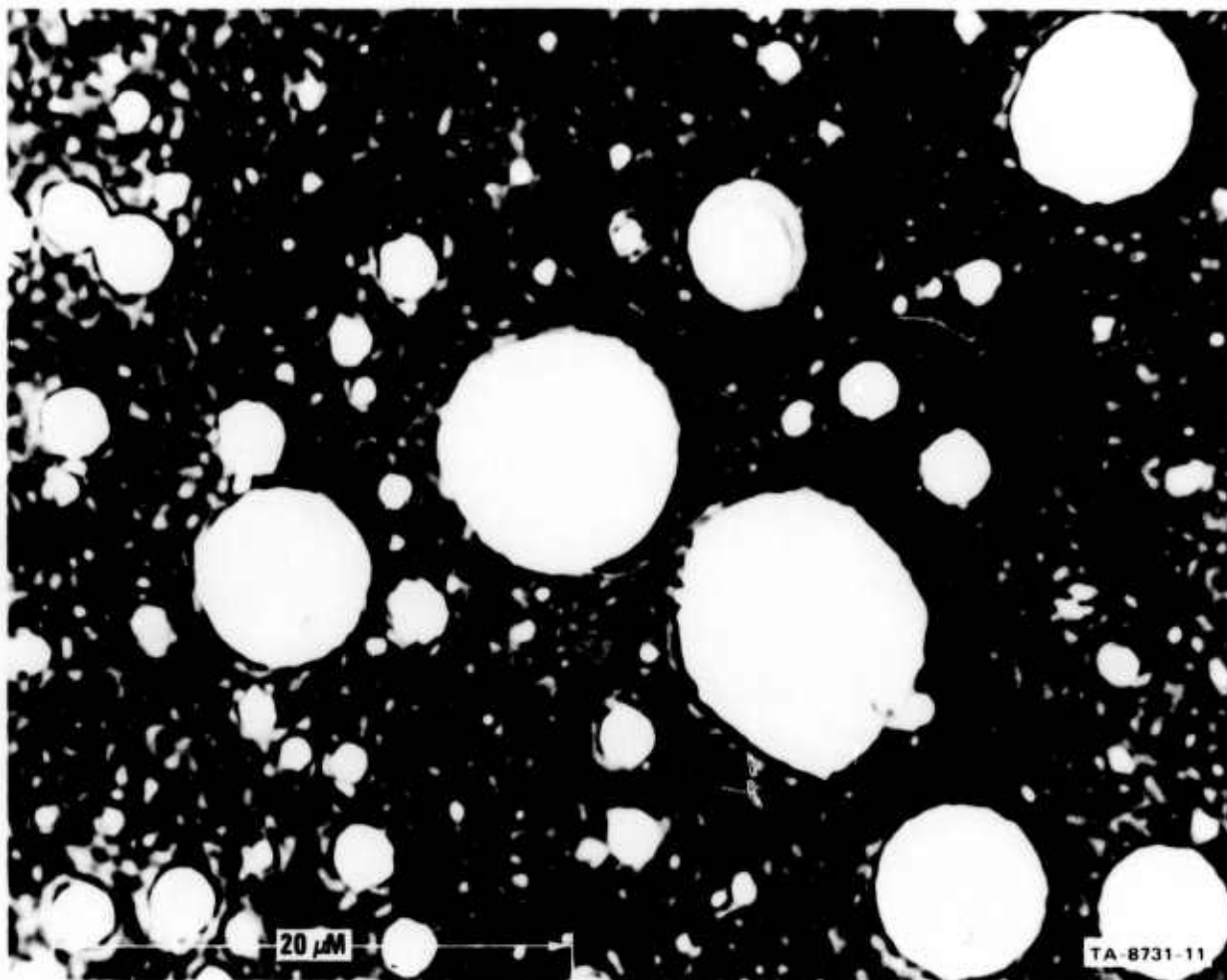


FIGURE 4 SPHEROIDIZED SmCo_5 IN SECTION (BRIGHT FIELD)

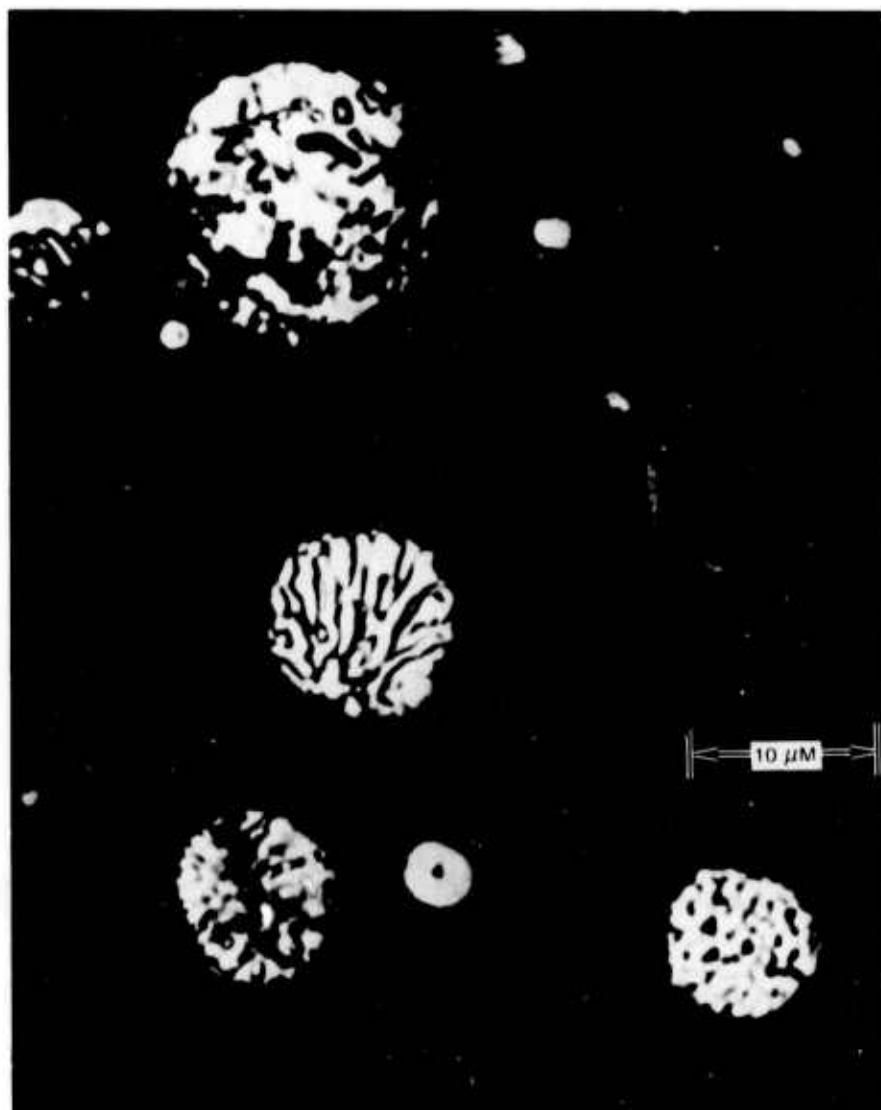


FIGURE 5 METALLOGRAPHIC CROSS SECTION OF SPHEROIDIZED
Sm-Co ALLOY PARTICLES (Primarily SmCo_5)

magnetic saturations are less than optimum.

The scanning electron micrographs of the spheroidized particle show a bimodal size distribution of (1) larger spherical particles, and (2) extremely fine (submicron) fume. Although fume is found separate from spherical particles, some fume also attaches to the particles, and the attachment appears to be strong enough to suggest magnetic agglomeration of fume and particles. A magnetic interaction would require that the fume contain cobalt as well as samarium or other volatile rare earths. This was confirmed by electron microprobe analyses of the SmCo_5 spheroidization products. Powders were mounted in a conducting mount, sectioned and polished for metallographic and microprobe analysis. The samarium content of the spherical particles varied considerably, from 10 to 35 wt% with an average Sm content below the stoichiometric amount for SmCo_5 . The balance of the material in the spherical particles was cobalt, and microprobe spectroanalysis showed that the impurity content of the spherical particles was identical with the impurity content of the starting materials--showing very minor amounts of silicon, aluminum, and cerium.

The fume did contain both samarium and cobalt, but the samarium-cobalt ratio was higher than that obtained with the spherical particles. Because of the low effective density of a mass of fume particles it is not possible to make a quantitative analysis of these particles based on relative intensities of samarium, cobalt, and other elements. However, the major constituents were cobalt, samarium, and oxygen. The oxygen was introduced when the system was opened to air, and some chemical reaction occurred with a noticeable release of heat. Impurities found in the starting materials and the spherical particles were also present in the fume.

The electron microprobe fluorescent analyses of spherical particles and fume found in the SmCo_5 are summarized in Table I. Average particle size analyses of spheroidized products measured by the Fisher method were

Table I
SEMIQUANTITATIVE ANALYSIS
OF INITIAL AND SPHEROIDIZED SmCo_5 - Run 7
(wt%)

	Co	Sm	Al	Si	Ce	La	O ₂	C
Initial	61.0 (1,2)	31.6 (1)	~ 0.2	~ 0.2	~ 0.3	< 0.1	Nil	-
Spherical particles	60-85 (Avg. = 68%)	12-35 (Avg. = 28%)	~ 0.3	~ 0.3	~ 0.3	< 0.1	Nil	-
Fume	22-31 (Avg. = 27%)	31-36 (Avg. = 33%)	~ 0.2	~ 0.4	~ 0.3	< 0.1	~ 12 (3,4) (uncorr.)	~ 5 (4) (uncorr.)

¹The cobalt and samarium feed analyses of individual particles varied $\pm 2\%$.

²Stoichiometric SmCo_5 contains 33.8% Sm and 66.2% Co.

³Oxidation occurred with considerable release of heat when air was admitted to the sample.

⁴Based on relative intensities without absorption or other matrix corrections.

in the range from 0.3 to 0.7 μm . The average size is lowered from the average size of the starting material only by the presence of the fume. These results are entirely consistent with melting, coupled with substantial vaporization of the rare earth followed by quenching of both the spherical particles and fume.

A major problem associated with the preferred vaporization of samarium or other rare earth components in the liquid alloy during spheroidization is a shift in the alloy composition caused by the loss of samarium. When evaporation is substantial, this leads to a two-phase microstructure consisting of RECo_5 and $\text{RE}_2\text{Co}_{17}$.

A large number of plasma spheroidization runs were made, using SmCo_5 and PrCo_5 particles smaller than 10 μm at various operating conditions, to achieve melting while minimizing excess feeding and rare earth vaporization losses. A minor amount of work was also done on mischmetal cobalt alloys. Analysis of the spheroidized particles show that it is not possible to melt all the SmCo_5 or PrCo_5 particles passing through the plasma without losing substantial amounts of samarium or praseodymium, and thereby causing precipitation of $\text{RE}_2\text{Co}_{17}$, as well as RECo_5 phases within the quenched spherical particles. Although praseodymium has a much lower vapor pressure than samarium, vaporization losses from liquid particles and other processing characteristics for praseodymium cobalt alloys are about the same as for the corresponding samarium alloys. This suggests that the slow process step controlling the rate of vaporization in these very small droplets, with a high surface area to volume ratio, may be diffusion of the rare earth element within the liquid droplet to the droplet surface, rather than the vaporization step itself.

No measurable loss of samarium or praseodymium occurs during plasma heating of a particle unless the particle melts. Since the equilibrium vapor pressure of solid and liquid at the melting point must be

identical if they have the same composition, this supports the diffusion-limited hypothesis for vaporization. Typical liquid metal diffusion coefficients are in the range from 10^{-4} to 10^{-6} cm^2/sec , whereas diffusion coefficients in solid alloys are usually several orders of magnitude smaller, even at temperatures just below their melting point.

Additional spheroidization runs were made, using ground Sm_2Co_7 and Pr_2Co_7 particles, so that the higher rare earth concentration in the starting material would compensate for vaporization losses in the plasma. The composition of particles is shifted, and one pass through the plasma yields an average composition midway between that of RE_2Co_7 and RECo_5 . A second pass through the plasma gives average compositions approximately those of RECo_5 , but these results include the fraction of the fume that is collected with the larger spherical particles.

Plasma spheroidized particles were characterized by wet chemical EDTA analysis, x-ray fluorescence analyses, metallography, and electron beam microprobe analysis. All of the analytical methods except EBM analysis gave determinations that are averaged over all the grains present in an aggregate. The composition variations of randomly selected spheroidized particles are demonstrated by results of EBM analysis of PrCo_5 particles in Figure 6. The variations of praseodymium analyses are much greater than the variations of the sums of praseodymium and cobalt analyses. For each particle, the cobalt variation was approximately equal and opposite to the praseodymium variation. Hence, the variations are real, not due to instrument error or caused by the electron beams overstepping a small spherical particle. In the latter instances, both praseodymium and cobalt concentrations would be varied. A similar variability in the composition of spheroidized particles was obtained for SmCo_5 alloys. The most plausible explanation for the variation in rare earth concentration in spherical particles is that particle residence times in the plasma are not uniform because there is considerable particle

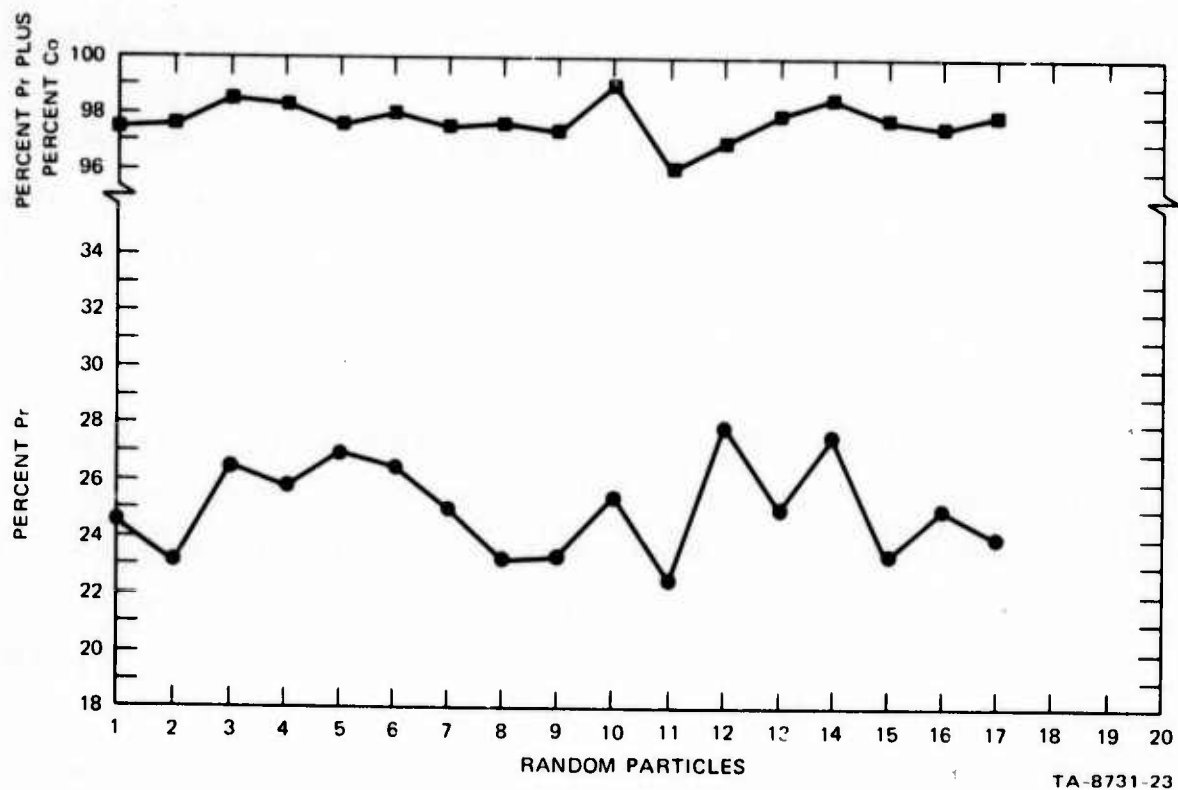


FIGURE 6 VARIATION IN PRASEODYMIUM CONTENT OF SPHEROIDIZED PARTICLES FROM MELT 22; 32.4% Pr

turbulence. A greater fraction of the rare earth was lost from small particles than from large ones. Longer plasma residence times are expected to increase the loss of the volatile rare earth element.

2. Plasma Annealed RECo₅ Particles

The argon plasma has also been used to heat SmCo₅ and PrCo₅ particles to high temperatures without exceeding their melting points. The plasma provides a relatively noncontaminating atmosphere where the hot particles are not in contact with each other and cannot sinter. Possible advantages anticipated for this heat treatment included relief of internal stresses in the comminuted particle, removal of surface oxides when the heat treating is conducted in an atmosphere containing a sufficiently reducing vapor such as samarium or calcium, and removal of surface layers by hot gas etching.

Two types of experiments were performed. In the first type of experiment, previously comminuted powders of SmCo₅ and an enriched samarium-cobalt eutectic alloy were well mixed and injected into the plasma torch at low power settings where only the eutectic particles melt. Since the eutectic particles contain a high proportion of samarium, considerable samarium vaporization occurs when they melt; and this tends to inhibit oxidation of the magnet alloy particles. Plasma annealing previously spheroidized particles was also investigated.

In the second type of experiment, chlorine was included with argon in the particle carrier gas and injected in a low-power plasma where particle melting does not occur. At elevated temperatures, chlorine will react with both samarium and cobalt to yield volatile chlorides. The chlorides of these metals were collected from the downstream gases and the surface texture of the particle changed, indicating that chlorine does etch the particle surface during its short exposure in the plasma.

3. Magnetic Properties of Plasma-Treated Particles

Magnetic properties of plasma spheroidized and plasma annealed SmCo_5 and PrCo_5 powders were determined with a vibrating magnetometer using a magnetizing field of 70 kG for most specimens. Some of the results are summarized in Table II.

Both plasma annealing and plasma spheroidization substantially lower the intrinsic coercivities of SmCo_5 . Spheroidization (melting) lowers the coercivity slightly more than does plasma annealing. The remanent magnetization of the spherical particles is reduced, because some are not single crystals; therefore perfect alignment cannot be achieved. Attempts to induce recrystallization in spheroidized particles by annealing at 800°C were not successful. A parametric study of the role of oxygen during plasma spheroidization and plasma annealing showed that oxygen had no statistical effect on the resulting intrinsic coercivities. Both plasma annealing and spheroidization also lowered the intrinsic coercivities measured with PrCo_5 .

Finally, plasma-spheroidized powders and plasma-annealed powders were fabricated into sintered magnets and magnetically evaluated. The powders were blended with a 60% samarium-40% cobalt sintering additive and aligned in a magnetic field of 24 kOe. The results are shown in Table III. The magnetizing field for all of the sintered specimens was 60 kOe. Although most of the intrinsic coercivities are low, the data show that high intrinsic coercivity can be obtained with spheroidized SmCo_5 . (Note sample SL-5 with an intrinsic coercivity of 25.7 kOe.) The higher coercivities in spheroidized materials were only obtained in the samarium cobalt system when the spheroidized particle was essentially single phase SmCo_5 , and even in these cases the high coercivities were only obtained after sintering with the samarium-rich sintering aid. The higher coercivities occur because of the diffusion of samarium into the spherical SmCo_5 particle until a hyperstoichiometric samarium-rich SmCo_5 compound is achieved. Nevertheless, the

Table II
MAGNETIC PROPERTIES OF PLASMA SPHEROIDIZED
AND PLASMA ANNEALED POWDER

Alloy (Nominal)	Ball Mill Grinding (hr)	Plasma Oxygen Pressure (atm)	Anneal/ Spheroidize	H _M (kOe)	H _C (kOe)	4πM ₃ (Gauss)	Remarks
SmCo ₅	3	--	Spheroidized	51	3.64	3101	Powder exposed to air two weeks at room temperature
SmCo ₅	3	--	Spheroidized	47	3.85	2540	
SmCo ₅	10	1 x 10 ⁻⁶	Spheroidized	58	7.14	6600	
SmCo ₅	10	2 x 10 ⁻¹⁶	Spheroidized	60	8.13	4020	
SmCo ₅	10	2 x 10 ⁻¹⁶	Spheroidized	58	3.6	3530	
SmCo ₅	3	2 x 10 ⁻¹⁶	Spheroidized				Reruns of previous spheroidized material
SmCo ₅	10	2 x 10 ⁻¹⁶	Annealed	58	8.7	8050	
SmCo ₅	10	--	Annealed	58	11.3	8280	
SmCo ₅	10	3 x 10 ⁻¹⁹	Annealed	61	11.4	6710	
PrCo ₅	10	3 x 10 ⁻¹⁹	Spheroidized	59	1.43	3900	
PrCo ₅	10	3 x 10 ⁻¹⁹	Annealed	58	1.71	5050	
PrCo ₅	10	--	Annealed	48	1.64	3490	

Table III

MAGNETIC PROPERTIES OF SINTERED MAGNETS
FABRICATED FROM PLASMA SPHEROIDIZED
AND PLASMA ANNEALED MATERIALS

Composition *	Particle Processing (Anneal/Spheroidize)	H _C (kOe)	4M _r [†] (Gauss)	Alignment Factor ^{††}
SmCo ₅	Spheroidized	3.14	3020	-
SmCo ₅	Spheroidized	2.5	3360	0.47
SmCo ₅	Spheroidized	9.1	2720	-
SmCo ₅	Spheroidized	15.0	3100	0.65
SmCo ₅	Spheroidized	3.64	2360	-
SmCo ₅	Spheroidized	25.7	4650	0.94
SmCo ₅	Annealed	3.1	5380	0.80
SmCo ₅	Annealed	4.14	5000	0.73
SmCo ₅	Annealed	7.28	3610	-
SmCo ₅	Annealed	5.6	4990	0.75
SmCo ₅	Annealed	7.4	4500	-
SmCo ₅	Annealed	8.15	4820	0.71
PrCo ₅	Spheroidized	-	0	-
PrCo ₅	Annealed	-	0	-
PrCo ₅	Annealed	17.1	4230	0.70
PrCo ₅	Annealed	19.7	7720	0.90

* All magnets were formed with 20% of sintering aid (60% Sm + 40% Co)

[†] The alignment factor was obtained by dividing 4M_r by 4M at 60 kOe.

^{††} No adjustment was made for the volume occupied by the sintering aid, and these values have not been corrected for demagnetization effects.

magnetic remanence of these materials was low because of polycrystalline spherical particles.

Annealing PrCo_5 in a plasma did not produce high coercive force powders immediately following plasma annealing. However, when these powders were sintered at 1130°C using a samarium cobalt sintering aid, the intrinsic coercive force of the resulting PrCo_5 magnet was 19,700 Oe.

In summary, neither plasma spheroidization or plasma annealing produced particles with coercivities superior to those produced by ball milling under properly controlled conditions. Since the magnetic remanence was generally lower, and the cost of processing greater, there is no incentive to produce samarium cobalt alloy powders by either of these methods.

C. Electrodeposition

Several of the RECo_5 compounds, including SmCo_5 , do not melt congruently. When these materials are produced by cooling the liquid of this composition, $\text{RE}_2\text{Co}_{17}$ is crystallized, and on further cooling, a peritectic reaction between the residual samarium-rich liquid and the $\text{RE}_2\text{Co}_{17}$ solid compound is required to produce RECo_5 . The rearrangement is necessary, and poor homogeneity of the lattice may result. Consequently, there was interest in exploring the magnetic properties of RECo_5 particles produced at temperatures below the peritectic temperature. In principle, this can be accomplished by growing crystals of the RECo_5 compound from a suitable solvent containing both the rare earth and cobalt. In this particular program, electrodeposition from fused fluorides and organic electrolytes was studied.

Fused salt electrolytic experiments were conducted, using a barium fluoride/lithium fluoride eutectic electrolyte. A molybdenum anode and a SmCo_5 cathode was used. Depending on the experimental conditions, lithium, samarium, and a samarium-cobalt alloy were deposited.

However, it was not possible to deposit a stoichiometric SmCo_5 compound; furthermore, the deposit was massive rather than particulate. Hence, there was no real incentive to utilize this method in producing magnetic particles.

Several electrolytic experiments were conducted at room temperature with organic electrolytes, using a variety of electrodes and electrolyte materials. Propylene carbonate, acetone, methanol, and acetonitrile were used as electrolytes. Electrodeposited particulates were produced, but the compositions were not stoichiometric SmCo_5 ; therefore these organic electrolysis methods were unsuccessful.

D. Metallothermic Reduction of Alloy Sponge

Direct metallothermic reduction involves the use of a metal more reactive than samarium to reduce both samarium and cobalt salts simultaneously and form an alloy product in the form of a metallurgical sponge, or loose agglomeration of particles. This is a potentially less expensive method for producing RECo_5 alloy powders than the conventional sequence of separate rare earth-metal reduction and purification, vacuum arc melting of the alloy, and crushing. Metal sponges produced by metallothermic reduction are generally much coarser than the particle size required for magnet sintering; and therefore further grinding of the metal sponge is required.

A thermochemical study was made of potential processes for metallothermic reduction of oxides and halides of cobalt and samarium to form SmCo_5 . The other rare earths will have similar thermodynamic behavior. Particular attention was paid to systems in which the metallothermic reaction product is a two-phase mixture of SmCo_5 particles and a salt or slag phase that can be subsequently leached or otherwise chemically processed, to extract the salt or slag without adversely affecting the SmCo_5 particles.

Free energy data for the formation of oxides indicate that only calcium and thorium are possible reductants for the rare earth oxides, and thorium is undesirable because it is slightly radioactive. Calcium, barium, and lithium are suitable reductants for the rare earth fluorides. Rare earth chlorides cannot be reduced by any metal, with the exception of lithium and barium, but the free energy margin of these metals as reductants is very small. The bromides and iodides do not appear to provide any system for metallothermic reduction of corresponding rare earth salts.

Metallothermic reduction requires an intimate stoichiometric mixture of fine powders of (1) a rare earth salt, (2) cobalt metal or a cobalt salt, and (3) the reducing metal. The salts are brittle solids that can be readily ground. Cobalt can be obtained in powder form. Malleable metal reductants can be converted to brittle hydrides and then ground to yield fine powders. The alkali and alkaline earth hydrides generally decompose on heating, before or simultaneously with the reduction reaction.

A thermite reduction reaction between samarium and CoCl_2 was conducted in vacuum and in argon using an intimate mixture of powders. Since samarium powder is difficult to grind and very reactive, a samarium-cobalt eutectic alloy that grinds easily and is less reactive was substituted. The alloy and CoCl_2 were mixed in proper turns to yield a high samarium alloy and SmCl_2 . Upon heating, this reaction occurs exothermically. The resulting alloy melted and formed spherical particles of various sizes in a salt matrix; however, many of the particles were too large for magnet powder processing. Considerable splattering also occurred. The sample was leached in a sodium acetate solution to remove the soluble salts before chemical analysis. The alloy particles contained insufficient samarium: 78% cobalt and 16% samarium. The expected alloy composition based on chemical analysis of the alloy was 75% cobalt and 25% samarium.

Some of the samarium may have been lost by vaporization.

Direct reduction of CoCl_2 was also conducted in the presence of moderate amounts of the BaF_2/LiF eutectic as an activator to dissolve samarium and also as a heat sink to prevent a temperature excursion from the exothermic reaction and melting. The BaF_2/LiF eutectic salt was 43 wt% of the particle mixture. This mixture was heated in a tantalum crucible at 800°C for two hours without inducing a temperature excursion, and then cooled. The resulting alloy particles were extremely fine and could not be physically separated from the residual salt without oxidizing the alloy particles. Consequently, a true chemical analysis of the alloy cannot be obtained. The analysis of the total residue was consistent with a materials balance on the alloy and salt phases.

An SmCo_5 sponge was produced by calcium reduction of the stoichiometric mixture of hydrided calcium, samarium Sm_2O_3 , and cobalt powder. The metal-thermic reduction reaction was conducted in an iron retort heated in argon at various temperatures, depending on the composition, for 2 hours. After reaction, dilute hydrochloric acid leaching of the residue removed CaO and left a SmCo_5 sponge with a particle size of about 35 mesh.

The x-ray diffraction pattern of the SmCo_5 sponge exhibited little line broadening and indicated that the alloy was more homogeneous and less strained than alloys produced by arc melting and quenching. With the exception of a trace of Sm_2Co_7 there was no other phase detected. Sieving the SmCo_5 sponge before any grinding yielded a trace of $\sim 20\ \mu\text{m}$ particles, but these were not magnetic and were probably unleached CaO . Neutron activation analysis shows the oxygen content to be 1700 ppm after ball milling. Part of this oxygen probably results from residual CaO , but the oxygen concentration is similar to arc-melted and ball-milled SmCo_5 .

SmCo_5 sponge and arc-melted SmCo_5 have similar magnetic properties after ball milling. Measured intrinsic coercivities were in excess of

20,000 Oe. However, the magnetic remanence of sintered magnets made from SmCo_5 sponge was reduced because of inadequate liberation of small crystals during ball milling (2 hours), which prevented ideal magnetic alignment. Polycrystalline SmCo_5 grains are shown among the ground thermite alloy particles in Figure 7. Other rare earth-cobalt alloys and mixed rare earth-cobalt alloys involving two rare earths were produced by the calcium metallothermic reduction method.

Metallothermic reduction has no advantages over alloy melting and ball milling insofar as the magnetic properties are concerned, but it may have an economic advantage in manufacturing sintered magnets in large quantities.

REFERENCES

1. K. Strnat et al., J. Appl. Phys., **38**, 1001 (1967)
2. J. J. Becker, IEEE Trans. Magnetics, MAG-4, 239 (1968).

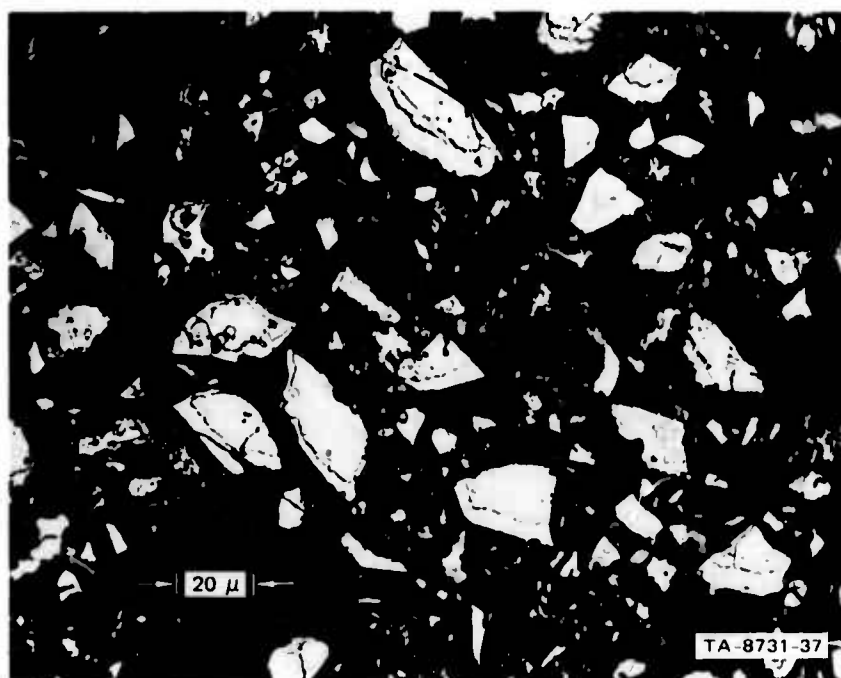


FIGURE 7 BALL MILLED SmCo_5 ALLOY PARTICLES REDUCED BY CALCIUM

II OXIDATION OF RECo_5

Introduction

Rare earth cobalt alloys, and SmCo_5 in particular, can exhibit high magnetic coercivities and have been the basis of a new class of sintered permanent magnets. The processing of these magnets usually entails particle comminution, magnetic orientation of the powder, compaction, sintering, and remagnetization of the thermally demagnetized sintered magnets. The present study was conducted because there was evidence suggesting that surface oxidation is detrimental to magnetic coercivity. For example, moderately high coercivities in particles can be obtained only by grinding in the absence of oxygen. Furthermore, storage of the ground particles in air at room temperature causes a reduction in magnetic coercivity.¹ Heating high coercivity particles in presence of oxygen lowers the coercivity² whereas etching particles, which removes the surface oxidation products, raises the coercivity.³

Experimental Program

The experimental program used vacuum arc-melted polycrystalline button ingots, usually with a polished flat surface, and SmCo_5 powders produced by ball milling in sodium gettered hexane. All starting materials were single-phase SmCo_5 and were subjected to x-ray diffraction and chemical analysis.

Sectioning an ingot normal to the flat surface after oxidation provided a cross section for examination. Chemical compositions along the cross section were determined by electron beam microprobe analysis, with simultaneous determination of cobalt, samarium, and oxygen. Phase

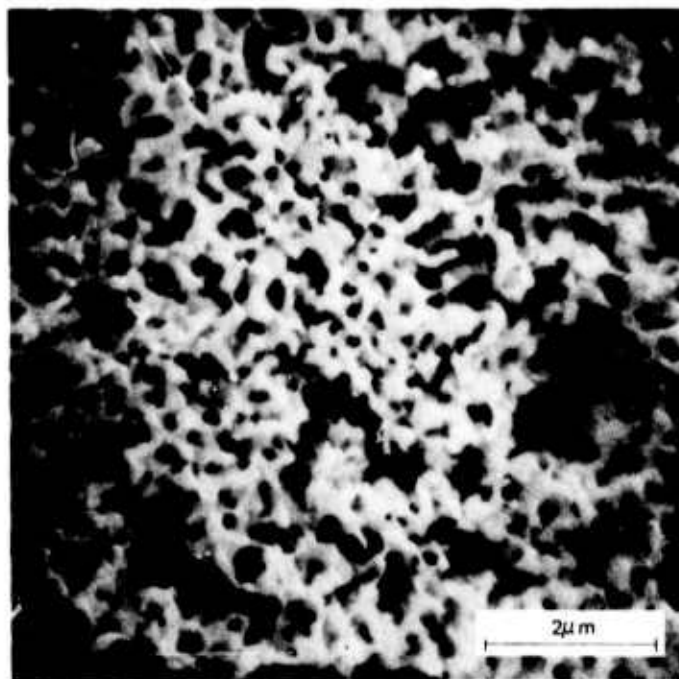
composition of the oxide subscale was determined by analyzing oxidized powders using x-ray diffraction powder methods. Although the subscale in cross section can be seen with light microscopy, resolution of the subscale composite microstructure required scanning electron microscopy.

Oxidation at temperatures from 350 to 1250°C produces a reasonably thick oxide subscale. Several ingot specimens were oxidized for various times at the same temperature, and the subscale thickness was determined metallographically by the sectioning method. Oxidation kinetics at lower temperatures were determined both thermogravimetrically, using an electronic microbalance, and by measuring the oxygen sorption as a function of time in a high vacuum apparatus employing a zirconia electrochemical cell as the oxygen measuring device. Both the thermogravimetric and oxygen consumption experiments were conducted on SmCo_5 particles having an average particle size of 25 micrometers.

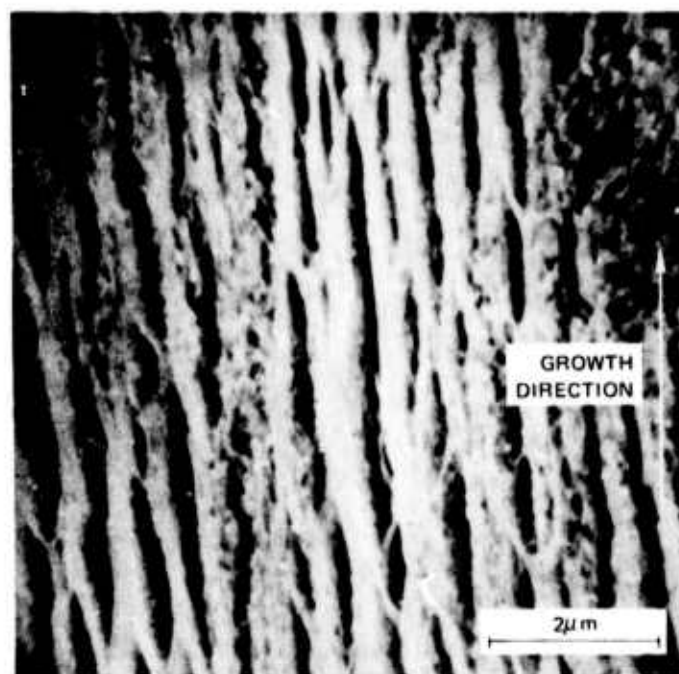
Oxidation Products: Subscale Microstructure and Composition

SmCo_5 oxidizes to produce two conjugate layers, a thin outer oxide scale and a thicker subscale, that can be readily seen under bright field illumination without etching the specimen. Formation of the outer oxide scale, which is composed of cobalt oxide and samarium oxide, can be prevented by oxidizing in oxygen partial pressures lower than the oxygen dissociation pressure for CoO . The subscale is a metal/oxide composite consisting of parallel samarium oxide platelets and fibers surrounded by cobalt. The subscale is produced by internal oxidation of samarium, but the internal oxidation mechanism is unusual.

Scanning electron micrographs taken both parallel to and transverse to the direction of growth of the subscale structure are shown in Figure 8. These specimens were oxidized at 1125°C for two minutes in a 90% CO_2 /10% CO gas mixture, which prevents any oxidation of cobalt. After metallographic mounting, the specimens were etched in 50% HNO_3 + 30% H_2SO_4 + 20% H_2O and



(a) TRANSVERSE



(b) LONGITUDINAL

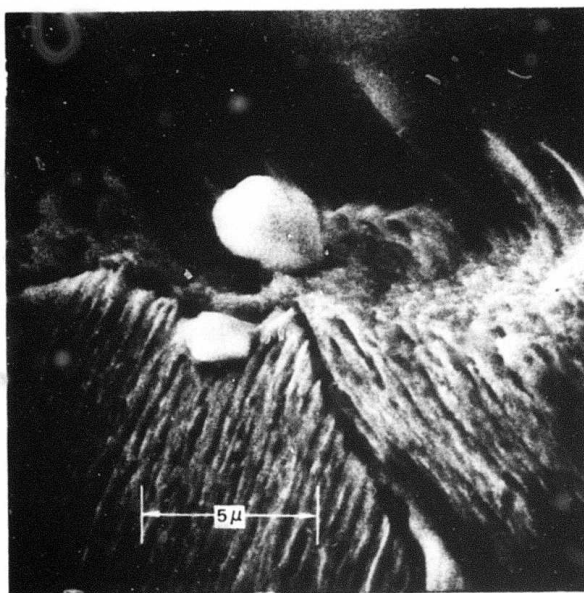
TA-8731-87R

FIGURE 8 FIBROUS STRUCTURE OF SAMARIUM OXIDE IN THE OXIDE/COBALT COMPOSITE SUBSCALE GROWN AT 1125°C

vapor coated with a gold-platinum alloy. The etching removes cobalt and leaves the oxide structure in relief. The transverse section indicates that the oxide consists of continuous fibers, narrow platelets, and a loosely interconnected network of platelets. The subscale microstructure is very similar in appearance to that of a eutectoid microstructure and dissimilar to the microstructure produced by classical internal oxidation, which consists of oxide particles dispersed in a metal matrix.

Although the orientation of the oxide platelets generally follows the direction of oxygen transport to the subscale-alloy interface, the platelets cluster into parallel groups that give the appearance of a "grain" structure at lower magnification. This effect is illustrated by the scanning electron micrograph shown in Figure 9. The subscale appears in the lower part of the micrograph with a bisecting "grain" boundary and unoxidized SmCo_5 appears in the upper part. These so-called "grains" are not easily distinguished in a light microscope unless polarized light is used. When platelet microstructures result from eutectoid decomposition, the grain of commonly oriented platelets often corresponds to preexisting grains in the single phase structure before decomposition. However, in this case the subscale "grain" size is smaller than the original cast SmCo_5 grain size.

X-ray diffraction determinations of the phase composition of the subscale have been made on both oxidized powder samples and oxidized flat surfaces of cast pieces, over a temperature range from 320 to 1000°C. Oxygen, air, and 90% CO_2 /10% CO oxidizing atmospheres were used. In all cases the metal produced in the subscale is β -cobalt (cubic). The normal polymorph of cobalt over most of this temperature range is α -cobalt (hexagonal). The rare earth metals are reported to be insoluble in cobalt and do not affect the α - β transformation.⁴ Cubic cobalt may result because of an orientation relationship with the samarium oxide phases.



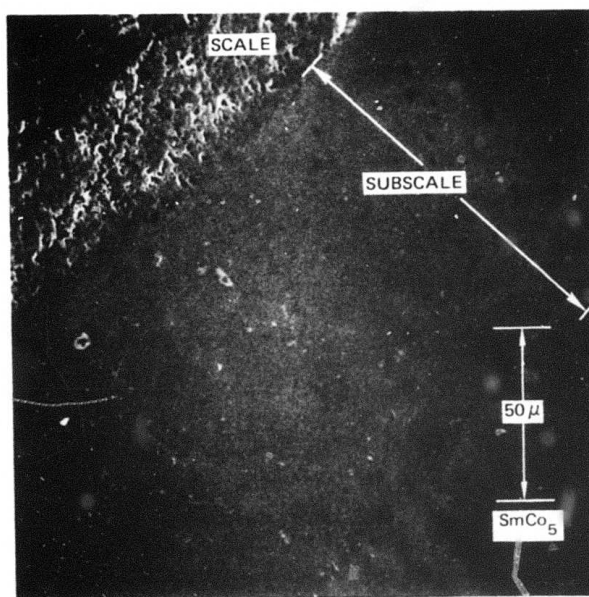
TA-8731-69

FIGURE 9 SUBSCALE/SmCo₅ INTERFACE AND INTERSECTING "GRAINS" WITHIN THE SUBSCALE STRUCTURE

The monoclinic sesquioxide, B-type Sm_2O_3 , is produced at all oxidation temperatures. Pure Sm_2O_3 exhibits the monoclinic structure above 850 to 900°C, and a cubic structure, C-type Sm_2O_3 , is usually observed at lower temperatures.⁵ X-ray diffraction peak intensities for the C-type sesquioxide are very weak or nonexistent in the subscale on SmCo_5 . No other samarium oxide phases are observed unless nitrogen is also present.

After oxidation in air, a suboxynitride phase, $\text{SmN}_{1-x}\text{O}_x$ (NaCl structure) is observed and the Sm_2O_3 peaks are weak. This samarium compound has been previously prepared and identified by Felmler and Eyring.⁶ Electron-beam microprobe analyses on air-oxidized samples have indicated that the actual oxygen content of the subscale is about 4.7 wt% (18.7 at.%), which is somewhat less than required stoichiometrically for oxidation to Sm_2O_3 and cobalt and somewhat greater than the amount required stoichiometrically for oxidation to SmO and cobalt. This finding is consistent with the presence of both the sesquioxide and suboxynitride in the subscale. However, nitrogen was not detected by EBM analysis. Based on EBM traverses, there were no measurable concentration gradients of oxygen, rare earth, or cobalt across the subscale in the direction of subscale growth during oxidation.

There was considerable porosity in the outer oxide scale, but no porosity was observed in the subscale. This is illustrated by the scanning electron micrograph shown in Figure 10. Porosity in the scale is probably associated with vacancy accumulation during the oxidation of cobalt to form cobalt oxide, since cobalt oxide is known to contain cobalt vacancies and the mechanism of oxide scale growth on cobalt by thermal oxidation entails the outward diffusion of cobalt ions in the oxide and the counterdiffusion of cobalt ion vacancies.⁷ Although most of the vacancies are annihilated by the cobalt interface reaction, an appreciable fraction of vacancies usually accumulates as voids during oxide scale growth by oxidation of cobalt metal.



TA-8731-70R

FIGURE 10 POROSITY IN THE OXIDE SCALE RESULTING FROM OXIDATION OF SmCo_5 (SEM)

The samarium/cobalt concentration ratio is approximately the same in the subscale as in the unoxidized alloy. This result is expected in the absence of appreciable counterdiffusion of the reactive metal solute for classical internal oxidation. If counterdiffusion of the reactive metal solute were significant compared with the inward diffusion of oxygen, the subscale should be richer in the reactive metal (present in the oxidized form) than in the alloy before oxidation.⁸

Oxygen also penetrates cracks in polycrystalline SmCo_5 . The result is a subscale on either side of the crack. The penetration of internal oxidation starting within a crack is usually as extensive as the internally oxidized zone adjacent to open surfaces.

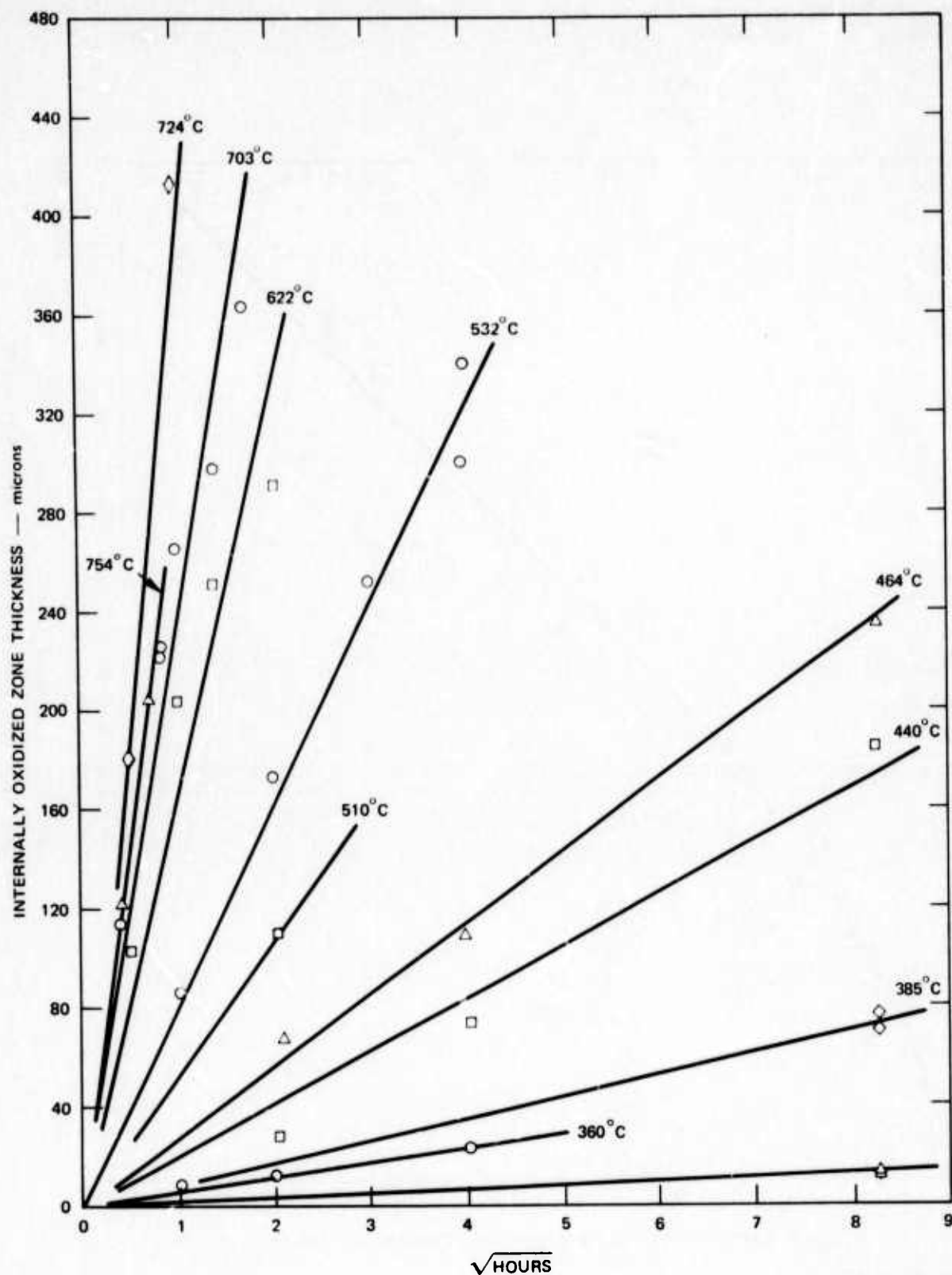
Kinetics of Internal Oxidation

A kinetic study of the oxidation process has shown that growth of the internally oxidized zone follows a parabolic rate law, as expected for both classical internal oxidation to produce a discontinuous distribution of oxide particles and for continuous oxide scale growth. The results of runs at several temperatures are shown in Figure 11. The thickness of the internally oxidized zone, δ , is given by

$$\delta = k_p t^{\frac{1}{2}}, \quad (1)$$

and the slopes of isotherms are the parabolic rate constants, k_p . Each data point represents a single isothermal oxidation/diffusion experiment on a polished ingot.

The temperature dependence of the internal oxidation rate follows the Arrhenius law to about 750°C with an apparent activation energy of 14.0 kcal/mol (58.8 k-J/mol), see Figure 12. However, there is a decrease in the apparent activation energy for the oxidation rate at higher temperatures. This is accompanied by a coarsening of the subscale composite microstructure. With two exceptions all the data points shown in Figure 12



TA-8731-43

FIGURE 11 PARABOLIC KINETICS OF THE SELECTIVE INTERNAL OXIDATION OF SmCo_5 IN AIR

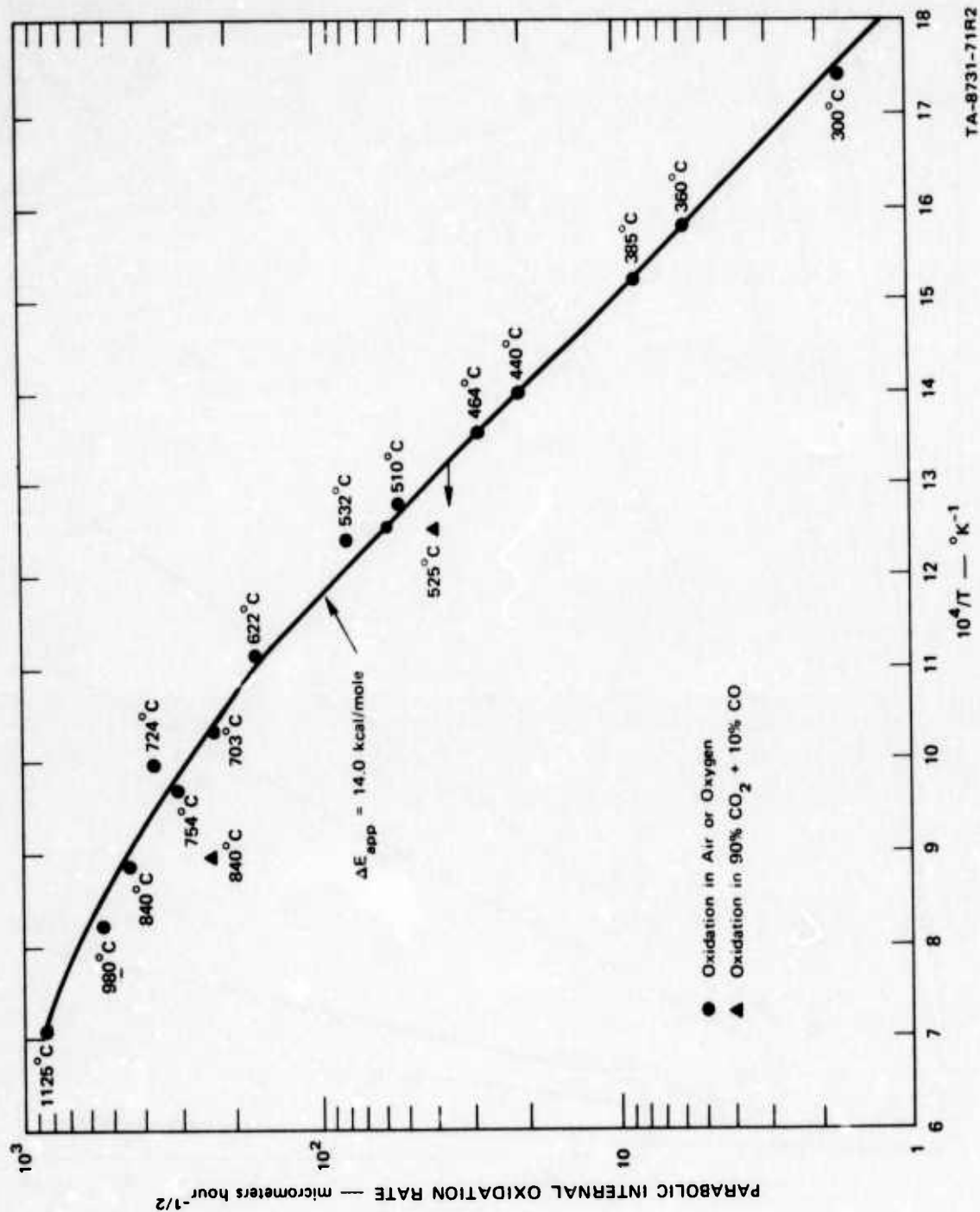


FIGURE 12 ARRHENIUS PLOT FOR THE INTERNAL OXIDATION RATE

were obtained from runs conducted in one atmosphere of air or oxygen. The remaining two data points were obtained from runs conducted in a flowing 90% CO₂/10% CO gas mixture.

The markedly reduced oxygen potential in the 90% CO₂/10% CO mixture caused a small decrease in the subscale oxidation kinetics at 840 and 525 °C to about half the respective rates obtained at the same temperatures in air. In general, for parabolic oxidation of metals the oxygen-pressure rate dependency is related to the point-defect concentration and defect transport mechanism in the oxide. The observed oxygen pressure dependence is much less than that encountered for any of the usual defect mechanisms responsible for ion diffusion in sesquioxides.⁵

Since SmCo₅ powders appear to be oxidized either at room temperature or at the slightly elevated temperatures resultant from the exothermic oxidation reaction, it is particularly important that kinetic data be obtained at very low temperatures so that the extent of oxidation as a function of particle size, time, and temperature can be predicted. The reaction was followed using gravimetric and oxygen consumption methods. The results were obtained using a single batch of 25 μm SmCo₅ particles. The particle size was determined by measuring the size of the particles using an optical microscope and then averaging the diameter. The extent of oxidation was limited to an oxide subscale thickness very much smaller than the particle radius. Consequently, the use of one-dimensional planar geometry was an adequate approximation in calculating the diffusion-controlled oxidation rate of the particles.

The weight gain and oxygen consumption curves obtained from these experiments were also parabolic, [Eq. (1)]. The results were converted into equivalent oxide scale thickness rates for comparison with the oxide scale thickness rates determined by the metallographic sectioning method used at higher temperatures.

The parabolic oxidation rates for the low temperature experiments are shown in Figure 13, where the straight line is an extrapolation of the Arrhenius plot from the high temperature data of Figure 12. These data show that the same oxidation mechanism observed at higher temperatures continues down to the lowest temperature at which rates could be measured, 100°C. The kinetics for the oxidation process between 100 and 1125°C shown in both Figures 12 and 13 span a range of oxidation rates that is seven orders of magnitude.

Although PrCo_5 has been less extensively studied, the oxidation mechanism and oxidation kinetics of this material are identical with those of SmCo_5 .

Discussion of the Oxidation Mechanism

The internal oxidation kinetics are consistent with internal oxidation as a moving boundary entailing diffusion of oxygen from the oxide scale through the subscale to the subscale/alloy interface. In problems of this type, parabolic kinetics result if the gradient of the diffusing species is small compared with the total concentration accumulated in the oxide phase within the subscale region. When this approximation is valid, diffusion through the subscale zone will be a nearly steady-state process.⁹ The parabolic rate constant is related to the diffusion coefficient D_O and the solubility difference ΔC_O of the major diffusant diffusing through the subscale according to the following equation:

$$k_p = \left(\frac{2D_O \Delta C_O}{W_O} \right)^{\frac{1}{2}}, \quad (2)$$

where W_O is the total amount of diffusant per unit volume of the subscale after complete oxidation of the samarium. This quantity can be calculated from the assumed stoichiometry of the oxide or from chemical analysis of oxygen and samarium in the subscale. The experimentally determined parabolic

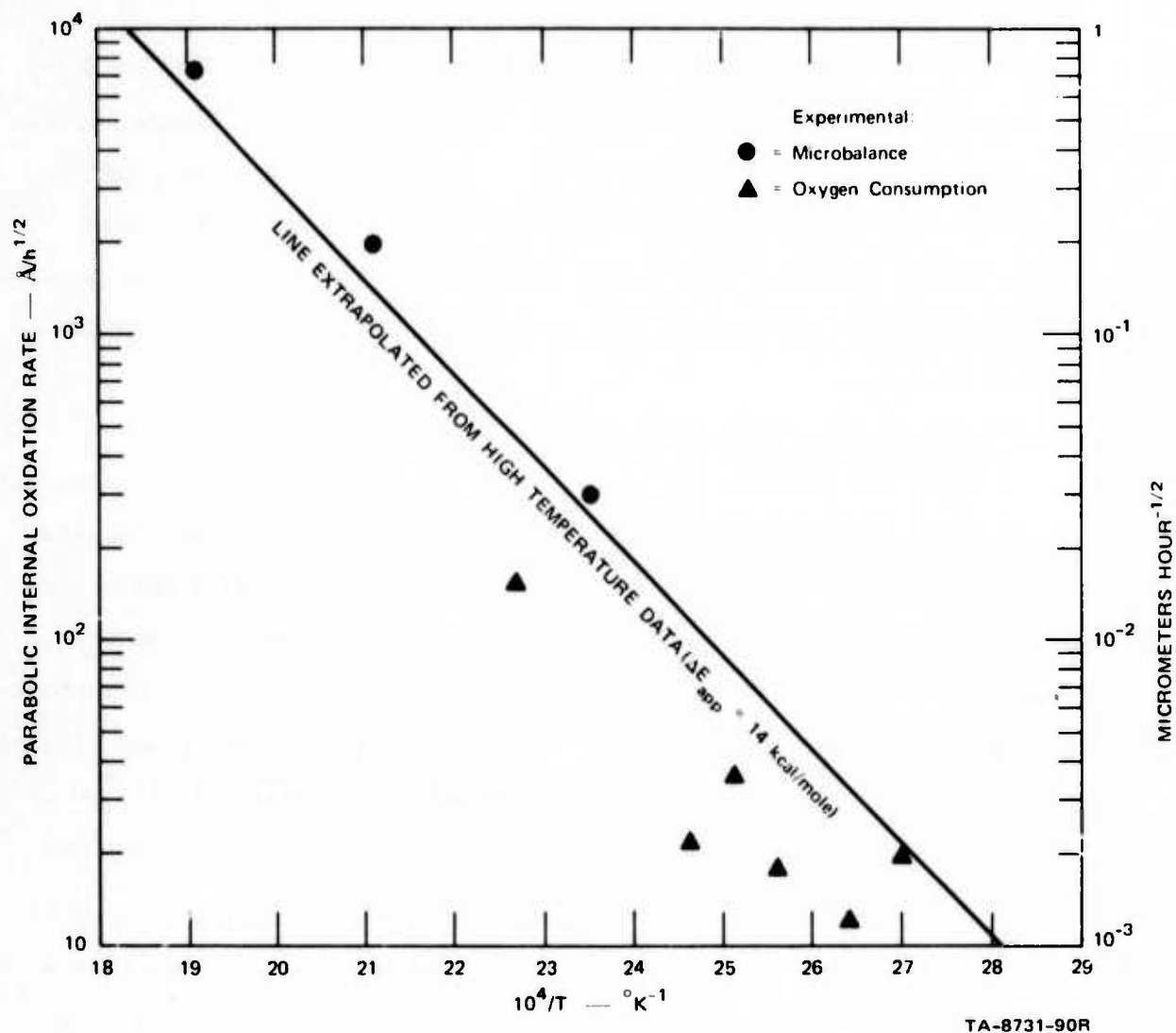


FIGURE 13 ARRHENIUS PLOT FOR THE INTERNAL OXIDATION RATE EXTENDED TO LOWER TEMPERATURES

rate constants, k_p , were used to determine the product $D_O \Delta C_O$ for any postulated mass transport mechanism. Below 750°C the value is

$$D_O \Delta C_O = 0.1 e^{-28000/RT} \text{ (g cm}^{-1} \text{ s}^{-1}) \quad (3)$$

Classical internal oxidation entails a small amount of the reactive solute metal dissolved in the less reactive metal matrix. Typically, the reactive solute metal is present in amounts of 1 or 2% and the subscale consists of a dispersion of isolated small particles within the less reactive metal matrix. When larger amounts of reactive solute are present, oxidation causes a reactive-metal external oxide scale rather than internal oxidation.

Because the solubilities of rare earth metals in cobalt are extremely low, counterdiffusion of samarium does not occur to a measurable degree, thus allowing internal oxidation to occur. However, the rare earth content of SmCo_5 is very high, 33 wt%. Consequently, internal oxidation produces a subscale with very large volume fractions of oxide. Consideration of the densities of cobalt and Sm_2O_3 indicates that the oxide content of the subscale is 38.8 vol%. The oxide phase is continuous because of the large volume of oxide in the subscale and its structural morphology.

With a continuous oxide phase present in the subscale, diffusion of oxygen can occur by three transport paths: the metal phase, the oxide phase, and the oxide/metal interface. Counterdiffusion of samarium within the oxide could also produce the subscale microstructure, but samarium diffusion through the metal phase of the subscale or along the oxide/metal interface would produce an oxide scale rather than the oxide/metal composite. In all previous examples of classical internal oxidation, the transport mechanism required diffusion of dissolved oxygen through the metal phase.

Consider the possibility of oxygen transport in the metal phase. Some limited data on the solubility of oxygen in β -cobalt have been published previously by Seybolt and Mathewson.¹⁰ If their solubilities for oxygen in β -cobalt are accepted and the concentration of oxygen within β -cobalt in equilibrium with samarium is taken as negligible, then a determination of the diffusivity can be made by comparing the solubilities with the calculated values of $D_O \Delta C_O$ derived from the experimental results. The required diffusivities of oxygen in β -cobalt to accommodate the observed internal oxidation rate would have to be $D_O \approx 1 \times 10^{-6} \text{ cm}^2/\text{sec}$ at 420°C and even greater at higher temperatures. In fact, at high temperatures the diffusion coefficient must be greater than those typically encountered for liquid metals. Consequently, transport of oxygen in the β -cobalt matrix cannot reasonably explain the rapid rate of growth of the subscale.

Based on the available information on diffusion of oxygen in B-type and C-type rare earth sesquioxides, it must be concluded that oxygen anion transport within the oxide fibers is also too slow to account for the rapid growth of the subscale. A study of self-diffusion of oxygen in B-type Sm_2O_3 has been made by Stone¹¹ over a temperature range between 696°C and 907°C using an isotopic exchange experimental technique. The activation energy for diffusion was about 23 kcal/mole.

Wirkus, Berard, and Wilder^{12,13} have reoxidized partially reduced rare earth sesquioxides and, although they have not studied Sm_2O_3 , they have obtained diffusion coefficients of the same order of magnitude in the same temperature ranges as the diffusion coefficients determined by Stone. Their implicit assumption is that these oxides are semiconductors, whereas Tare and Schmalzried¹⁴ find them to be ionic conductors at low oxygen pressures (C-type structure).

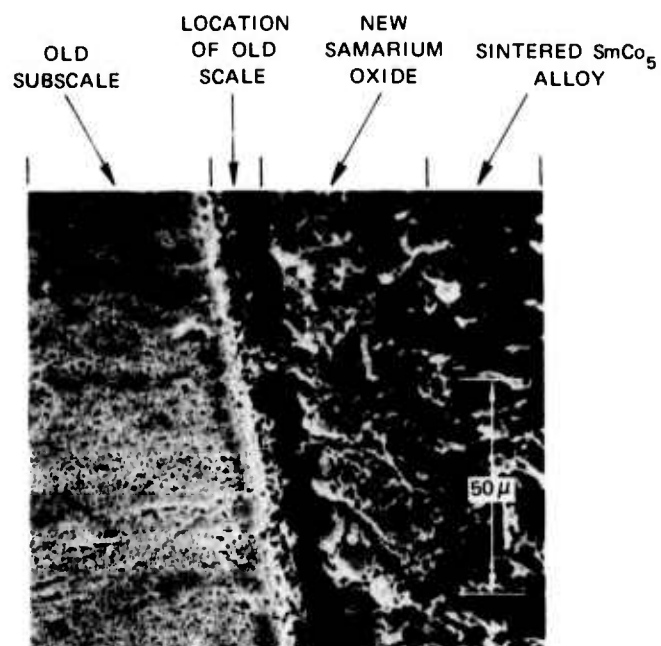
At 800°C the diffusion coefficient of oxygen in Eu_2O_3 determined by

Wirkus and Wilder is $D_O = 2.27 \times 10^{-10} \text{ cm}^2 \text{ sec}^{-1}$. The value obtained from Stone's data for oxygen diffusion in Sm_2O_3 at 800°C is $D_O = 2.76 \times 10^{-10} \text{ cm}^2 \text{ sec}^{-1}$.

If the rate of internal oxidation of SmCo_5 is determined by the flux of oxygen anions through Sm_2O_3 platelets, then the experimental value of $D_O \Delta C_O$ can be calculated from Eq. (3) and the results can be compared with the samarium oxide diffusion data obtained at the same temperature. The experimental value of $D_O \Delta C_O$ at 800°C is $2.0 \times 10^{-7} \text{ g cm}^{-1} \text{ s}^{-1}$. Matching the value for the diffusion coefficient determined by Stone, namely $D_O = 2.76 \times 10^{-10} \text{ cm}^2 \text{ s}^{-1}$, would require an oxygen concentration difference of about 700 g cm^{-3} . This conclusion is clearly absurd since the total oxygen concentration in Sm_2O_3 is only 1.17 g cm^{-3} and the actual driving force could only represent a concentration difference that is matched by an appropriate point-defect concentration difference in the oxide that would undoubtedly be much smaller than the total oxygen concentration in the oxide.

These calculations show that, if oxygen transport through the oxide is rate limiting, then the diffusivity must be much larger than the diffusivity observed by Stone¹¹ and by other investigators working on the diffusion of oxygen or reoxidation of partially reduced B- and C-type rare earth sesquioxides.

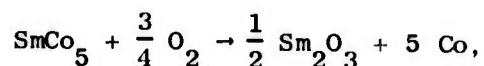
In a special experiment a previously oxidized ingot, including the oxide scale and oxide subscale, was surrounded by a SmCo_5 powder compact and was vacuum sintered. Both oxygen and cobalt were transferred out of the region occupied by the original cobalt oxide/samarium oxide scale and into the external sintered SmCo_5 , leaving a gap. Oxygen was transferred from CoO to samarium in the surrounding alloy. The gap can be explained if oxygen is the species diffusing in the new subscale and moving from left to right in Figure 14. The new subscale will be initiated at the old



TA-8731-77R

FIGURE 14 OXYGEN DEPLETED GAP BETWEEN THE ORIGINAL SUBSCALE GROWN ON SmCo₅ AND THE SAMARIUM-RICH ALLOY

scale/ SmCo_5 interface and grow outward. Since there is a negligible volume change for the total solids in the oxidation reaction,



a compensating bulk counterflow of the solid in reference to a stationary coordinate is not required and the gap will result.

Diffusion of samarium through the new samarium oxide would require accumulation of the new oxide in the region previously occupied by the CoO scale so that a gap would not form. If samarium were diffusing, the equivalent void space would have to occur in the samarium source region, which is also inconsistent with the experimental results. Migration of samarium outward by a vacancy exchange mechanism in the oxide phase would require the accumulation of internal vacancies and the precipitation of voids that, as shown in Figure 10, are not observed in the subscale. Hence, it must be concluded that oxygen is the diffusing species.

The oxidation process stabilized the fibrous microstructure of the subscale. When oxygen is evacuated from a furnace containing previously oxidized SmCo_5 the samarium oxide in the subscale undergoes recrystallization, disintegration of the fibrous microstructure and grain coarsening. The driving force for these microstructural changes is the reduction of interfacial energy associated with a reduction in interfacial area. Re-exposure of a specimen to oxygen at elevated temperatures after previous oxidation and vacuum recrystallization does not cause renewed internal oxidation because of the disruption of easy diffusion paths. Any oxidation that occurs is limited to cobalt at the subscale/oxygen interface.

There are no consistent phase changes in either cobalt or the samarium oxides that correlate with the apparent change in activation energy above 650°C . This supports the conclusion that bulk diffusion of oxygen is not fast enough in either cobalt or Sm_2O_3 to account for

the internal oxidation rate.

A set of O^{18} tracer experiments was performed in which 30 mesh $SmCo_5$ particles were sequentially oxidized in O^{16} followed by O^{18} . Other $SmCo_5$ particles were oxidized first in O^{18} followed by O^{16} . Then, each type of the oxidized particles was intimately mixed with spectrographic grade carbon and heated inside a Knudsen effusion cell to about $1250^\circ C$ in vacuum. Reduction of the outer region of the subscale by carbon produced a low partial pressure of carbon monoxide that effused from the cell and was monitored with a Nuclide 12-60-HT mass spectrometer. The intensity ratio $I_{CO^{28}}/I_{CO^{30}}$ was determined for each sample.

The results of this series of experiments show that the depth sequence of oxygen in the subscale is inverse to the oxidation sequence. Oxygen involved in early oxidation of $SmCo_5$ always occurs in the outer region of the subscale. Recently reacted oxygen occurs deeper in the subscale, nearer to the $SmCo_5$ alloy interface. Hence, reacting oxygen is transported directly to the inner interface by shortcircuiting the preexisting subscale-oxide. These results and the rapid rates of internal oxidation observed can be explained only by extremely rapid oxygen transport along the metal/oxide fiber interface. A large amount of interface area is available for oxygen transport because of the small dimensions of the composite microstructure.

The interface transport mechanism can also account for the apparent change in activation energy for the internal oxidation rate at high temperatures. The fiber size and spacing begin to increase with increasing temperature at about $750^\circ C$, and the interfacial area per unit volume of oxide subscale decreases correspondingly. If it is assumed that the same transport mechanism is involved at all the temperatures for which there are experimental data, then a reduction in the interfacial area would reduce both the number of effective paths for oxygen transport and the apparent activation energy, even though the true activation energy for

interface diffusion and the enthalpy for generating mobile species at the samarium oxide-cobalt interface remain constant.

An important practical consideration is the extent of oxidation of SmCo_5 magnet powders during processing. Oxygen analyses by neutron activation show that the oxygen concentrations of sintered magnets prepared from powders are generally similar to the analyses of powders before sintering, and that oxygen analyses of arc-melted alloys are usually much lower. Hence, it appears that most of the oxidation of rare earth-cobalt alloys occurs during and after grinding, but before sintering and at or near room temperature.

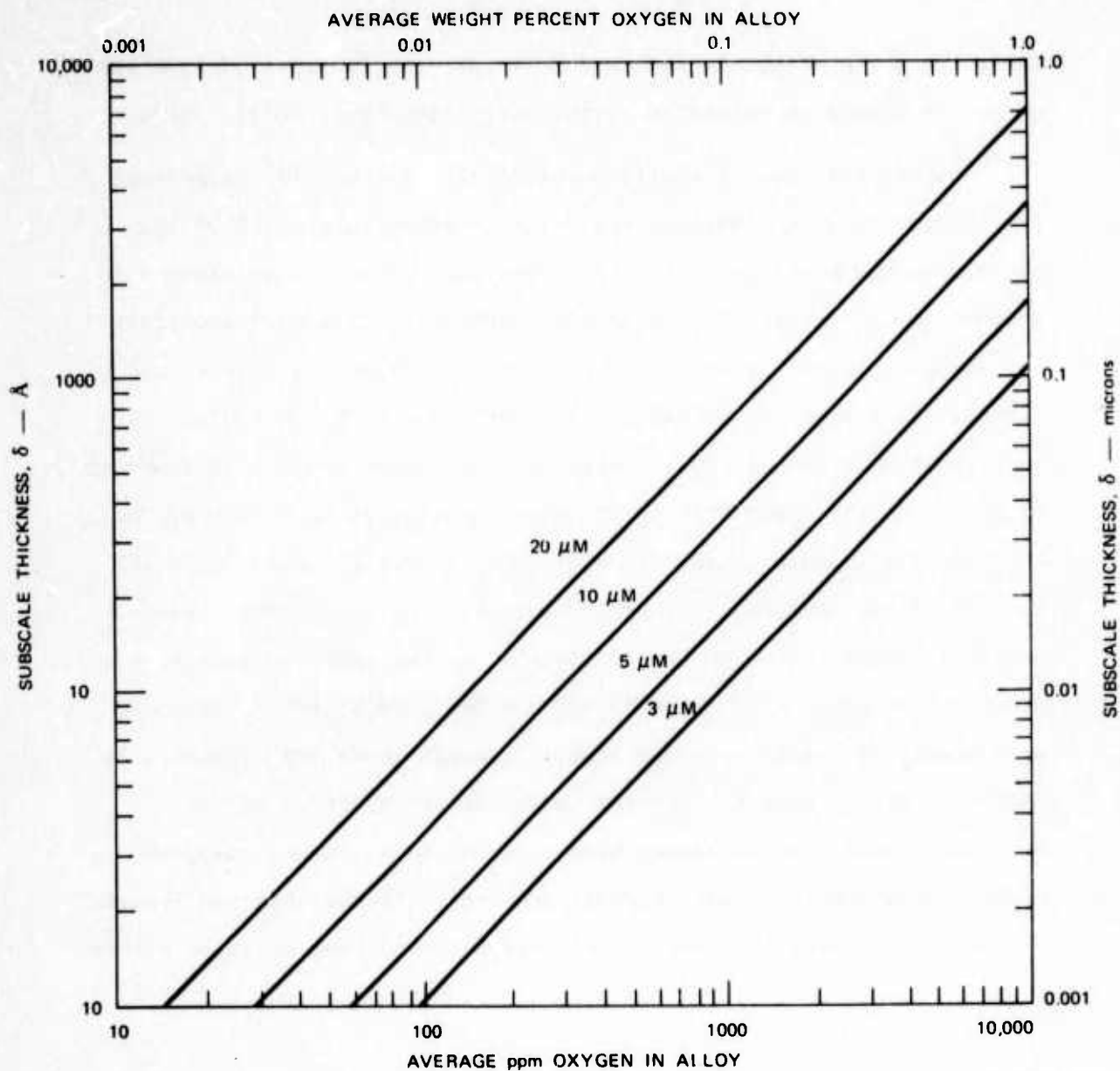
The adiabatic temperature rise caused by partial oxidation of SmCo_5 powders has been calculated. The assumptions for this calculation need to be emphasized. First, samarium is selectively oxidized to samarium sesquioxide and hence all of the measured oxygen in a sample can be assigned to Sm_2O_3 . Second, the sensible heat of oxidation is uniformly distributed in the alloy particle instantaneously. Because of rapid heat transfer in the metal, this approximation is probably adequate for a moderately slow oxidation process and small particles such as those required in preparing sintered magnets. The third assumption is that no heat is lost from the oxidizing alloy system. This approximation is probably valid for a large volume of particles and oxidation occurring fast enough so that heat transfer out of the crucible or particle container is not significant.

The temperature rise will be proportional to the amount of oxygen, the specific heat of SmCo_5 , and the heat of formation of Sm_2O_3 . The specific heat is about $0.1 \text{ cal g}^{-1} \text{ deg}^{-1}$ ($0.42 \text{ J g}^{-1} \text{ deg}^{-1}$) which was estimated from an assumption that the heat capacity is $7 \text{ cal g-atom}^{-1} \text{ deg}^{-1}$. The heat of formation of Sm_2O_3 at 298°K is $433,900 \text{ cal/mole}$.¹⁵ Consequently, the adiabatic temperature rise caused by an increase in oxygen is given by the following derived relation:

$$T_2 - T_1 = 0.095 (C_{O_2} - C_{O_1}) , \quad (4)$$

where C_O is the oxygen concentration in ppm. An increase of 1000 ppm of oxygen causes an adiabatic temperature increase of nearly 100°C .

Oxygen analyses in samarium-cobalt alloys generally range from a few hundred to a few thousand ppm after grinding, depending on the processing and particle size. This amount of oxygen is sufficient to account for an appreciable adiabatic temperature rise during oxidation. For example, a 100°C rise in temperature from 25 to 125°C is enough to account for a subscale thickness of about 100 \AA in a few hours. The relationship between subscale thickness and oxygen content is shown in Figure 15. A 100 \AA subscale thickness is equivalent to a 1000-ppm oxygen increase for a 3-micrometer-diameter SmCo_5 particle. Hence, for the particle sizes employed in sintered magnets, the observed increase in oxygen is consistent with the particle size, the expected temperature rise, the kinetics of oxidation, and the expected subscale thickness as a result of the temperature rise. Although these relationships do not prove that a temperature rise and internal oxidation by the diffusion-controlled mechanism have occurred to match the observed oxygen concentration, they at least show that all the observed results are compatible with the kinetics of internal oxidation of these alloys.



TA-8731-74R

FIGURE 15 SUBSCALE THICKNESS AS A FUNCTION OF OXYGEN CONTENT AND PARTICLE DIAMETER IN SmCo_5 MAGNET POWDER

CONCLUSIONS

Oxidation of SmCo_5 is selective, forming an extremely fine fibrous composite subscale of samarium oxide and cobalt. Samarium oxynitride is also observed when nitrogen is present in the oxidizing atmospheres. The oxide content of the subscale is about 39 vol%, and both phases are continuous. The fibrous microstructure is generally oriented in the subscale growth direction.

The oxidation kinetics are controlled by quasisteady-state diffusion of oxygen through the subscale to the subscale/alloy interface at an unusually rapid rate for solids. The subscale growth rate is too fast to be accounted for by lattice diffusion in either cobalt or samarium oxide, and rapid diffusion along the interface separating the oxide and cobalt phases within the subscale is apparently the rate-controlling process.

The apparent activation energy for the parabolic rate constant is 14 kcal/mol (58.8 k-J/mol). However, the rate of oxidation increases less rapidly above 750°C. Increased coarsening of the fibrous microstructure occurs with increasing temperature above 750°C and probably accounts for the apparent reduction in rate increase.

The composite microstructure is stable during the oxidation process, but recrystallization of the oxide is rapid on continued heating without oxygen.

The near room temperature oxidation kinetics adequately explain the amount of oxidation usually observed in magnet powders processed in ambient temperature atmospheres before sintering.

The oxidation behavior of PrCo_5 is identical with that of SmCo_5 .

REFERENCES

1. J. J. Becker: IEEE Trans Mag., 1963, MAG-4, p. 239.
2. H. Mildrum, A. E. Ray, and K. Strnat: Proceedings of the 8th Rare Earth Research Conference, pp. 21-30, T. A. Henrie and R. E. Lindstrom, eds., Reno, Nevada, 1970.
3. J. J. Becker: IEEE Trans. Mag., 1969, MAG-5, p. 211.
4. K. A. Gschneidner, Rare Earth Alloys, pp. 149-53, D. Van Nostrand, New York, 1961.
5. P. Kofstad: Nonstoichiometry, Diffusion, and Electrical Conductivity in Binary Metal Oxides, Chap. 12, Wiley-Interscience, New York, 1972.
6. T. L. Felmlee and L. Eyring: J. Inorg. Chem., 1968, vol. 1, pp. 660-66.
7. P. Kofstad: J. Inorg. Chem., 1968, vol. 1, p. 238.
8. J. S. Swisher: "Internal Oxidation," in Oxidation of Metals and Alloys, p. 238, edited by D. L. Douglass, American Society for Metals, Metals Park, Ohio, 1971.
9. J. Crank: The Mathematics of Diffusion, p. 117, Oxford Press, London, 1956.
10. A. U. Seybolt and C. H. Mathewson: Trans. AIME, 1935, vol. 117, p. 156.
11. G. D. Stone, G. R. Weber, and L. Eyring: "Mass Transport in Oxides," NBS Special Publication 296, p. 179, NBS, Washington, D.C., 1968.
12. C. D. Wirkus, M. F. Berard, and D. R. Wilder: J. Am. Ceram. Soc., 1967, vol. 50, p. 113.
13. M. F. Berard, C. D. Wirkus, and D. R. Wilder: J. Am. Ceram. Soc., 1968, vol. 51, p. 643.
14. V. B. Tare and H. Schmalzried: Z. Phys. Chem. N.F., 1964, vol. 43, p. 30.
15. C. E. Wicks, and F. E. Block: "Thermodynamic Properties of 65 Elements--Their Oxides, Halides, Carbides, and Nitrides," Bull. 605 U.S. Bureau of Mines, Government Printing Office, Washington, D.C., 1963.

III MICROSTRUCTURAL CHANGES IN SmCo_5 CAUSED BY OXYGEN SINTER-ANNEALING AND THERMAL AGING

INTRODUCTION

Microstructural changes accompanying the processing of rare earth magnets, based on SmCo_5 as the primary magnetic phase, can affect magnetic coercivity. A sluggish eutectoid decomposition of SmCo_5 into Sm_2Co_7 and $\text{Sm}_2\text{Co}_{17}$ occurring at temperatures below about 750°C has been reported.^{1,2} Microstructural changes resulting from (a) partial oxidation, (b) heating to sintering temperatures, and (c) thermal aging at intermediate temperatures are the subjects of the present study.

Oxidation of SmCo_5 is a rapid process, known to occur in air at measurable rates as low as 100°C . The oxidation is selective for samarium, producing a subscale consisting of β -cobalt and samarium oxide fibers³ oriented in the general direction of growth of the subscale.

The selective oxidation of samarium near the surface causes a samarium activity gradient within the metallic phases and outward diffusion of samarium to alloy with cobalt during a subsequent thermal heat treatment, which cannot be avoided in producing sintered magnets. This diffusion process causes depletion of samarium in the alloy core.

Two types of inclusions have been observed during the present study: the intermetallic compound, $\text{Sm}_2\text{Co}_{17}$, precipitates within samarium-depleted alloys of the SmCo_5 structure, and samarium oxide forms on cooling an oxygen-saturated solid solution alloy. Both types of inclusion may be nucleation sources for magnetic domains and thereby lower the intrinsic coercivity.

EXPERIMENTAL

The experimental procedure involved deliberate introduction of known amounts of oxygen into stoichiometric SmCo_5 by thermal oxidation of small polycrystalline cast pieces of this alloy. The average SmCo_5 grain size, which is controlled by solidification, was about 80 μm in these test specimens. Sintered magnets were also examined but they are generally unsuitable for microstructural examination because of their small grain size and porosity.

An oxidation temperature of 800°C was used. After oxidation, the specimens were annealed in oxygen-gettered argon at normal sintering temperatures, $1125 \pm 5^\circ\text{C}$, for 30 minutes, which was sufficient to provide a macroscopically homogeneous distribution of oxygen throughout the SmCo_5 alloy pieces.

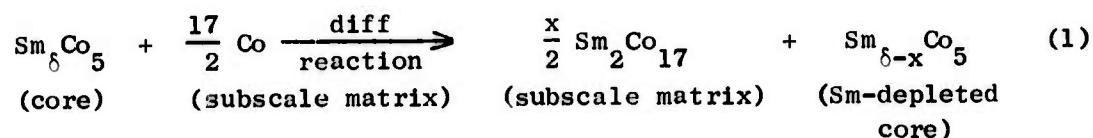
Microstructural determinations were made after oxidation, after annealing at sintering temperatures, and after a subsequent thermal aging at 800°C. This temperature was chosen because it is substantially below the sintering temperature and apparently above the eutectic decomposition temperature,² and the homogeneity range in SmCo_5 is believed to be extremely narrow. Furthermore, it has been shown that aging sintered SmCo_5 magnets at intermediate temperatures from 900 to 1000°C can often increase their magnetic coercivities.⁴ After their terminal heat treatment specimens were cooled by quick removal from the hot zone of the furnace. The microstructural examinations were made using reflection light microscopy, scanning electron microscopy, and electron beam microprobe analysis.

RESULTS

A. Oxide Subscale/ SmCo_5 Reaction at Sintering Temperatures

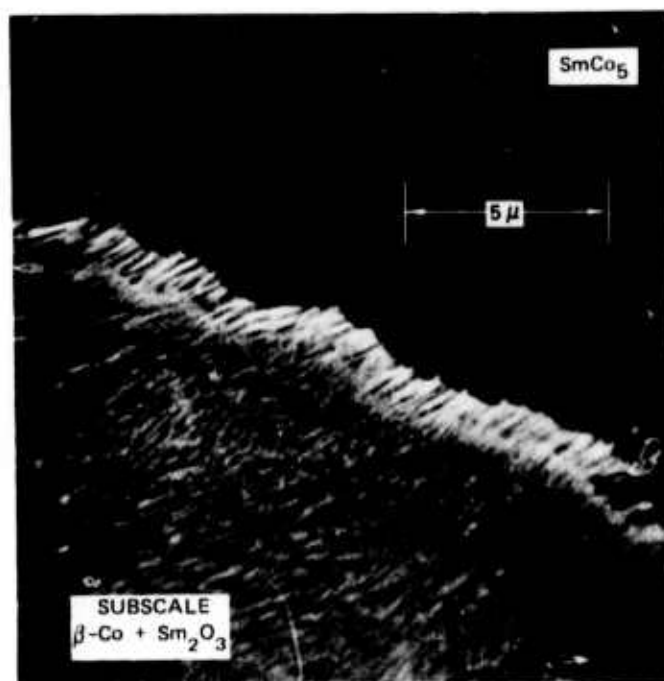
The oxide subscale formed during oxidation of SmCo_5 is shown in Figure 16. Subsequent heating in the absence of oxygen causes the existing oxide subscale to change rapidly. The fine samarium oxide fibers recrystallize into larger, more equidimensional particles. A zone that is partially depleted in samarium oxide forms adjacent to the unoxidized SmCo_5 core, and the few oxide particles in this oxide-depleted zone are considerably larger than those in the undepleted region of the subscale. Figure 17 shows the partially depleted zone on the right-hand side of the scanning electron micrograph.

The oxide particles and alloy phases have been identified by electron beam microprobe analysis. The metal matrix of the depleted region consists of a $\text{Sm}_2\text{Co}_{17}$ band sandwiched between SmCo_5 in the core and the remaining β -cobalt in the subscale matrix. This phase is produced during annealing because samarium is transported from the SmCo_5 core into the subscale region, where it reacts with cobalt. The solid-state diffusion reaction, which can be inferred from the observed microstructure and the samarium-cobalt phase diagram,⁵ is:



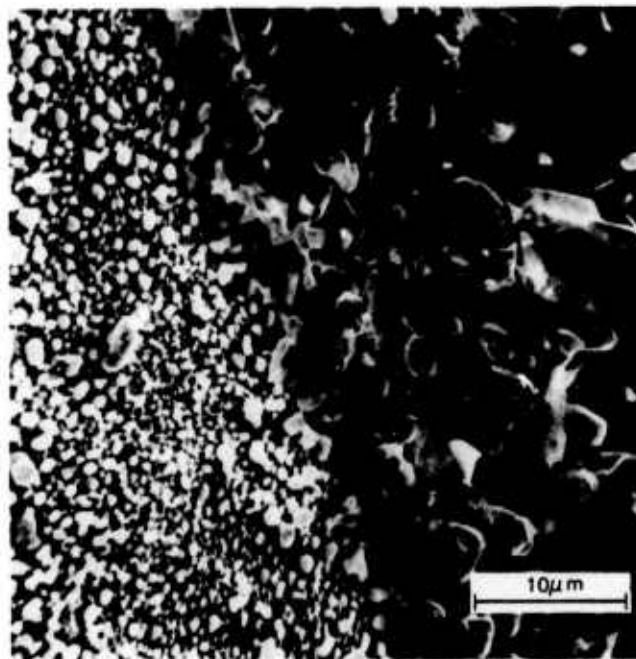
where $\delta \approx 1$.

During cooling from the annealing temperature, the homogeneity range of the SmCo_5 phase narrows and at the temperature where the composition of the alloy intersects the solvus (Figure 18), rejection of



TA-8731-65R

FIGURE 1 SCANNING ELECTRON MICROGRAPH OF THE SUBSCALE/SmCo₅ INTERFACE; OXIDIZED 1125°C, 2 MIN; ETCHED 50 HNO₃, 30 H₂SO₄, 20 H₂O



SA-8731-93

FIGURE 17 BOUNDARY OF THE OXIDE DEPLETED ZONE
(RIGHT SIDE) WITHIN THE SUBSCALE AFTER
ANNEALING AT 1125°C

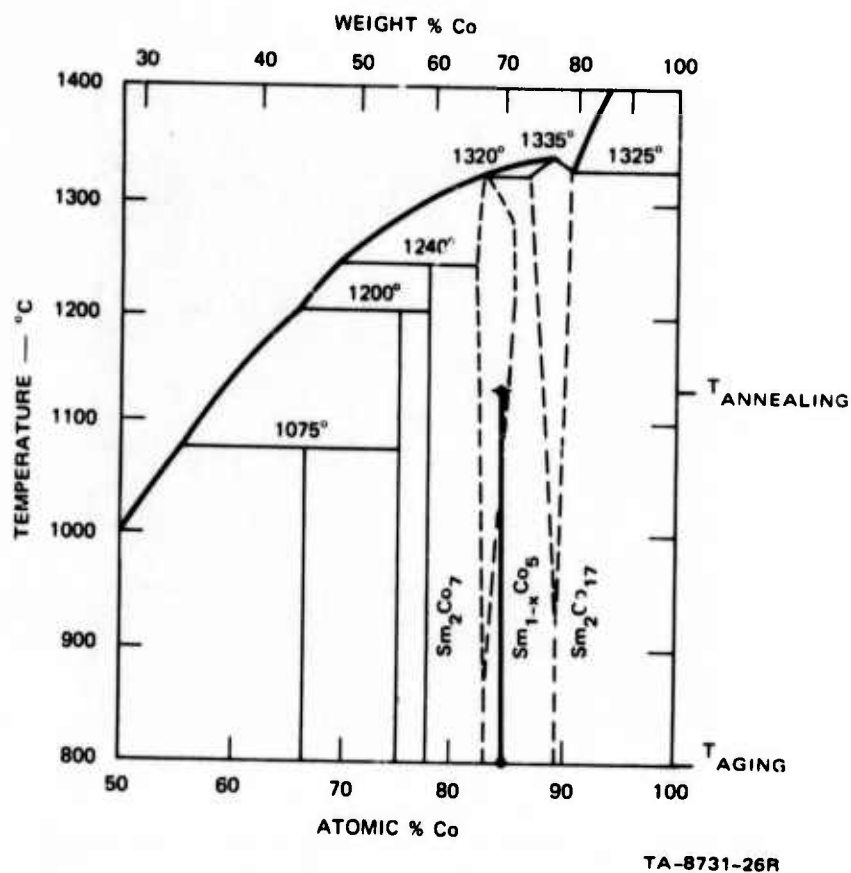
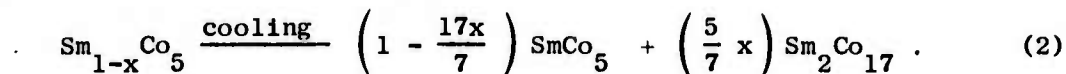


FIGURE 18 SAMARIUM-COBALT PHASE DIAGRAM AFTER BUSCHOW AND VAN DER GOOT (5)

the excess cobalt occurs as precipitation of $\text{Sm}_2\text{Co}_{17}$. If $\delta = 1$, then within the core:



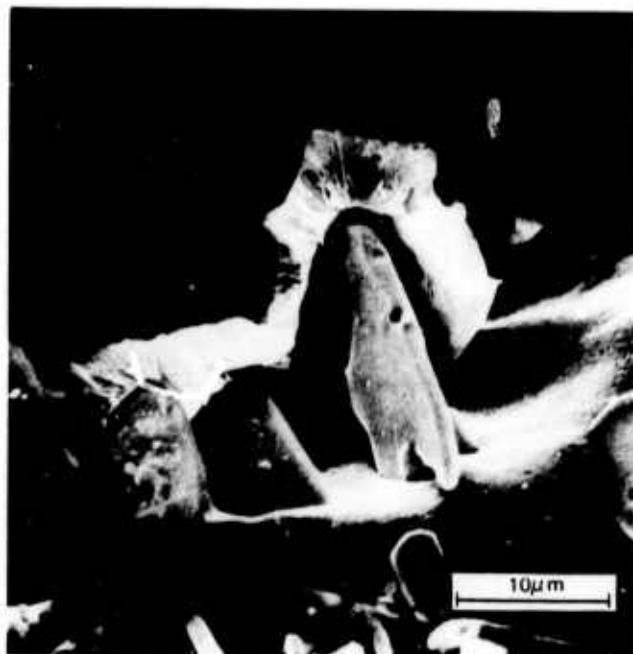
Annealing also causes oxides in the subscale to dissolve partially and oxygen migrates into the core. This process accounts for the reduction in total volume of the oxide particles observed within the depleted zone of the subscale. Oxide dissolution is a direct result of the greater solubility of oxygen in SmCo_5 at the annealing temperature, 1125°C , than at the oxidation temperature, 800°C .

The scanning electron micrograph shown in Figure 19 shows essentially all of the features resulting from annealing a partially oxidized SmCo_5 specimen. The original interface separating the subscale from the SmCo_5 core is shown. Below this boundary is the region containing a matrix of $\text{Sm}_2\text{Co}_{17}$ and large recrystallized samarium oxide particles. A two-phase alloy region consisting of a matrix of SmCo_5 and fine $\text{Sm}_2\text{Co}_{17}$ precipitates exists above the boundary. A relic of the original fibrous subscale is also shown.

B. Oxygen Solubility and Samarium Oxide Precipitation in SmCo_5

Note that a small samarium oxide particle appears in the SmCo_5 core region above the interface in Figure 19. This particle was produced by oxygen dissolved in SmCo_5 during annealing and subsequently precipitated on cooling.

The amount of oxygen transferred from the oxide subscale into SmCo_5 during annealing is the excess solubility at 1125°C over the solubility at 800°C . This excess solubility was determined as follows. The oxide content within the SmCo_5 core of an aged specimen was calculated metallographically. Large oxide grains are produced during the thermal aging treatment by a solution-reprecipitation process. These oxide grains



SA 8731-94

FIGURE 19 BOUNDARY BETWEEN THE OXIDE DEPLETED
DEPLETED ZONE AND THE SmCo_5
CORE

appear black under reflected light; see Figure 20. Consequently, a Quantimet image analysis was performed on several sections and the area percent of oxide was determined. The average area of oxide grains was determined to be $2.6 \pm 0.4\%$. The area percent is equal to the volume percent for randomly distributed equidimensional particles in a dilute suspension. The excess solubility of oxygen was determined from the volume of oxide in the SmCo_5 core after aging the specific gravities of Sm_2O_3 and SmCo_5 and their stoichiometries. This calculation involves the implicit assumption that all of the soluble oxygen in excess of the 800°C solubility was precipitated as measurably large oxide grains during the 45 minute aging treatment at 800°C . The precipitation and growth of extremely large oxide grains during this period, as shown in Figure 20, indicates that this assumption is probably valid. The metallographic determination of the excess oxygen solubility, calculated from the 2.6% oxide area is $0.35 \pm 0.05 \text{ wt\%}$ ($3500 \pm 500 \text{ ppm}$).

A measurement was also made of the thickness and the area of the oxide subscale depletion zone formed during annealing. From inspection of several scanning electron micrographs it was estimated that about 75% of the oxide in the depleted zone was dissolved. The calculation indicated that the excess solubility of oxygen in SmCo_5 is $(C_{\text{O}_{1125}} - C_{\text{O}_{800}}) \approx 0.35 \text{ wt\%}$, but it is impossible to put error limits on this estimate. Nevertheless, there is good agreement between the amount of oxygen appearing inside the samples after aging and the amount of oxygen depleted from the subscale during annealing.

Although the oxide grains observed in the aged specimens were sometimes larger than $100 \mu\text{m}$, oxide inclusions within the annealed and rapidly cooled specimens are generally smaller than $1 \mu\text{m}$. Any exceptions can usually be traced back to larger oxide inclusions that were present in the cast alloy before the deliberate oxidation step.

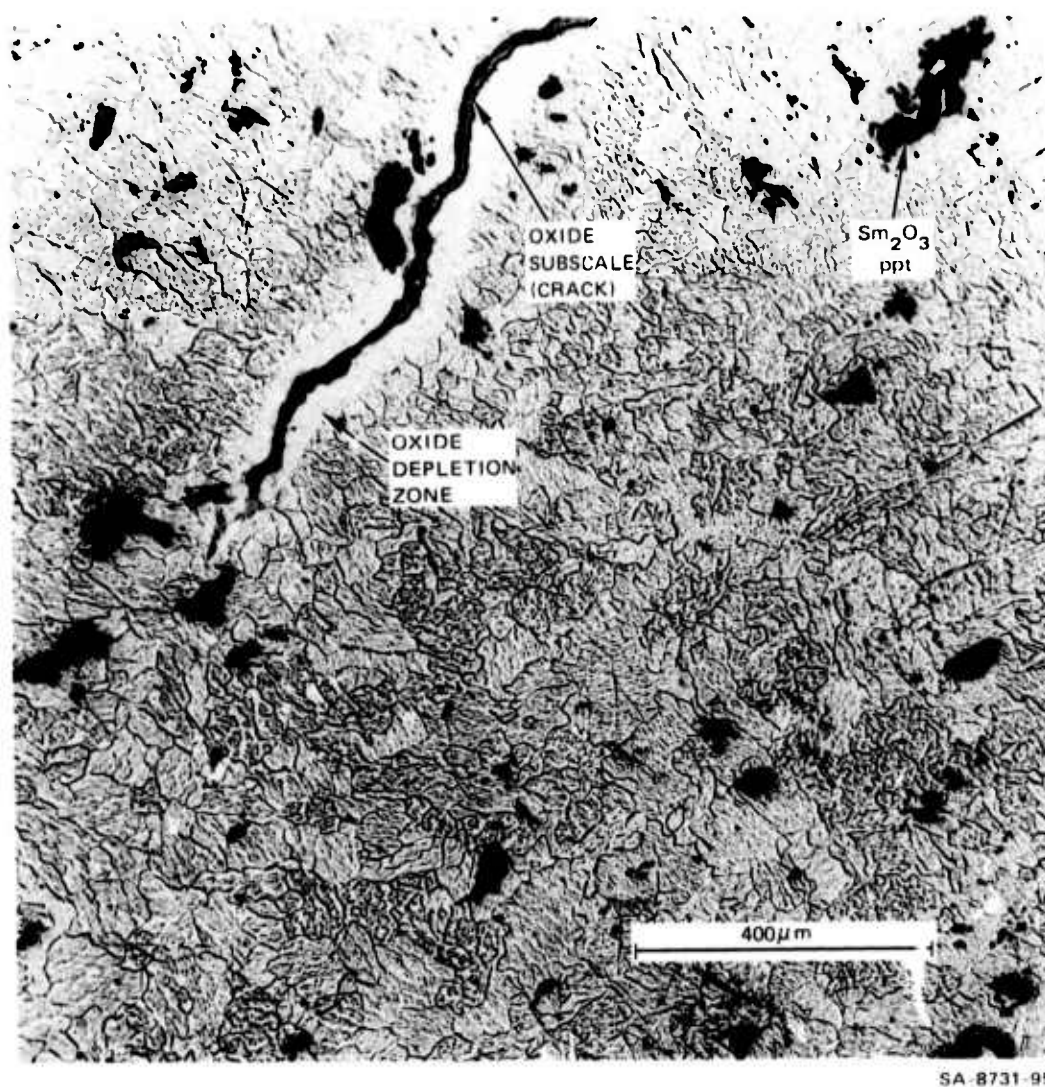


FIGURE 20 OXIDE PRECIPITATES IN THE SmCo_5 GRAINS
AFTER OXYGEN SATURATION AT 1125°C AND
AGING AT 800°C

The annealed specimen of Figure 21 shows a region of low oxide inclusion population in the upper part of the figure and a region of high oxide inclusion population in the lower half of the figure. High population regions were less common than low population regions in all of the specimens examined. The boxed area in Figure 21 was picked at random within the high inclusion population region. The average oxide volume fraction, F_f , was determined from

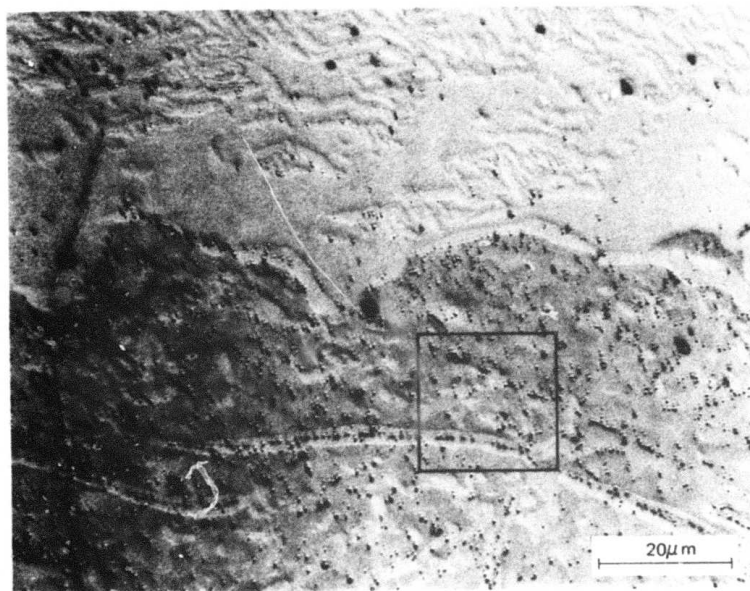
$$V_f = \frac{\pi}{6} N_s \bar{d}_p^3 \quad (3)$$

where N_s is the particle population per unit area, and \bar{d}_p is the mean particle diameter. The particle population in the boxed area was 3.0×10^7 inclusions/cm² and the resulting oxide volume fraction was 0.03, which is similar to the oxide volume fraction observed in thermally aged specimens. Hence, in the high population regions, most of the dissolved oxygen has precipitated as small but visible inclusions.

However, a large amount of oxygen known to be present in the specimens was not accounted for in the low population regions of the annealed specimens. This oxygen may occur as small inclusions below the resolution limit, as coherent oxygen-rich zones, and as a supersaturated solute.

Small oxide inclusions have also been observed within the primary SmCo_5 grains of both experimental and commercial sintered magnets. These inclusions usually appear within SmCo_5 grains rather than at grain boundaries in polished sections under bright field illumination as shown in Figure 22. Because excess samarium was present in this alloy precipitation of $\text{Sm}_2\text{Co}_{17}$ has not occurred.

Fracture surfaces have also been examined using scanning electron microscopy. Oxide particles are rarely observed unless the specimen surface has been previously etched to expose them. An etched fracture



SA-8731-108

FIGURE 21 SmCo₅ QUENCHED FROM 1125°C TO R
ROOM TEMPERATURE IN ARGON—
SHOWING SMALL SCALE OXIDE
INCLUSIONS

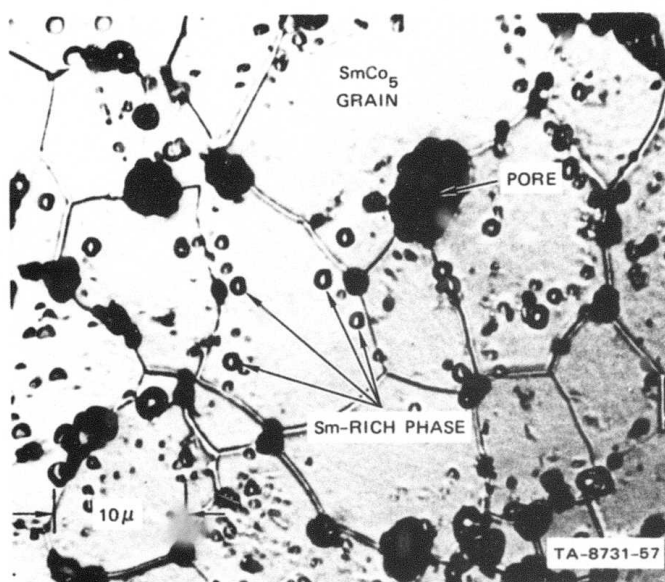


FIGURE 22 POLISHED SECTION OF A COMMERCIAL SmCo₅ POWDER MAGNET SINTERED WITH EXCESS SAMARIUM

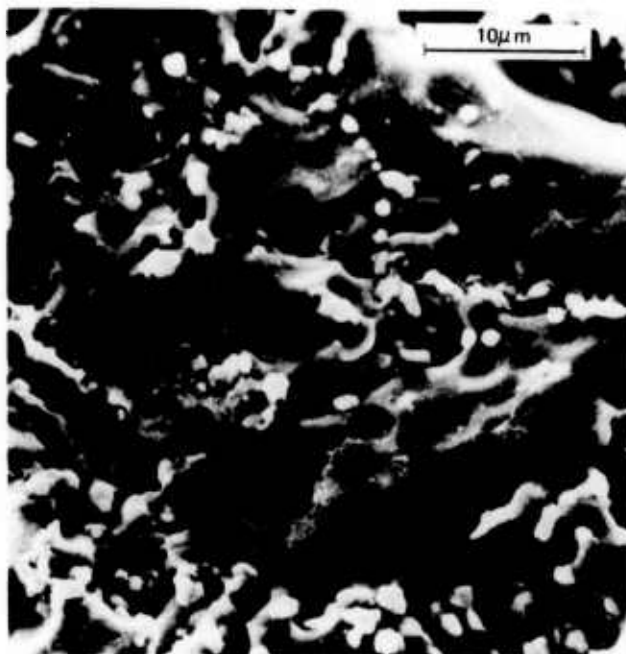
surface of a sintered SmCo_5 magnet is shown in Figure 23. The white spots in this scanning electron micrograph are oxide inclusions that have been left after the matrix metal was dissolved, and the dark areas are pores.

C. Precipitation of $\text{Sm}_2\text{Co}_{17}$ in SmCo_5

There are two stages of $\text{Sm}_2\text{Co}_{17}$ precipitation within SmCo_5 that result from partial oxidation followed by sintering or annealing. The primary stage results from sinter-annealing and subsequent cooling and is described by Equations (1) and (2). As a single phase alloy is quenched from 1125°C , precipitates of $\text{Sm}_2\text{Co}_{17}$ occur within the SmCo_5 grain. These precipitates are about $1\ \mu\text{m}$ wide and a few micrometers long. They have been identified from fluorescent intensities of cobalt and samarium obtained by nondispersive X-ray analysis of the precipitates in a scanning electron microscope. These precipitates often occur in clusters as shown in Figure 24. One small samarium oxide precipitate also appears near the upper edge of this micrograph.

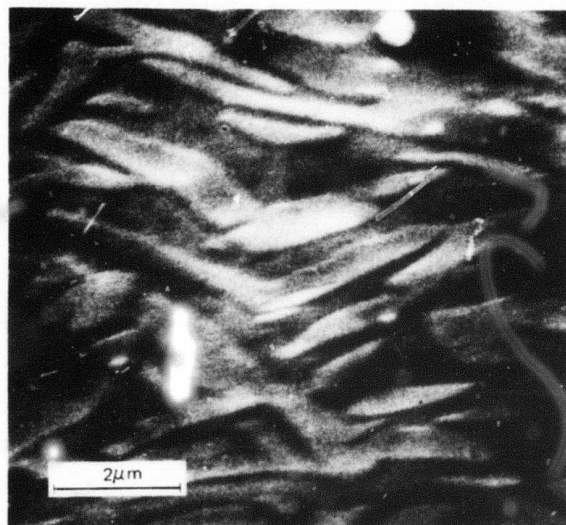
There was no tendency for $\text{Sm}_2\text{Co}_{17}$ to precipitate at the SmCo_5 grain boundaries during the primary stage of $\text{Sm}_2\text{Co}_{17}$ precipitation. It should be emphasized that primary precipitation of $\text{Sm}_2\text{Co}_{17}$ within the SmCo_5 grains occurs whenever excess cobalt is exsolved from a samarium-depleted SmCo_5 phase during cooling, whether the cause of samarium depletion in the alloy is samarium oxidation, samarium vaporization, or an off-stoichiometric initial composition.

Primary $\text{Sm}_2\text{Co}_{17}$ precipitation is evidently complete on cooling from 1125°C . A series of aging tests for various times to 24 hours at 800°C using pieces from a samarium-depleted double-melted ingot (not oxidized) showed no increase in the amount of $\text{Sm}_2\text{Co}_{17}$ or any apparent rearrangement of $\text{Sm}_2\text{Co}_{17}$ as a result of aging.



SA-8731-97

FIGURE 23 SAMARIUM OXIDE PARTICLES IN A
SINTERED SmCo_5 MAGNET EXPOSED
BY ETCHING (SEM)



SA-8731-98

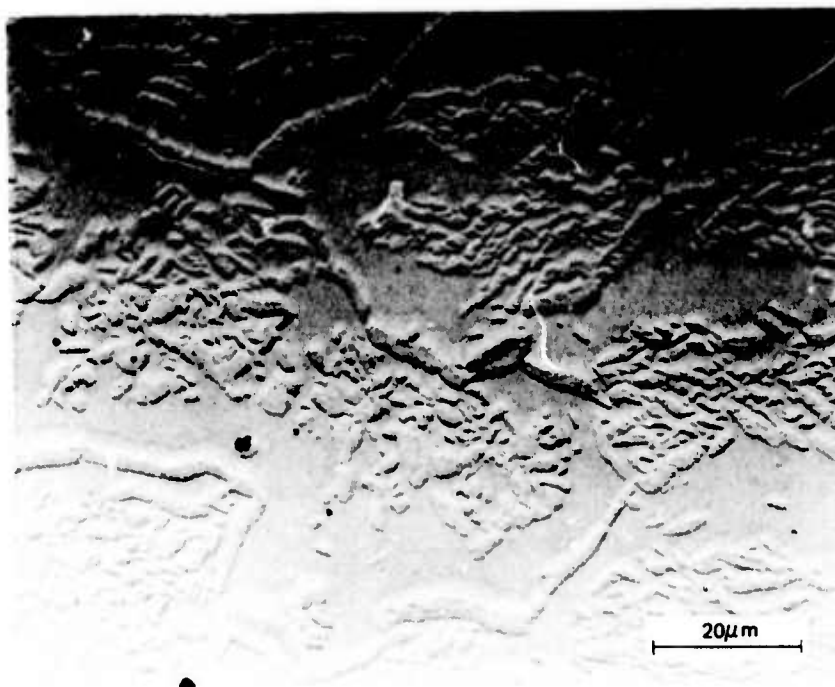
FIGURE 24 SCANNING ELECTRON MICROGRAPH OF
 $\text{Sm}_2\text{Co}_{17}$ PRECIPITATES IN SmCo_5

The second stage of $\text{Sm}_2\text{Co}_{17}$ precipitation is caused by rejection of oxygen dissolved in SmCo_5 and formation of Sm_2O_3 . As already mentioned, precipitation of Sm_2O_3 is limited and does not occur to any appreciable extent during quenching, but becomes complete with thermal aging. During the aging process, both samarium and oxygen are collected into a few large samarium oxide grains, and they must diffuse out of the SmCo_5 grains and be transported over distances relatively large when compared with the primary SmCo_5 grain size. This further depletion of samarium from the SmCo_5 grains causes rejection of additional $\text{Sm}_2\text{Co}_{17}$. Micrographs indicate that this secondary precipitation of $\text{Sm}_2\text{Co}_{17}$ occurs at the SmCo_5 grain boundaries rather than throughout the grains. This process is particularly evident in the micrograph of the aged specimen in Figure 25.

The precipitation of large Sm_2O_3 particles is probably controlled by rapid grain boundary diffusion of samarium. This process causes bulk depletion of samarium from the region immediately adjacent to SmCo_5 grain boundaries and precipitation of $\text{Sm}_2\text{Co}_{17}$ in the samarium-depleted zone, which is about 2 μm wide. This model is consistent with the observed kinetics of solid state sintering of SmCo_5 , which indicate that sintering in SmCo_5 is also controlled by a grain boundary diffusion process⁶.

Precipitation of $\text{Sm}_2\text{Co}_{17}$ has also been observed in sintered magnets. However, the $\text{Sm}_2\text{Co}_{17}$ precipitate size is apparently independent of the SmCo_5 matrix grain size ($\approx 5 \mu\text{m}$), and the $\text{Sm}_2\text{Co}_{17}$ precipitates are about the same size as the small SmCo_5 grains.

The precipitation of fine $\text{Sm}_2\text{Co}_{17}$ particles in samarium-depleted alloys contrasts sharply with the Sm_2Co_7 phase in samarium-rich alloys. In the latter case the SmCo_5 grains were clean and Sm_2Co_7 occurred only as separate grains outside the SmCo_5 grains.



SA-8731-109

FIGURE 25 SmCo_5 QUENCHED FROM 1125°C TO ROOM TEMPERATURE AND AGED AT 800°C —SHOWING $\text{Sm}_2\text{Co}_{17}$ INCLUSIONS

Examination of many precipitates by electron beam microprobe analysis produced no evidence of $\text{Sm}_2\text{Co}_{17}$ within SmCo_5 grains or an eutectoid decomposition. However, the temperature (800°C) was probably too high and the time (24 hours maximum) too short to produce visible microstructural changes from an eutectoid reaction or other solid-state disproportionation reaction.

DISCUSSION OF Sm_2O_3 AND $\text{Sm}_2\text{Co}_{17}$ INCLUSIONS AND THE INTRINSIC COERCIVITY OF SmCo_5

The highest published room temperature intrinsic coercivity in sintered SmCo_5 magnets is $H_{c1} = 43 \text{ kOe}$.⁷ A sintered SmCo_5 magnet with a room temperature intrinsic coercivity of 43 kOe has also been produced and measured in our laboratory. However, this is only about 15% of the theoretical coercivity, $2K/M_s$, where K is the magnetocrystalline anisotropy and M_s is the saturation magnetization. Furthermore, sintered SmCo_5 magnets usually have much lower coercivities than 43 kOe, and SmCo_5 powders and samarium-depleted sintered magnets usually have intrinsic coercivities well below 20 kOe. Because of the high magnetocrystalline anisotropy, coherent rotation of domains and curling cannot occur at the comparatively low fields at which magnetic reversal actually occurs.

Magnetic domain nucleation and domain-wall pinning are the factors that probably control coercivity in polycrystalline magnets. For a detailed review, see Livingston.⁸ Metallic and oxide inclusions may impede domain-wall movement and increase coercivity. However, these same defects may act as nucleation sites for new domains and decrease coercivity. Magnet processing operations that lead to oxidation and insufficient samarium in the alloy, are known to lower coercivity. The present experimental results show that oxidation and samarium depletion cause precipitation of Sm_2O_3 and $\text{Sm}_2\text{Co}_{17}$ inclusions within SmCo_5 grains. Magnet processing operations that decrease these inclusions are known to raise coercivity. Consequently, nucleation of reverse domains by these inclusions, rather than domain-wall pinning, apparently reduces coercivity.

Additional arguments against a domain-wall pinning model can be made based on other experimental information. Sintered rare earth cobalt magnets are made by aligning the powder (easy axis crystallographic parallel orientation). During sintering the crystallographic orientation is maintained but the specimen is thermally demagnetized. If domain-wall motion controlled the coercivity, then magnetization of the sintered specimen should require a high field, similar to H_{c1} . The experimental evidence is that magnetization nearly equal to M_s can be obtained in a thermally demagnetized specimen at fields much lower than H_{c1} .

Domains have been observed in a large number of SmCo_5 grains in which $\text{Sm}_2\text{Co}_{17}$ inclusions have been introduced by samarium depletion. Bending of domain walls around these inclusions⁹ has not been observed in our laboratory. In all cases the domain walls seem to be oblivious to the presence of the cobalt-rich inclusions. Small oxide particles, $\leq 1 \mu\text{m}$, such as those shown in the gas-quenched specimen of Figure 21 also do not appear to have a preferred locus coincidental with domain walls and, therefore, are evidently not pinning domain walls.

It appears that an inclusion domain-nucleation model can explain some of the confirmed phenomenological relations between samarium-cobalt magnet processing and the resulting intrinsic coercivity. An example is the observed drastic decrease in coercivity if excess samarium is not present during sintering.¹⁰ According to this hypothesis, Sm_2O_3 and $\text{Sm}_2\text{Co}_{17}$ inclusions can heterogeneously nucleate reverse domains. Inclusions resulting from the reported^{1,2} eutectoid decomposition may behave similarly. Magnetic coercivity of a grain and of a sintered aggregate will decrease as the population of inclusions increases.

Rather than present a lengthy speculative discussion of these phenomena and their possible association with inclusions, effects with possible causes are listed in Table IV.

Table IV

SOME EFFECTS INVOLVING MAGNETIC COERCIVITY IN SmCo_5 AND THEIR POSSIBLE CAUSES

Effects	Possible Causes
<ul style="list-style-type: none"> Excess Sm is required to obtain high H_{c1} in sintered magnets Aging at 900 to 1000°C increases H_{c1} in sintered magnets containing excess Sm Very short time high temperature annealing (unpublished) in plasma lowers H_{c1} in single particles Low temperature thermal aging reduces coercivity¹² but results can be reversed by heating to intermediate temperature (2900°C) Excessive sintering temperature lowers H_{c1} Etching increases H_{c1} in single particles¹⁴ Decrease in H_{c1} with long time aging at room temperature in single particles is accelerated in the presence of oxygen Overgrinding decreases H_{c1} in single particles¹⁶ Grinding in liquid nitrogen improves room temperature H_{c1} of particles compared with room temperature grinding The outer shell ($\sim 200 \text{ \AA}$) of sintered magnet bodies has low coercivity (unpublished) 	<p>Excess Sm replenishes that depleted from SmCo_5 by oxidation and prevents exsolving of $\text{Sm}_2\text{Co}_{17}$ precipitates.</p> <p>Aging scavenges Sm_2O_3 in large grains and removes fine oxide inclusions from the primary SmCo_5 grains.</p> <p>Surface oxide dissolves in SmCo_5 and reprecipitates as submicron oxide inclusions. Insufficient time or temperature is available to scavenge Sm_2O_3 into large grains. Also, there is no source of Sm to replenish that lost by oxidation, hence $\text{Sm}_2\text{Co}_{17}$ is precipitated.</p> <p>Eutectoid decomposition,^{1,2} usually in an incipient stage?</p> <p>Oxygen solubility increases with temperature and causes more inclusions of samarium oxide; also discontinuous grain growth may occur.</p> <p>Etching removes the oxide subscale¹³ which is a source of domain nucleation at particle surfaces.</p> <p>Selective surface oxidation of Sm occurs to form the oxide sub-scale. This may not happen if the system were truly free of oxygen. Eutectoid decomposition may make a contribution.</p> <p>Surface oxidation increases per unit volume of material during grinding or following grinding and exposure to air. Grinding in the presence of small amounts of oxygen is much more deleterious than grinding in lesser amounts of oxygen.</p> <p>The oxidation kinetics are reduced at the lower temperature of liquid nitrogen.</p> <p>Oxidation or loss of Sm by evaporation causes inclusions to form--this has been observed metallographically.</p>

CONCLUSIONS

It is now clear that internal surfaces occur in primary SmCo_5 grains of sintered magnets and result from precipitation of fine $\text{Sm}_2\text{Co}_{17}$ and Sm_2O_3 inclusions. The oxygen solubility determinations for cast SmCo_5 show that unusually large amounts of oxygen can dissolve in SmCo_5 at sintering temperatures. For careful processing operations, where oxygen contamination is kept below 3500 ppm, all of the oxygen will be dissolved in SmCo_5 during sintering. The normal cooling of sintered magnets will leave approximately submicron oxide particles within the SmCo_5 grains, which have also been observed in sintered magnets. Much of the oxygen in quenched SmCo_5 is unaccounted for and may be present as supersaturated oxygen, coherent oxygen-rich zones, and unresolvable oxide inclusions. Oxide precipitates can be removed from the SmCo_5 magnet grains by an aging-recrystallization treatment that tends to collect the oxygen in a few large oxide grains without changing the grain size of SmCo_5 . Selective oxidation of the alloy also affects the formation of fine $\text{Sm}_2\text{Co}_{17}$ precipitates within SmCo_5 grains by depleting samarium and shifting the composition. Precipitation of $\text{Sm}_2\text{Co}_{17}$ occurs in two sequential stages, the first occurs randomly within SmCo_5 on cooling from sintering temperatures and the second occurs near SmCo_5 grain boundaries as a result of the subsequent thermal aging to remove oxygen by recrystallization.

Although oxidation cannot be entirely prevented, primary and secondary formation of $\text{Sm}_2\text{Co}_{17}$ precipitates can be prevented by having excess samarium present in the powder compact to replace the samarium depleted from SmCo_5 grains.

REFERENCES

1. F. J. A. Den Broeder and K. H. J. Buschow, J. Less-Common Metals, 29, 65 (1972).
2. K. H. J. Buschow, J. Less-Common Metals, 29, 283 (1972).
3. R. W. Bartlett and P. J. Jorgensen, "Microstructure and Growth Kinetics of the Fibrous Composite Subscale Formed by Internal Oxidation of SmCo_5 ," submitted to Met. Trans. (June 1973).
4. M. G. Benz and D. L. Martin, J. Appl. Phys., 42, 2786, (1971).
5. K. H. J. Buschow and A. S. Van der Goot, J. Less Common Metals, 14, 323 (1968).
6. P. J. Jorgensen and R. W. Bartlett, "Kinetics of Solid-State Sintering in SmCo_5 ," to be submitted.
7. K. H. J. Buschow, P. A. Naastepad, and F. F. Westendorp, IEEE Trans. Mag. 6, 301 (1970).
8. J. D. Livingston, "Present Understanding of Coercivity in Cobalt-Rare Earths," to be published in AIP Conference Proceedings (1972).
9. H. Zijlstra, J. Appl. Phys. 41, 4881 (1970).
10. M. G. Benz and D. L. Martin, Appl. Phys. Letters, 17, 176 (1970).
11. M. G. Benz and D. L. Martin, J. Appl. Phys., 42 2786 (1971).
12. F. F. Westendorp, J. Appl. Phys., 42, 5727 (1971).
13. F. F. Westendorp, Sol. State Commun. 8, 139 (1970).
14. J. J. Backer, J. Appl. Phys. 41, 1055 (1970).
15. F. F. Westendorp, IEEE Trans. Mag. 6, 472 (1970).
16. K. J. Strnat, Cobalt, 36, 133 (1967).
17. K. J. Strnat, J. C. Olson, and G. Hoffer, J. Appl. Phys., 39, 1263 (1968).

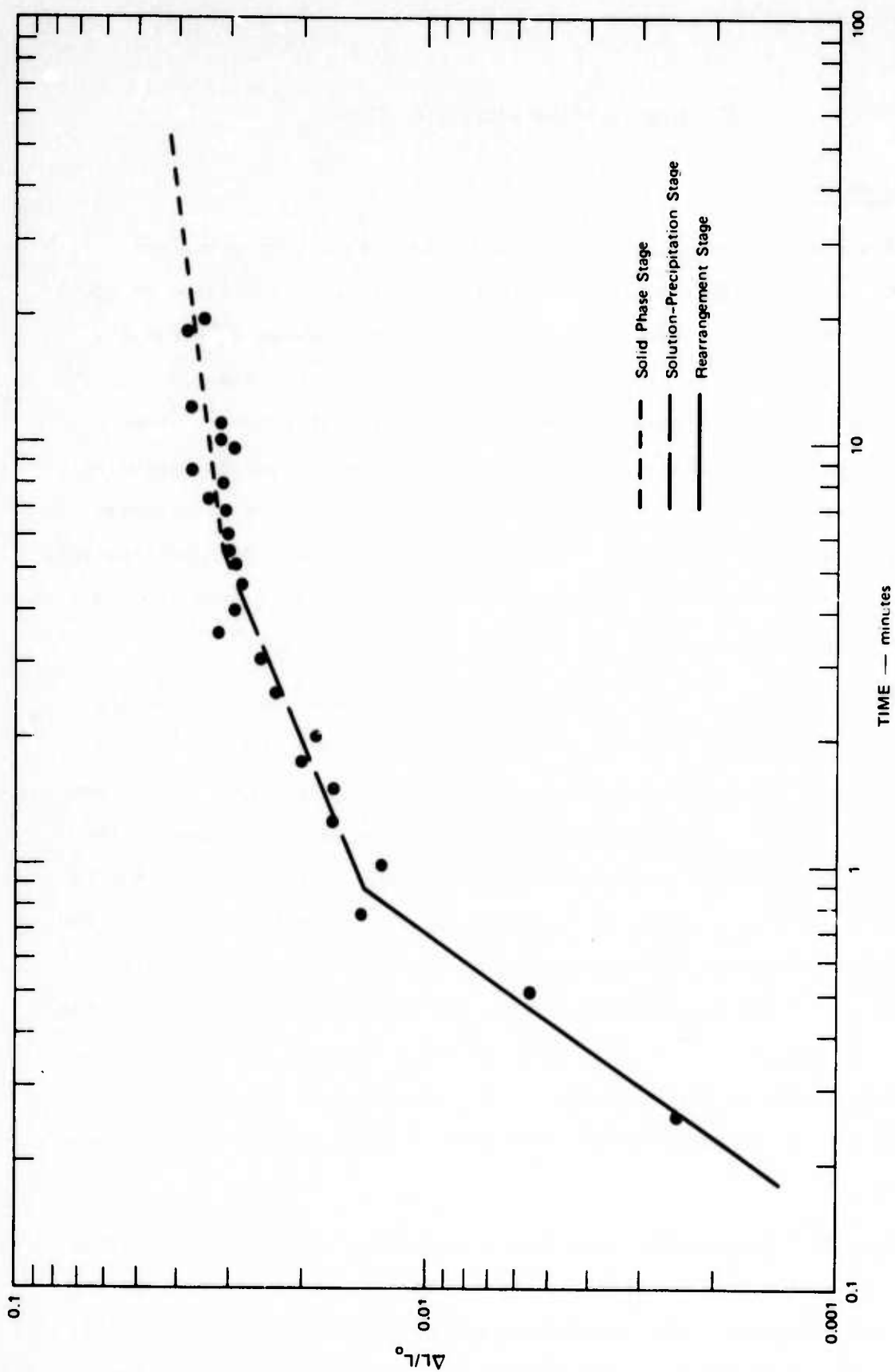
IV LIQUID PHASE SINTERING OF SmCo_5

Introduction

The compound SmCo_5 can be fabricated into excellent permanent magnets using techniques based on powder metallurgy. The alloy is ground into a fine powder, aligned in a magnetic field, pressed to achieve a maximum green density, and finally sintered in an inert atmosphere. The sintering process has been studied by several investigators¹⁻¹¹ and Benz and Martin¹⁰ provide an excellent list of references on sintering of rare earth-cobalt alloys. Cech² discovered that off-stoichiometry compositions rich in samarium sinter to high densities and simultaneously attain high coercivities. The magnetic properties are extremely sensitive to the final heat treatment and composition of the alloy.

The sintering of SmCo_5 magnets is usually accomplished by adding a samarium-rich phase (60 wt% Sm + 40 wt% Co) to SmCo_5 powder.¹⁰ The samarium-rich phase becomes liquid during the sintering process,¹² and therefore liquid-phase sintering kinetics are expected to control the initial stages of sintering. The liquid-phase sintering process may be divided into three stages: (1) rearrangement on formation of the liquid phase, (2) solution and precipitation of the solid phase, and (3) coalescence or solid-phase sintering with the formation of a solid skeleton. These three stages can be identified during isothermal sintering if the linear shrinkage of a powder compact is determined as a function of sintering time and plotted logarithmically. Figure 26 shows these stages for SmCo_5 .

Kingery¹³ has derived equations to describe liquid-phase sintering during the solution-precipitation stage. The equations are derived for spherical particles, complete wetting of the solid by the liquid, solution of the solid in the liquid phase, and constant grain size. The



TA-8731-39

FIGURE 26 ISOTHERMAL TIME DEPENDENCE OF SHRINKAGE OF SmCo_5 COMPACTS AT 1123°C

rate-controlling step may be diffusion in the liquid phase or the phase boundary (solid/liquid) reaction leading to dissolution. The equation that describes liquid diffusion-controlled sintering is,

$$\Delta L/L_o = \left[\frac{6K_2 \delta D X_o \gamma_{LV} V_o}{K_1 RT} \right]^{1/3} r^{-1/3} t^{1/3} \quad (1)$$

where K_1 and K_2 are dimensionless constants approximately equal to 0.5 and 1, respectively; δ is the thickness between particle-particle contact points; D is the diffusion coefficient of the slowest diffusing species in the liquid phase; and X_o is the mole fraction of SmCo_5 in the liquid phase at infinite radius of curvature; γ_{LV} is the liquid-vapor surface energy; V_o is the molar volume of SmCo_5 ; r is the particle radius, t is time; and $\Delta L/L_o$ is the linear shrinkage.

If the sintering kinetics are controlled by a dissolution process, the kinetics can be described by the following equation,

$$\Delta L/L_o = \left[\frac{2k' K_2 \gamma_{LV} X_o V_o}{K_1 RT} \right]^{1/2} r^{-1} t^{1/2} \quad (2)$$

where k' is the appropriate rate constant multiplied by an atomic jump distance.

Understanding the sintering mechanism and the parameters that affect sintering, such as amount of the liquid phase, particle size, time, and temperature, should provide the means for better control over the sintering process.

Experimental Procedure and Results

SmCo_5 powders were made for this study by arc melting the elements. The resulting alloy was ground in an alumina ball mill using sodium-gettered hexane as the milling fluid. The samarium and cobalt concentration of the alloy were determined, following milling, by titration with EDTA which is accurate within ± 0.1 wt%. The alloy composition was then adjusted to 37 wt% samarium and 63 wt% cobalt by adding the appropriate amount of the 60 wt% samarium + 40 wt% cobalt alloy. Slightly different alloy compositions obtained from the arc melting allowed the initial amount of samarium-rich liquid phase to be varied from 1.5 wt% to 13.8 wt%.

The oxygen content of the alloys was determined by neutron activation analysis and final alloy compositions were calculated based on the assumption that the oxygen was present as Sm_2O_3 . The 1.5 wt% liquid phase alloy had an oxygen concentration of 1.17 wt% and hence a final composition of 68.0 wt% cobalt. The 11.2 wt% liquid phase alloy with a 12.6 micron particle size had an oxygen concentration of 0.75 wt% and a final composition of 66.13 wt% cobalt, while the 19.6 micron particle size material contained 0.84 wt% oxygen and therefore a final composition of 66.6 wt% cobalt. It should be noted that the initial amount of liquid phase depends only on the original SmCo_5 alloy composition. The above association of final composition and the initial amount of liquid phase was used for identification purposes only.

Disk-shaped specimens, 1.0 inch in diameter by 0.13 inch thick, were fabricated by die pressing at 30,000 psi in the absence of a magnetic field. The specimens were placed on a molybdenum support in a furnace employing a graphite heater surrounded by oxygen-gettered argon. The shrinkage was recorded by time-lapse photography, and the data were read from the films by means of a Telereadex film analyzer.

The shrinkage was measured over a temperature range between 1032 and 1165°C. A typical shrinkage isotherm obtained at 1123°C is shown in Figure 26. Experiments of this type usually exhibit some experimental scatter and the data shown in Figure 26 are comparatively good data with a minimum amount of scatter. Data scatter became severe below approximately 1100°C because of the small amounts of shrinkage, and therefore the majority of the data were obtained between 1100°C and 1165°C.

Prill et al.¹⁴ have shown that errors in interpretation of the sintering mechanism can occur when the shrinkage occurring during the rearrangement process (first stage) is not taken into account. All of the data were plotted on logarithm shrinkage versus logarithm time graphs, as shown in Figure 26, and the first break in the curve was taken as the point at which the rearrangement process was complete. The total shrinkage and elapsed time at this point were subtracted from the shrinkage and time values, and replotted as $\Delta L/L_r$ versus corrected time.

Shrinkage data obtained for samples containing a liquid phase equal to 1.5 wt% are shown in Figures 27 and 28. Figure 29 contains shrinkage data for specimens containing 11.8 wt% liquid phase.

The shrinkage data presented in Figures 26 through 29 were obtained on disks containing SmCo_5 powders with an average particle diameter of 12.6 μm . The particle size was measured by metallographically sectioning the sintered samples and counting the number of grain boundaries intersected by random straight lines of known length. The particle sizes reported are equal to 1.5 times the average distance between the intercepts.¹⁵

Shrinkage data were also obtained on SmCo_5 powders with average particle sizes of 7.4 and 19.6 μm . The 7.4- μm shrinkage data are shown in Figure 30, and the 19.6 μm data are shown in Figures 31 and 32.

The shrinkage was measured over a temperature range between 1032 and 1165°C. A typical shrinkage isotherm obtained at 1123°C is shown in Figure 26. Experiments of this type usually exhibit some experimental scatter and the data shown in Figure 26 are comparatively good data with a minimum amount of scatter. Data scatter became severe below approximately 1100°C because of the small amounts of shrinkage, and therefore the majority of the data were obtained between 1100°C and 1165°C.

Prill et al.¹⁴ have shown that errors in interpretation of the sintering mechanism can occur when the shrinkage occurring during the rearrangement process (first stage) is not taken into account. All of the data were plotted on logarithm shrinkage versus logarithm time graphs, as shown in Figure 26, and the first break in the curve was taken as the point at which the rearrangement process was complete. The total shrinkage and elapsed time at this point were subtracted from the shrinkage and time values, and replotted as $\Delta L/L_r$ versus corrected time.

Shrinkage data obtained for samples containing a liquid phase equal to 1.5 wt% are shown in Figures 27 and 28. Figure 29 contains shrinkage data for specimens containing 11.8 wt% liquid phase.

The shrinkage data presented in Figures 26 through 29 were obtained on disks containing SmCo_5 powders with an average particle diameter of 12.6 μm . The particle size was measured by metallographically sectioning the sintered samples and counting the number of grain boundaries intersected by random straight lines of known length. The particle sizes reported are equal to 1.5 times the average distance between the intercepts.¹⁵

Shrinkage data were also obtained on SmCo_5 powders with average particle sizes of 7.4 and 19.6 μm . The 7.4- μm shrinkage data are shown in Figure 30, and the 19.6 μm data are shown in Figures 31 and 32.

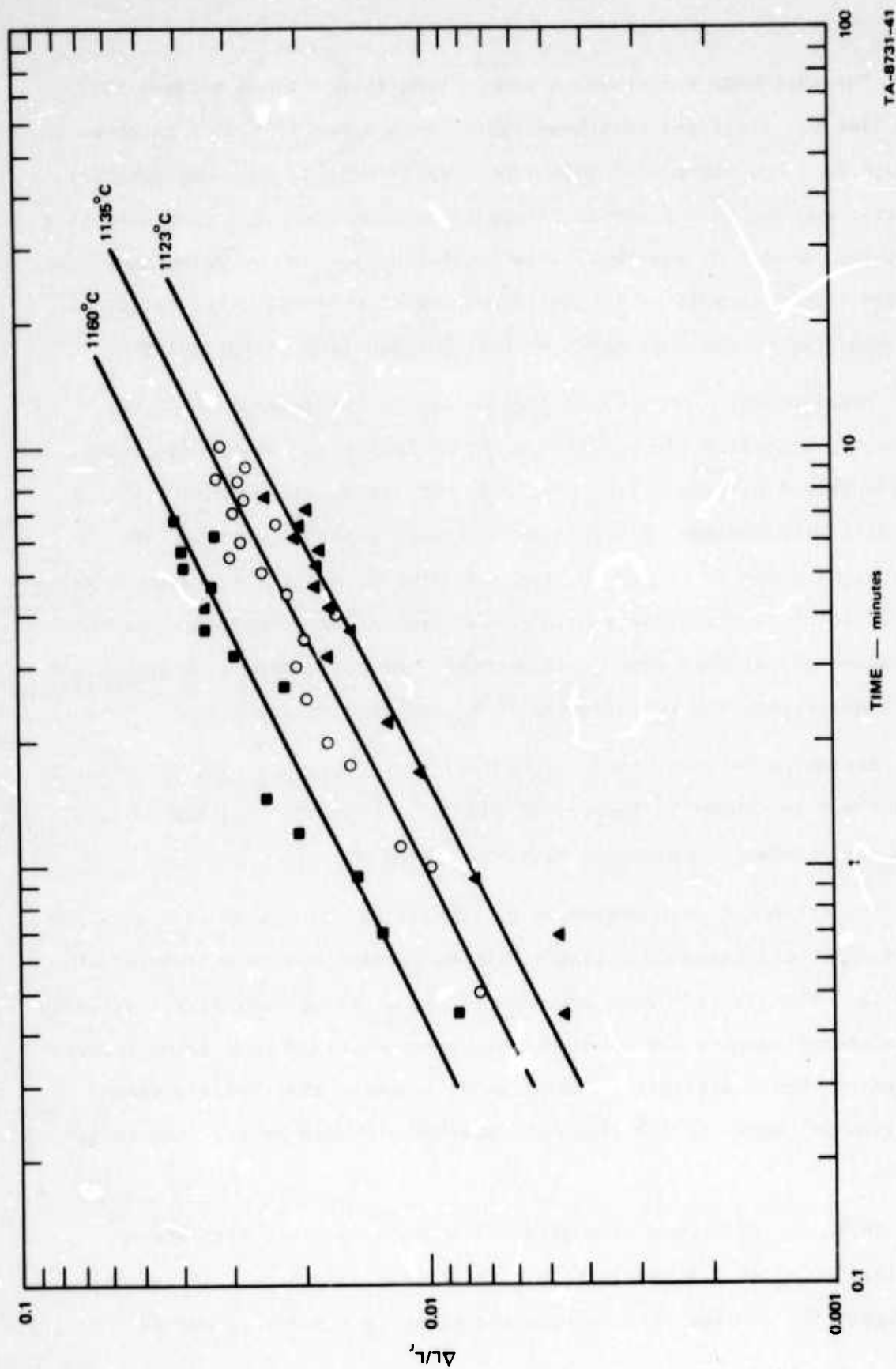
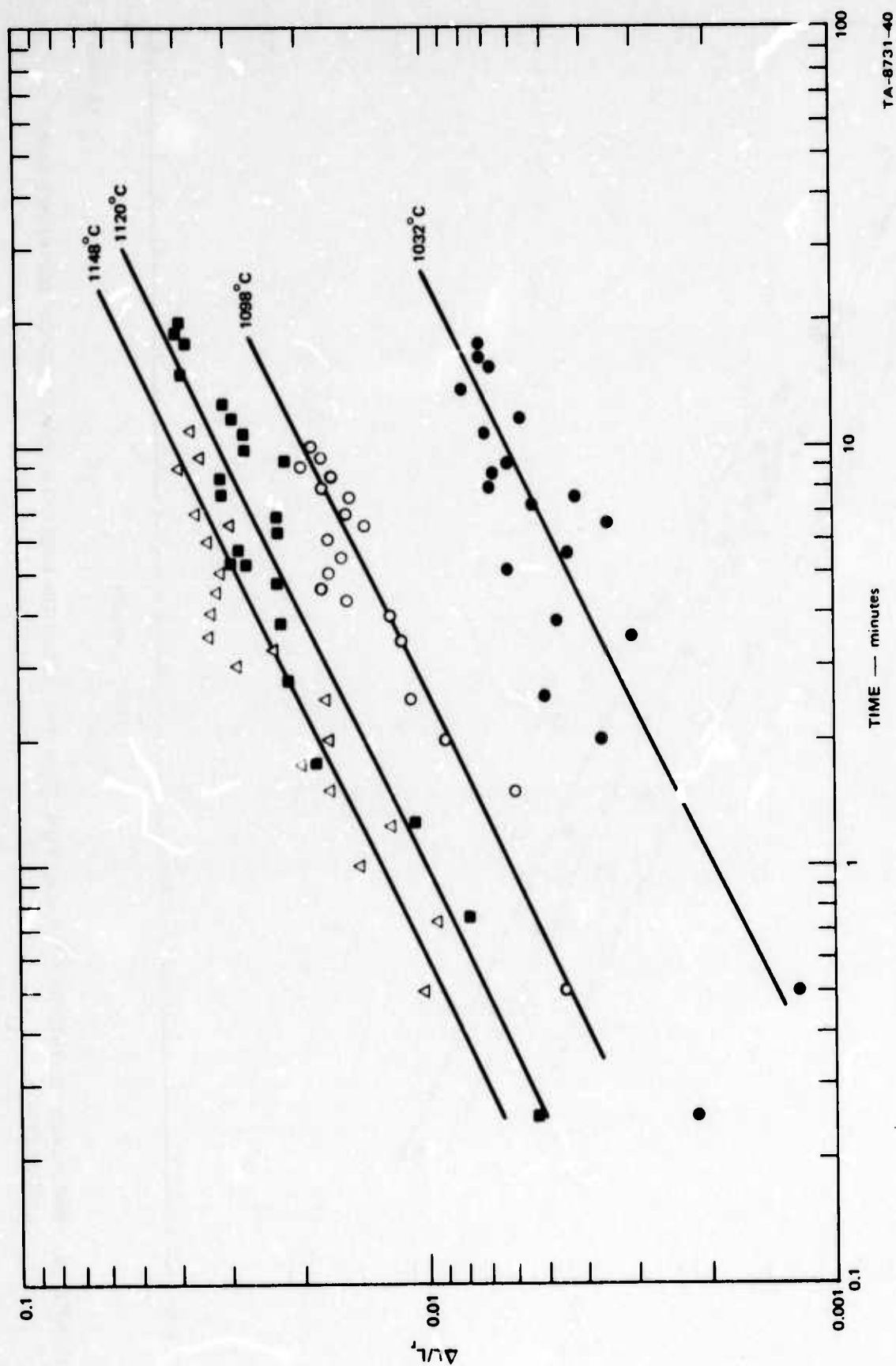


FIGURE 27 CORRECTED ISOTHERMAL TIME DEPENDENCE OF SHRINKAGE OF SmCo_5 COMPACTS AT SEVERAL TEMPERATURES FOR ONLY THE SOLUTION-PRECIPITATION STAGE OF SINTERING USING 1.5 wt% LIQUID PHASE

TA-8731-41



TA-8731-40

FIGURE 28 CORRECTED ISOTHERMAL TIME DEPENDENCE OF SHRINKAGE OF SmCo_5 COMPACTS AT SEVERAL TEMPERATURES FOR ONLY THE SOLUTION-PRECIPITATION STAGE OF SINTERING USING 1.5 wt% LIQUID PHASE

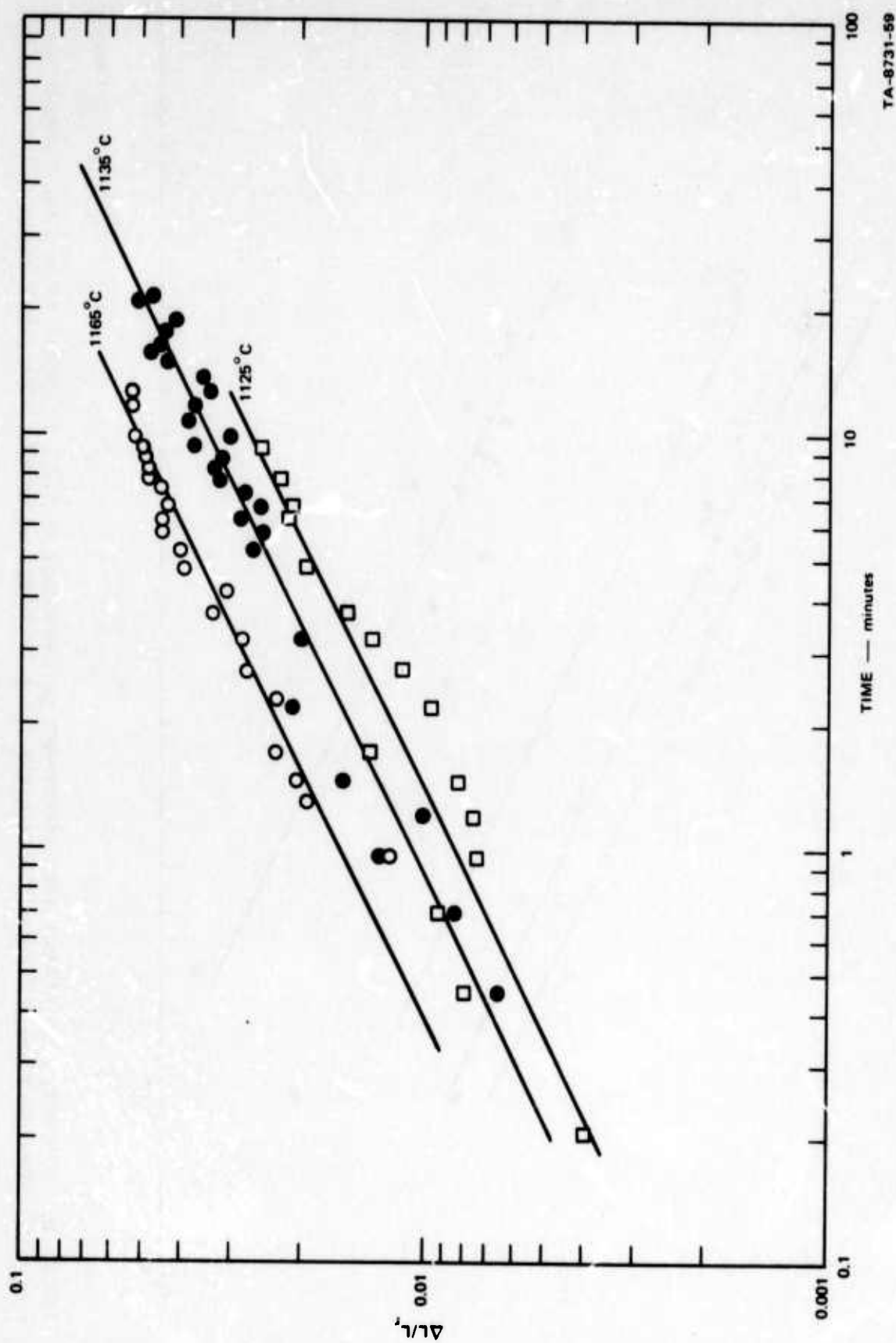
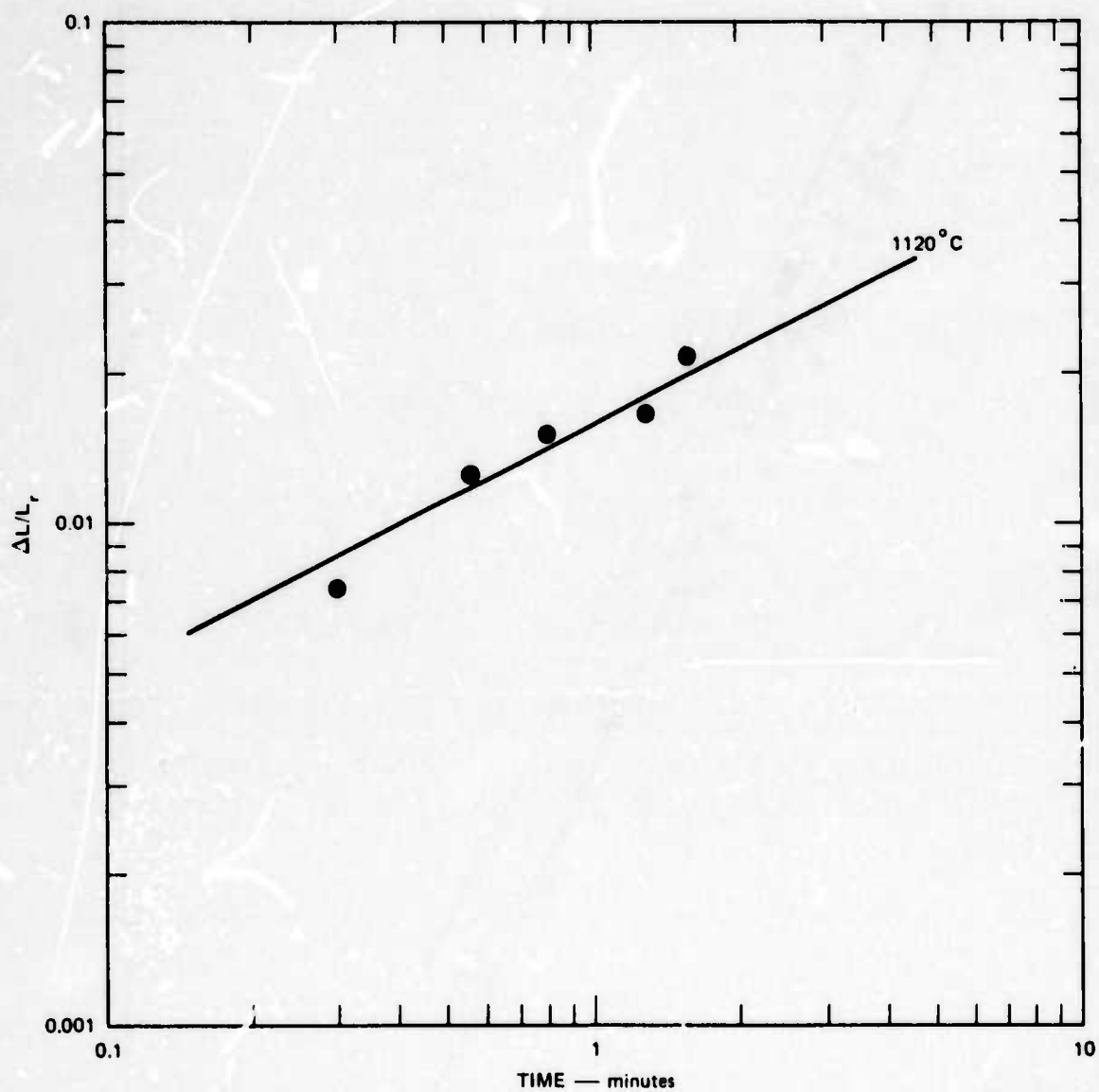


FIGURE 29 SHRINKAGE ISOTHERMS OF SmCo_5 FOR ONLY THE SOLUTION-PRECIPITATION STAGE OF SINTERING USING 11.8 wt% LIQUID PHASE



TA-8731-63

FIGURE 30 SmCo_5 SHRINKAGE DATA OBTAINED AT 1120°C USING 13.8 wt% LIQUID PHASE AND AN AVERAGE PARTICLE SIZE OF $7.4 \mu\text{m}$

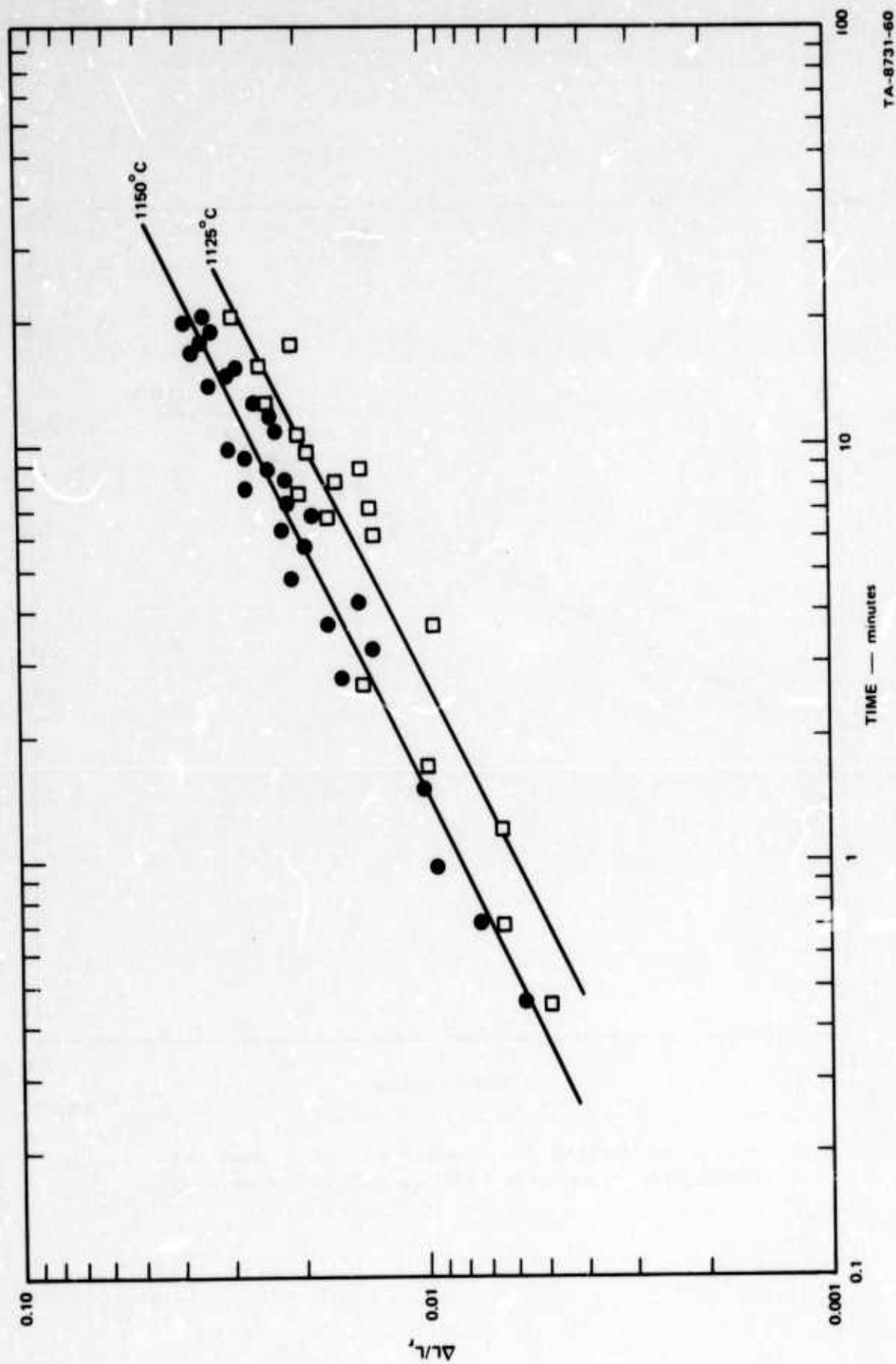


FIGURE 31 SHRINKAGE ISOTHERMS FOR 11.8 wt% LIQUID PHASE AND AN AVERAGE PARTICLE SIZE OF 19.6 μm

TA-8731-60

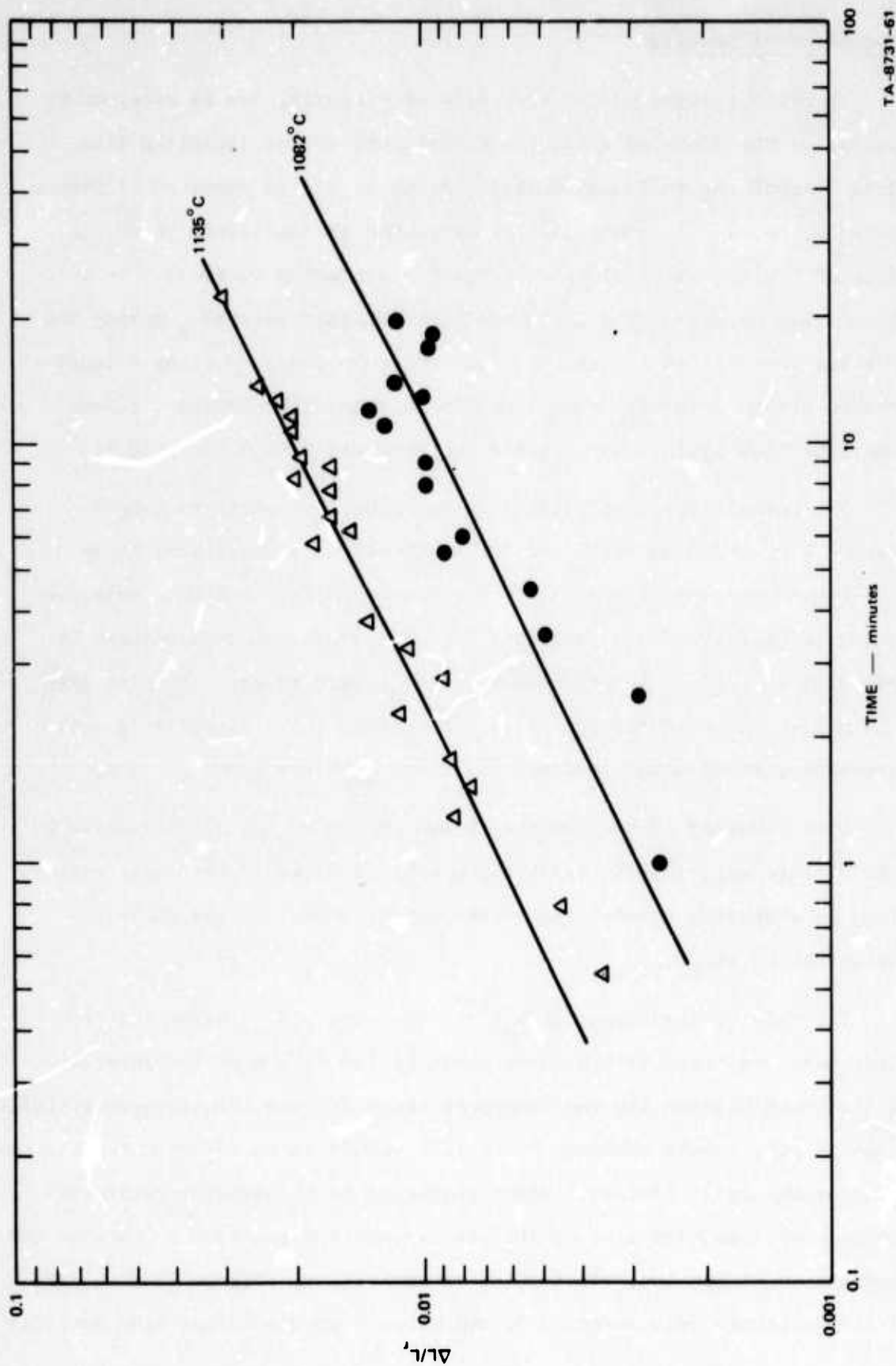


FIGURE 32 SmCo_5 SHRINKAGE ISOTHERMS FOR 11.8 wt% LIQUID PHASE AND AN AVERAGE PARTICLE SIZE OF $19.6 \mu\text{m}$

TA-8731-61

Discussion of Results

An understanding of the mechanism of sintering can be obtained by evaluating the slope of a logarithm shrinkage versus logarithm time plots. According to Equation (1), a slope of 1.3 is expected if the sintering process is controlled by diffusion in the liquid phase. A slope of 1/2 (Equation 2) is expected for sintering controlled by a dissolution process. The shrinkage data obtained for SmCo_5 during the solution-precipitation stage of sintering were analyzed using a least-squares fit to determine the slope of the logarithm shrinkage versus logarithm time plots. The results obtained are listed in Table V.

The correlation coefficient at the higher temperatures ranged between 0.92 and 0.98 while the data obtained at temperatures below 1100°C had correlation coefficients as low as 0.54. The exponents presented in Table V clearly indicate that a dissolution type process is rate limiting rather than diffusion in the liquid phase. The data presented in Figures 27 through 32 were therefore force-fitted to a solid line with a slope equal to 0.5.

Data obtained at temperatures below approximately 1100°C exhibited considerable experimental scatter primarily because of the small differences in shrinkage between the rearrangement stage and the solution-precipitation stage.

The rate of shrinkage, $\Delta L/L_r t^{1/2}$, on a $\log \Delta L/L_r$ versus $\log t$ plot where the slope is 1/2 corresponds to the values of the intercept. If the break between the rearrangement stage and the solution-precipitation stage is incorrectly determined, it will result in an error in the shrinkage rate for the later process. Since sintering is a thermally activated process, an Arrhenius plot of the rate versus $1/T$ provides a check on the correctness of the transition point determination. Figure 33 is a plot of the shrinkage rate versus $1/T$, and since a good straight line data fit

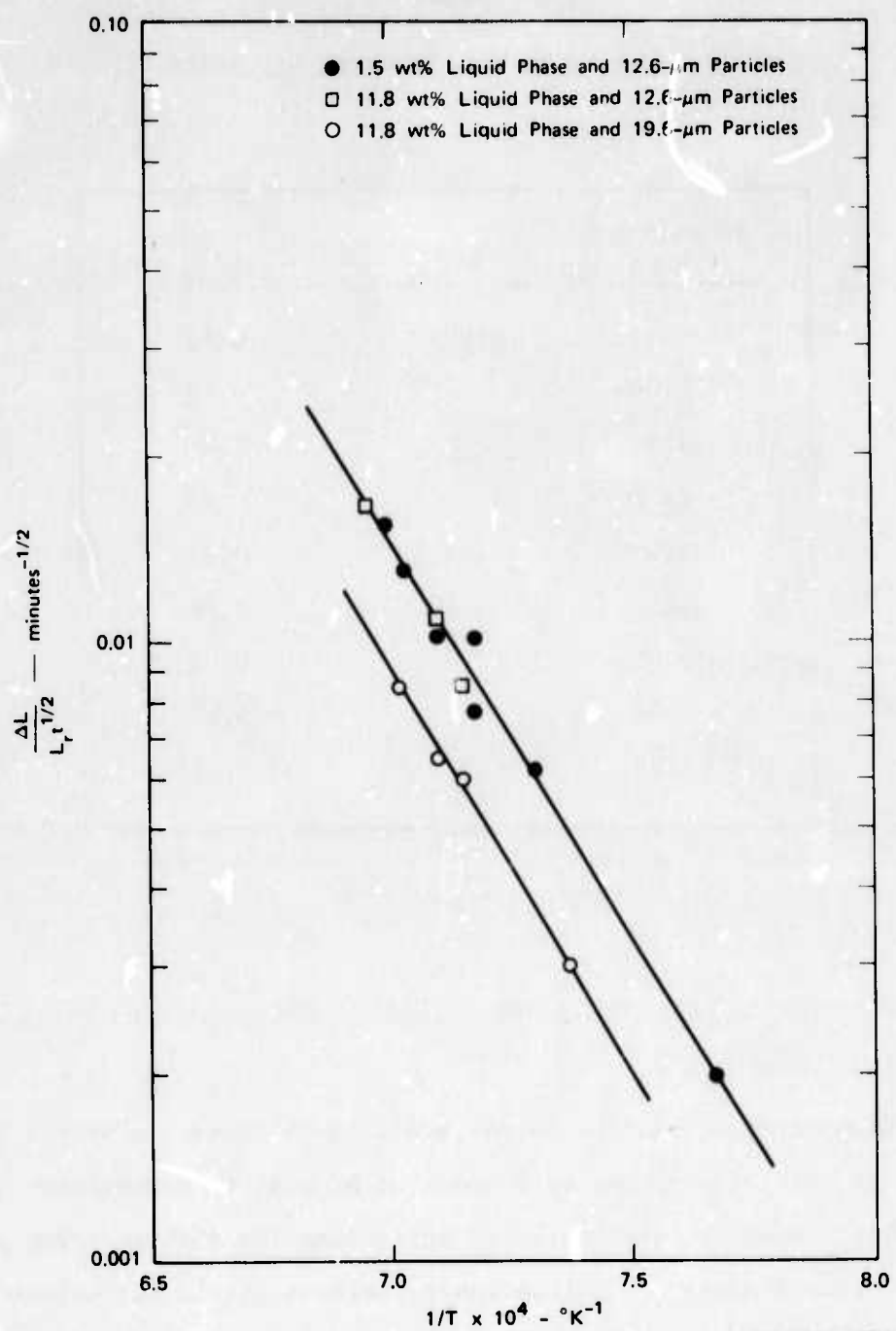


FIGURE 33 ARRHENIUS PLOT OF THE SHRINKAGE RATE VERSUS RECIPROCAL TEMPERATURE

Table V

TYPICAL SHRINKAGE ISOTHERM EXPONENTS

Temperature (°C)	Exponent
1165	0.51
1150	0.52
1135	0.49
1135	0.44
1125	0.41
1123	0.48
1120	0.47
1105	0.51
1082	0.65

was obtained, confidence can be placed in the transition point of determinations.

Quantitative reaction rates cannot be calculated a priori from Equation (2), because the rate constant k' must be determined experimentally. However, the energy of activation for the sintering process may provide a means of distinguishing between liquid diffusion-controlled sintering and sintering controlled by dissolution. The apparent activation energy determined from the slope of the Arrhenius plot, Figure 33, is 57.6 kcal/mole. In Equation (2) the rate constant k' and the solubility X_0 vary exponentially with temperature. The enthalpy associated

with X_0 was determined from data taken from the samarium-cobalt phase diagram and was equal to 4.8 kcal/mole. Thus, the energy of activation for k' is 52.8 kcal/mole. Alternatively, the liquid diffusion-controlled sintering model, Equation (1), contains terms X_0 and D that vary exponentially with temperature. Thus, liquid diffusion-controlled sintering would require a liquid diffusion coefficient D with an activation energy greater than 50 kcal/mole, which is about an order of magnitude greater than the diffusion activation energies normally observed in liquid alloys. This fact strongly indicates that sintering is controlled by the phase-boundary dissolution process during the solution-precipitation stage rather than liquid diffusion.

Another means of distinguishing between different sintering mechanisms is to investigate the rate of sintering as a function of particle size, since the models for sintering exhibit various dependencies on the radius of the sintering particles. Table VI lists the particle size dependence for various sintering models.

Table VI

SINTERING MODEL PARTICLE SIZE DEPENDENCE

<u>Liquid-Phase Sintering</u>	<u>Particle Size Dependence</u>
Dissolution process	r^{-1}
Diffusion in liquid phase	$r^{-4/3}$
<u>Solid-State Sintering</u>	
Volume diffusion	$r^{-3/2}$
Grain boundary diffusion	$r^{-4/3}$

The exponents in Table VI for the solid-state sintering models vary slightly from those quoted with different assumed boundary conditions, but these variations will not confuse the conclusions to be made in this particular study. The rate of sintering of SmCo_5 for the solution-precipitation stage is plotted in Figure 34 versus the grain size of the SmCo_5 particles. These data were obtained at a constant power setting of the vacuum furnace that produced a temperature of $1123^\circ\text{C} \pm 5^\circ\text{C}$. Lines corresponding to the various particle size functions were passed through the smallest grain size datum point. A comparison of the lines in Figure 34 indicates that a phase boundary (solid-liquid) reaction is rate limiting for the initial sintering of SmCo_5 . Figure 33 shows the difference in rate of sintering between 12.6- μm and 19.6- μm particles as a function of temperature.

The rate of sintering can be calculated if reasonable values are assigned to the constants in Equation (2). Let k' equal $\frac{\lambda kT}{h} e^{\Delta S^\ddagger/R} e^{-Q/RT}$ where λ is the jump distance, ΔS^\ddagger is the entropy of activation, Q is the energy of activation and k and h are Boltzmann's and Planck's constants, respectively. Then, assuming the following values: $\lambda = 3\text{\AA}$, $\Delta S^\ddagger = 2.0 \text{ E.U.}$, $Q = 52.8 \text{ kcal/mole}$, $K_1 = 0.5$, $K_2 = 1$, $x_o = 0.42$, $\gamma_{LV} = 300 \text{ erg/cm}^2$, $V_o = 51.7 \text{ cm}^3/\text{mole}$, $T = 1123^\circ\text{C}$, and $r = 12.6 \mu\text{m}$, we obtain a sintering rate equal to $4.85 \times 10^{-1} \text{ min}^{-1/2}$ based on the assumption that every surface site is active. Experimentally we observe a sintering rate equal to $8.0 \times 10^{-3} \text{ min}^{1/2}$. If we assign the difference between these two values to inactive surface sites, we obtain a ratio of active/inactive surface sites of 1/60, which is a reasonable number.

The amount of liquid phase present does not affect the solution-precipitation sintering kinetics, see Figure 33. This behavior is expected from a consideration of the rate-controlling step and the resulting kinetic equations. The amount of liquid phase does, however, influence the total

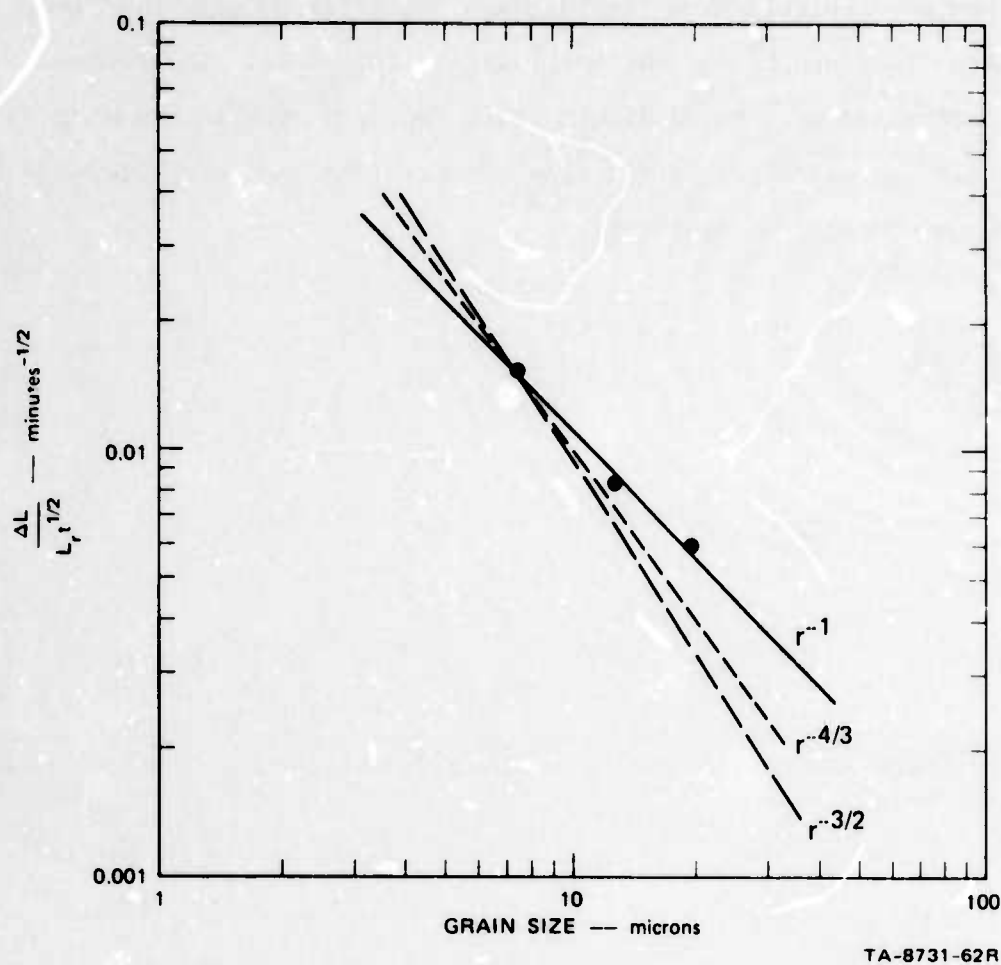


FIGURE 34 PLOT OF THE SINTERING RATE OF SmCo_5 VERSUS THE GRAIN SIZE AT A TEMPERATURE OF 1123°C

amount of shrinkage obtained in the rearrangement stage of a liquid-phase sintering process.

Conclusions

The initial sintering of SmCo_5 in the presence of a 60 wt% Sm additive can be described as a liquid-phase sintering process involving rearrangement followed by a solution-precipitation stage. The latter stage is controlled by a solid/liquid phase boundary reaction leading to dissolution as evidenced by the time, temperature, and particle size dependence on the rate of sintering.

REFERENCES

1. D. K. Das, IEEE Trans. Magnetics 5, 214 (1969)
2. R. E. Cech, J. Appl. Phys. 41, 5247 (1970)
3. M. G. Benz and D. L. Martin, Appl. Phys. Letters 17, 176 (1970)
4. D. L. Martin and M. G. Benz, Cobalt 50, 11 (1971)
5. D. K. Das, IEEE Trans. Magnetics 7, 432 (1971)
6. M. G. Benz and D. L. Martin in A.I.P. Conf. Proc. No. 5, Magnetism and Magnetic Materials - 1971, A.I.P., New York, p. 1082 (1972)
7. J. Tsui and K. Strnat, Appl. Phys. Letters 18, 107 (1971)
8. J. Tsui, K. Strnat and R. Harmer, J. Appl. Phys. 42, 1539 (1971)
9. D. L. Martin and M. G. Benz, IEEE Trans. Magnetics 7, 285 (1971), and 7, 291 (1971)
10. M. G. Benz and D. L. Martin, J. Appl. Phys. 43, 3165 (1972)
11. G. H. Gessinger, E. de Lamotte and K. Bachmann, AIEE Trans. Magnetics 8, (1972)
12. K.H.J. Buschow and A. S. Van der Goot, J. Less Common Metals 14, 323 (1968)
13. W. D. Kingery, J. Appl. Phys. 30, 301 (1959)
14. A. L. Prill, H. W. Hayden, and J. H. Brophy, Trans. AIME 233, 960 (1965)
15. R. L. Fullman, Trans AIME 197, 447 (1965).

Introduction

Benz and Martin studied the mechanism of sintering of rare-earth cobalt alloys¹ and postulated that the sintering kinetics are controlled by the diffusion of samarium atoms in grain boundaries via a samarium atom-cobalt vacancy cluster exchange mechanism. This conclusion was based on an observed one-third time dependence of volume shrinkage calculated from end point densities of samples that initially contained a liquid phase, and on a comparison of the total volume shrinkage or density with the alloy composition. Benz and Martin further noted that a correlation existed between the conditions that produced rapid shrinkage and the conditions that yielded high intrinsic coercivity. This correlation has important implications in the processing of magnet materials. In the present study, the solid phase stage of sintering of SmCo_5 has been investigated under conditions in which kinetic models could be applied to determine the effect of changes in stoichiometry on the kinetics of sintering.

The sintering kinetics of solids have been investigated extensively beginning with Kuczynski² and then followed by Kingery and Berg,³ Coble,⁴ and Johnson and Cutler.⁵ Refinements in the assumptions relating the mathematical models to the physical model have been made primarily by Johnson.⁶ From these studies the general equation for solid state sintering is given as

$$\frac{\Delta L}{L_0} = \left(\frac{K_V \Omega D}{k T r^n} \right)^m t^m \quad (1)$$

where

$\Delta L/L_0$ = the fractional shrinkage

γ = the surface free energy

Ω = the volume transported per atom of the rate-controlling species

D = the self-diffusion coefficient of the rate-controlling species

k = Boltzmann's constant

T = absolute temperature

r = the particle or powder radius

K, n, m = constants that depend on the sintering mechanism.

Table VII lists the values of the constants versus the sintering mechanism.

Table VII
SINTERING CONSTANTS FOR EQUATION (4)

Sintering Mechanism	K	n	m	Reference
Volume diffusion	5.34	3	0.49	6
	$20/\sqrt{2}$	3	0.40	3
	2	3	0.50	4
Grain boundary diffusion	2.14b	4	0.33	6
	3b	4	0.33	4

The symbol b in Table VII is the grain boundary width. The constant m is usually determined by plotting the logarithm of fractional shrinkage versus the logarithm of time, and a sintering mechanism is deduced based on the value of m . This method of determining the sintering mechanism

is subject to error principally because of the assumption that a single sintering mechanism is operative. Particle shape and size distribution can also lead to erroneous conclusions.⁶

Time and length corrections must be applied, because m varies with small errors in time and shrinkage. These errors result from the inability to heat the sample instantaneously to the sintering temperature. Lay and Carter⁷ have outlined a relatively easy method of correcting the time and length that involves calculating L_0 from thermal expansion data and extrapolating a length versus time plot to intersect the calculated L_0 value, thus determining the effective initial time. Johnson⁸ later pointed out that the method of Lay and Carter is strictly valid only if an array of identically sized spheres are used in the study and if it is known that all of the mass transport is due to a single mechanism.

The effect of stoichiometry on the sintering kinetics of SmCo_5 was investigated by measuring the shrinkage kinetics as functions of time and temperature and by varying the samarium content from 29.3 wt% to 34.8 wt%. These samarium concentrations at the sintering temperature employed extend beyond the limits of the SmCo_5 single phase field.⁹⁻¹¹

Experimental Procedure

Samarium-cobalt alloy powders were made for this study by arc melting the elements. Slight changes in the alloy compositions were obtained by adjusting the samarium/cobalt ratio used in the arc melting. The alloys were annealed in an oxygen-gettered argon atmosphere at 1110°C for four hours, and were then individually ground in an alumina ball mill for three hours using sodium-gettered hexane as the milling fluid. The final alloy compositions were determined from ethylenediaminetetraacetic acid titration data, and the compositions were adjusted for loss of samarium due to the formation of Sm_2O_3 and for incorporation of oxygen in solid solution, which was assumed to be equal to 0.35 wt%. The oxygen content of the alloys

used in this study was determined by both neutron activation analysis and by vacuum fusion analysis. These methods of analysis for oxygen in SmCo_5 give conflicting results, with the vacuum fusion method always exhibiting the higher value.

The neutron activation analyses were consistent with x-ray diffraction studies and metallographic examination, while the vacuum fusion analysis presented discrepancies. The neutron activation analyses were therefore selected as being more representative of the actual oxygen content. Higher oxygen contents determined by vacuum fusion analysis could be due to oxidation of the porous sintered compacts during the analytical procedures since samples are typically heated during the analysis to 1950°C in a vacuum of 10^{-5} torr.

Disk-shaped specimens, 1.0 inch in diameter by 0.13 inch thick, were fabricated by die pressing at 30,000 psi in the absence of a magnetic field. The specimens were placed on a molybdenum support in a furnace employing a graphite resistance heater surrounded by oxygen-gettered argon. The change in sample diameter was recorded by time-lapse photography as functions of time and temperature, and the data were read from the films by means of a Telereadex film analyzer.

Sample length corrections were made following the method of Lay and Carter⁷ using the thermal expansion data presented in Figure 35. These data were obtained by using a commercial dilatometer modified so that a static argon atmosphere could be used to surround the sample to prevent oxidation.

Heating the sintering samples from room temperature to the sintering temperature required approximately 90 seconds. Shrinkage below approximately 1100°C was almost negligible, and the time required to reach 1165°C from 1100°C was approximately 5 seconds. Calculated L_o values (initial

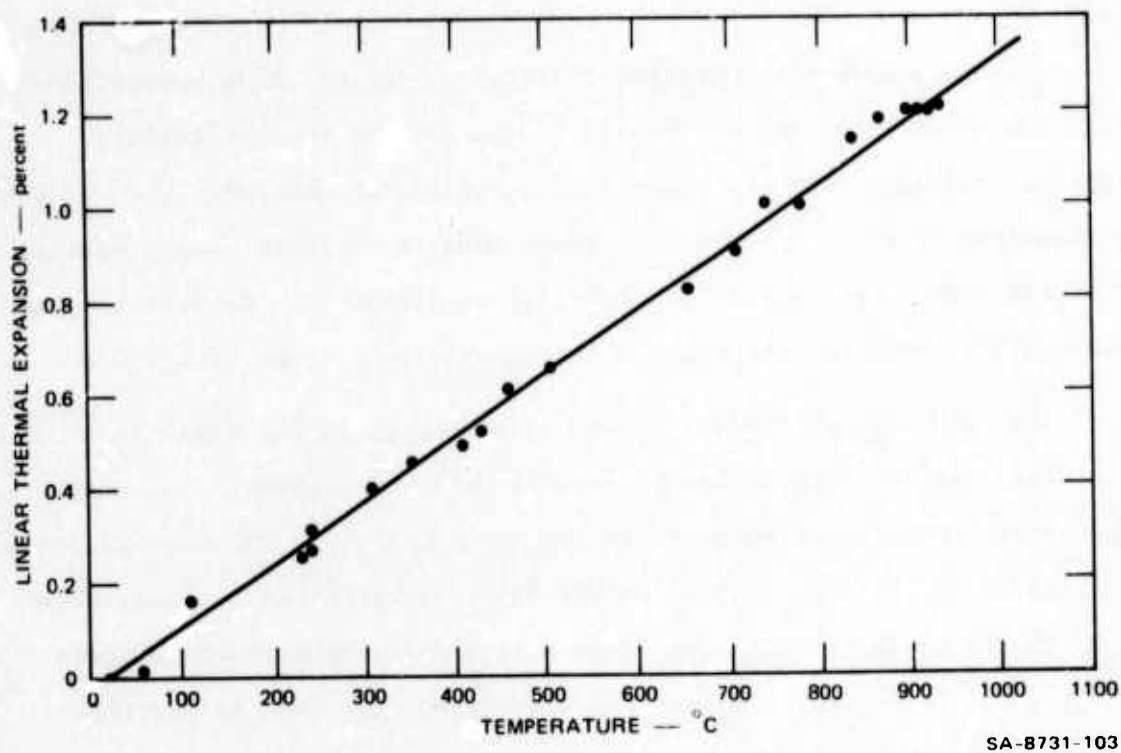


FIGURE 35 LINEAR THERMAL EXPANSION OF POLYCRYSTALLINE RANDOMLY ORIENTED SmCo_5

sample diameter) corresponded exactly with the experimentally measured L_0 values at 1100°C . At 1120°C a small correction in L_0 was required and these corrections increased in magnitude as the sintering temperature was raised to 1165°C , indicating that shrinkage was occurring as the sample was heated from 1100 to 1165°C . The corrections ranged from 0.0% at 1100°C to less than 2.0% at 1165°C .

Results

Shrinkage data were obtained for four different alloy comparisons with one composition being repeated to demonstrate reproducibility. Typical shrinkage data are shown in Figures 36, 37, and 38. The value of m (Equation 1) as determined by a least-squares analysis ranged between 0.24 and 0.37 . The correlation coefficient except for one isotherm was above 0.93 . Thus the shrinkage data approximate a slope of $m = 0.33$.

The time exponent (0.33) of the shrinkage isotherms suggests sintering kinetics controlled by grain boundary diffusion, if a single transport mechanism is responsible for the sintering. The data presented in Figures 36, 37, and 38 were subsequently force-fitted to lines drawn with slopes equal to 0.33 . The data near 1100°C exhibit considerable scatter due to the small amounts of shrinkage. The rate of shrinkage can be calculated from the intercept values for each isotherm, and the rate of shrinkage is shown plotted versus reciprocal temperature in Figure 38.

From the data in Figure 39, an apparent activation energy of 285 kcal/mole for the sintering process was calculated. This extremely high activation energy is unlikely for a grain boundary diffusion process and suggests that more than a single transport mechanism is involved in the solid state sintering of SmCo_5 .

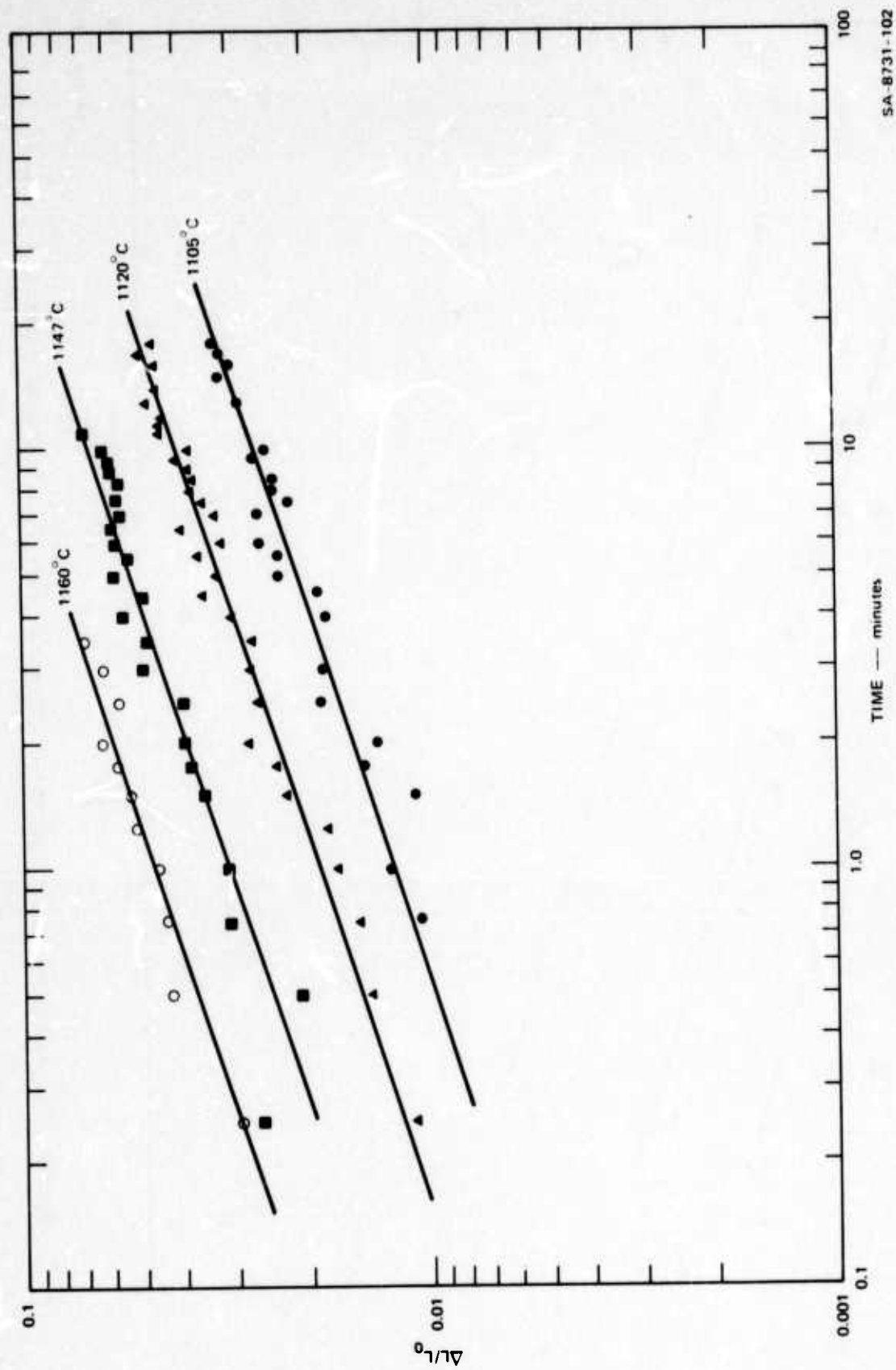


FIGURE 36 SAMARIUM-COBALT SHRINKAGE ISOTHERMS FOR AN ALLOY CONTAINING 29.3 wt% Sm

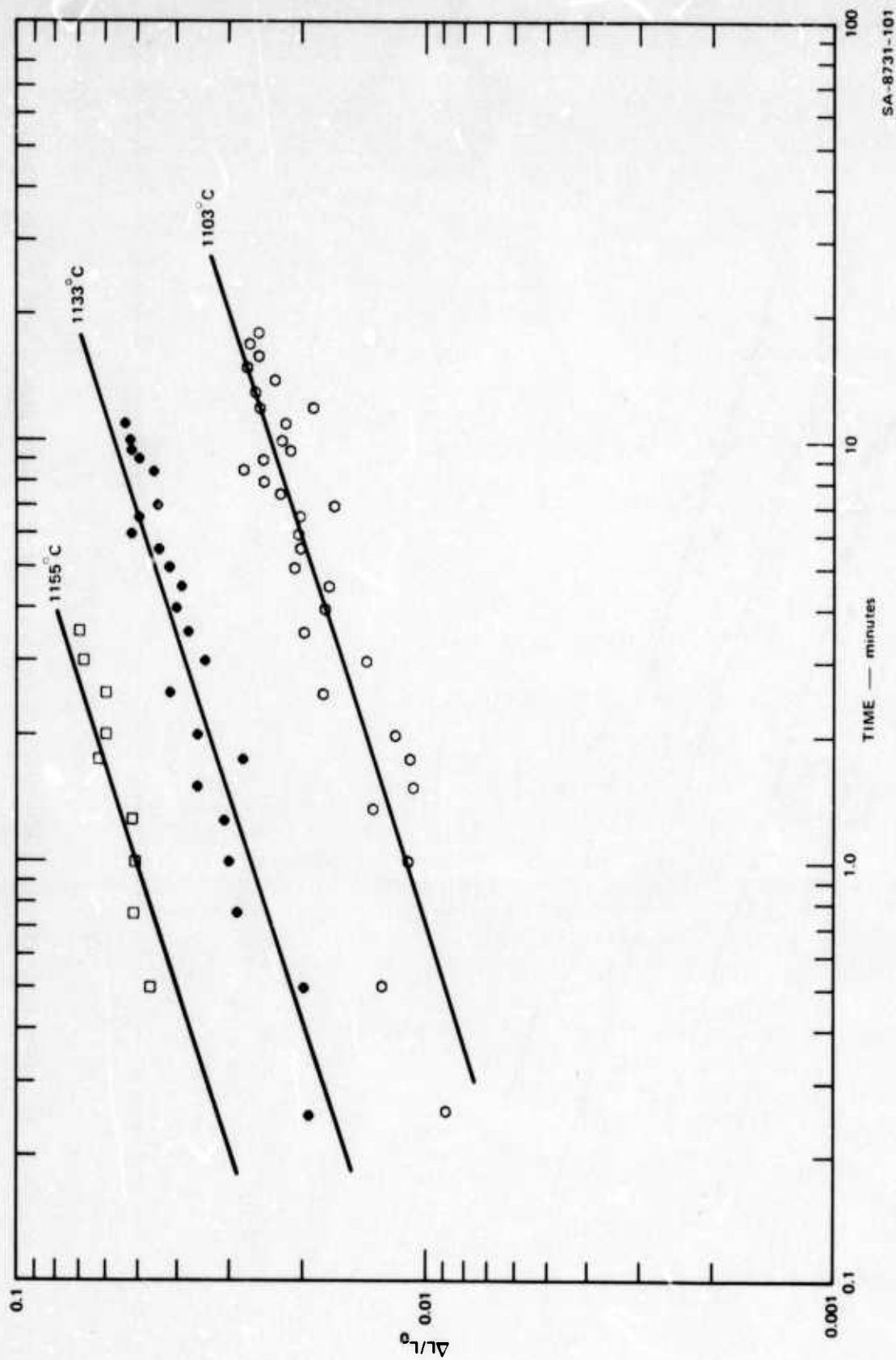


FIGURE 37 SAMARIUM-COBALT SHRINKAGE ISOTHERMS FOR AN ALLOY CONTAINING 32.9 wt% Sm

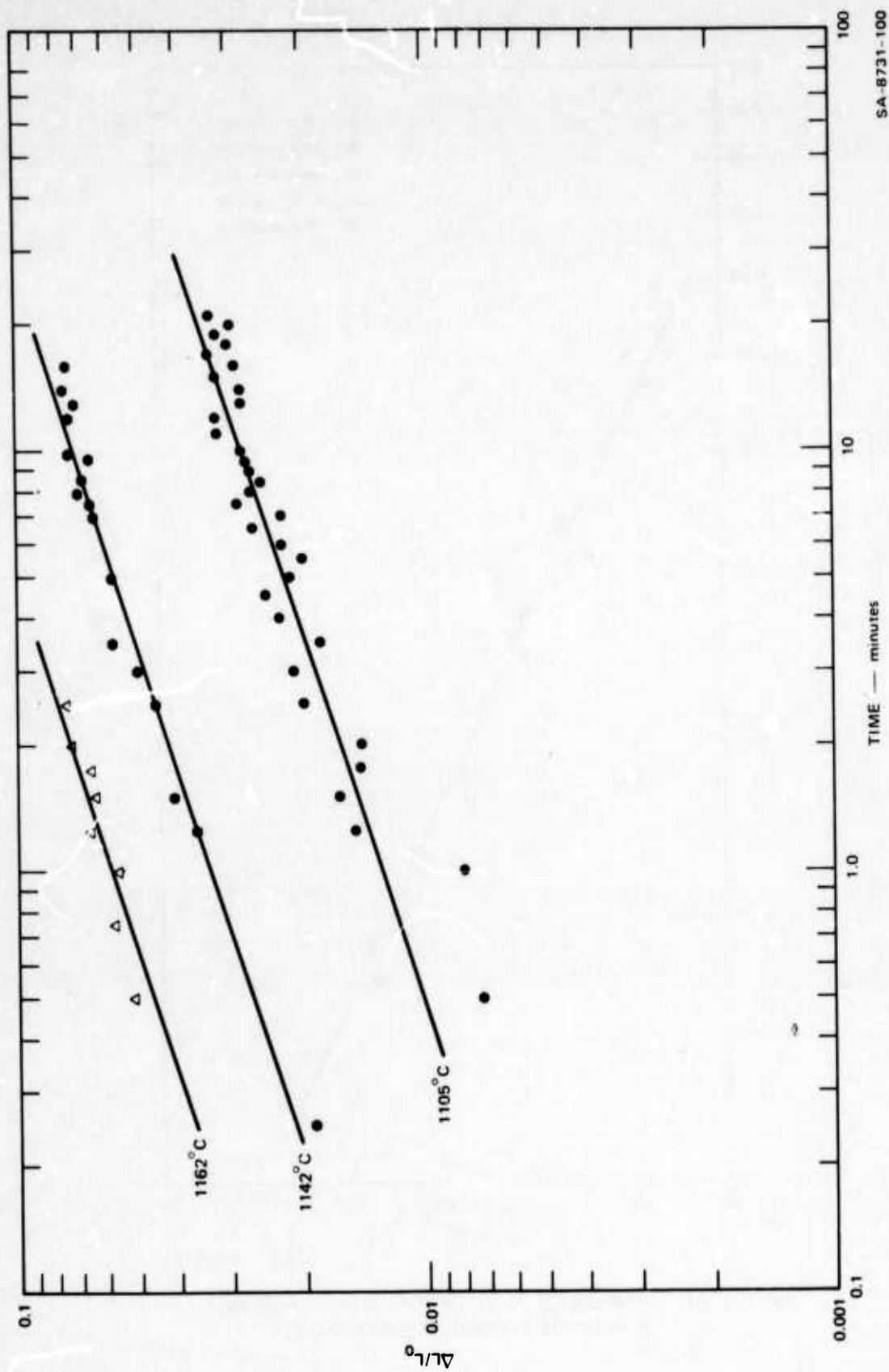
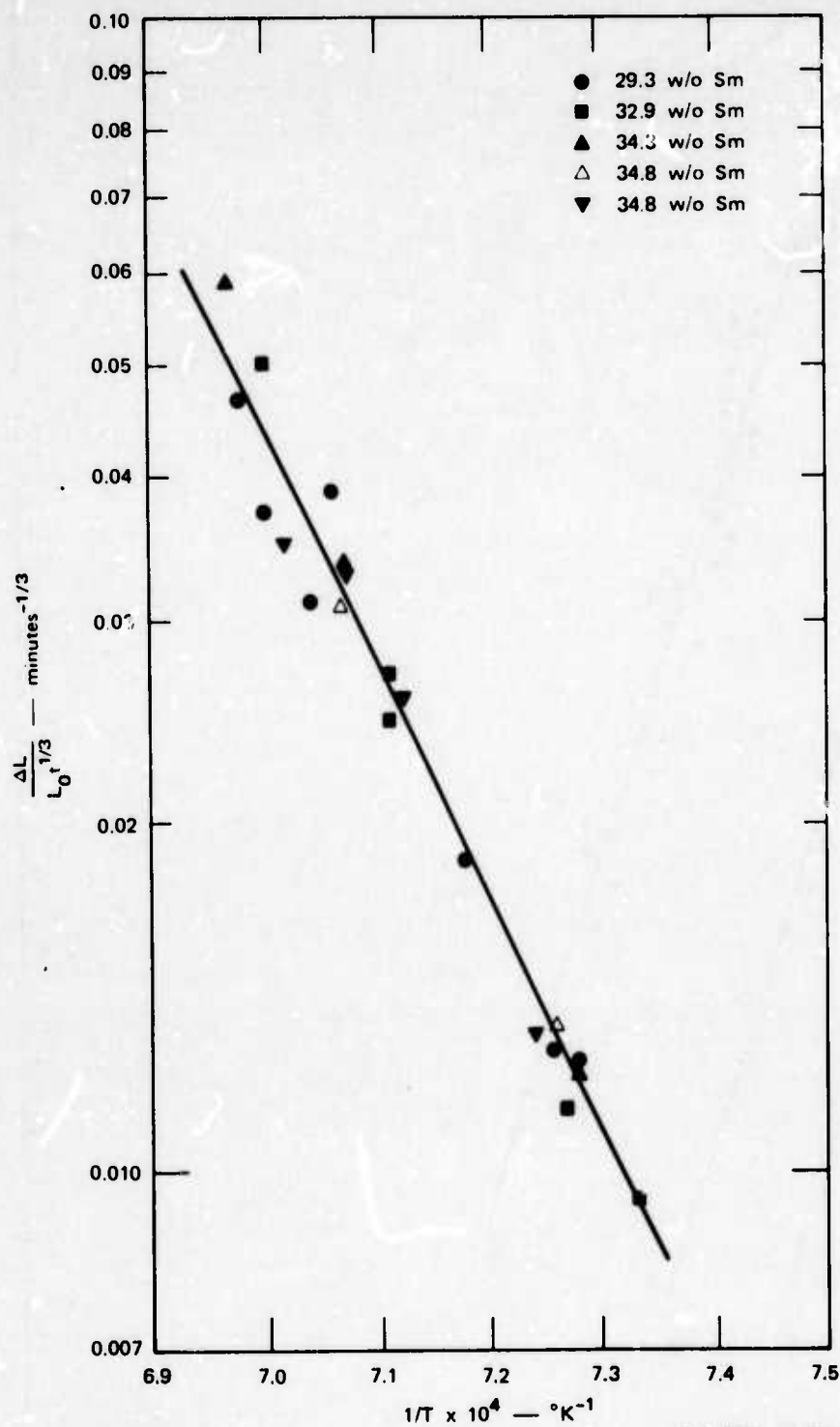


FIGURE 38 SAMARIUM-COBALT SHRINKAGE ISOTHERMS FOR ALLOYS CONTAINING 34.3 AND 34.8 wt% Sm



SA-8731-104R1

FIGURE 39 ARRHENIUS PLOT OF THE SHRINKAGE RATE
VERSUS RECIPROCAL TEMPERATURE

Discussion

The fact that shrinkage occurs indicates that the sintering of SmCo_5 involves transport of material from the grain boundaries to the pore surface by grain boundary transport or by diffusion through the SmCo_5 lattice. A plastic deformation mechanism cannot be completely eliminated especially in the very initial stages of sintering. However, evidence for the predominance of grain boundary transport of samarium in SmCo_5 over lattice diffusion at 800°C can be obtained from annealing experiments using cast alloys.¹²

The oxygen solubility at 1125°C is approximately equal to 0.35 wt%. Quenching and subsequent annealing of the samples at 800°C causes exsolution of the oxygen with the formation of Sm_2O_3 . Oxide particles form at grain boundaries and grow in size by coalescence. The samarium is transported via the grain boundaries to the oxide particles as evidenced by a loss of samarium at the grain boundaries to form $\text{Sm}_2\text{Co}_{17}$.

Size considerations would predict that samarium should diffuse more slowly than cobalt, and therefore it is reasonable to assume from the annealing experiments that the shrinkage observed during the sintering of SmCo_5 is controlled by the diffusion of samarium atoms along grain boundaries, in accordance with the shrinkage-time exponent observed in Figures 36 through 38.

The possibility of surface-diffusion-controlled sintering occurring simultaneously with grain boundary transport was investigated in an attempt to explain the high activation energy obtained from the shrinkage data plotted in Fig. 39. Sintering experiments at 1000°C exhibited considerable neck growth as shown in Fig. 40 without any detectable shrinkage for periods of time up to one hour. Since neck growth occurs without any accompanying shrinkage at 1000°C , we are forced to conclude that transport of material occurs from the surfaces of particles to the neck regions by

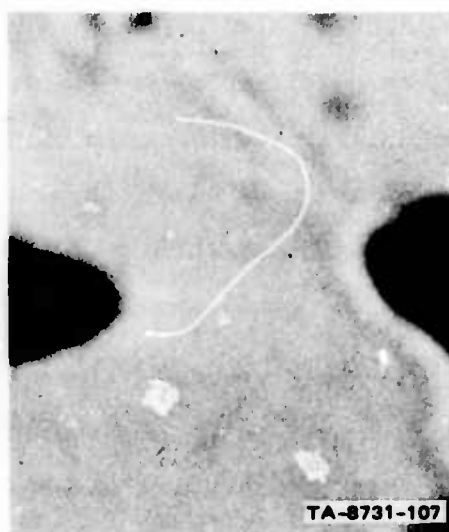


FIGURE 40 PHOTOGRAPH OF NECK REGION OF
SmCo₅ PARTICLES SINTERED AT 1000°C

either a surface diffusion mechanism or by an evaporation-condensation mechanism. The most likely of these is surface diffusion because of the low vapor pressure of cobalt. Either of these mechanisms will cause an increase in the grain boundary diffusion path length and an increase in the neck radius, thereby lowering the chemical potential gradient during the shrinkage process. This will retard the relative amount of shrinkage by grain boundary transport, and it will increase the apparent activation energy until a temperature is reached at which the amount of atomic transport by surface diffusion is negligible with respect to the amount of atomic transport by grain boundary diffusion.¹³

Good spherical particles of SmCo_5 with controlled compositions could not be obtained due to samarium-losses and oxidation during the spheroidization process. This precluded obtaining meaningful data on neck size versus shrinkage, which would have allowed a determination of the relative amounts of surface diffusion versus grain boundary diffusion. Therefore it is impossible to calculate activation energies for the individual sintering mechanisms. These same reasons also prevent a correlation of the preexponential factors and therefore prevent an unequivocal identification of the sintering mechanisms.

The samarium content has been varied entirely across the SmCo_5 phase field, and since we do not observe any difference in the rate of shrinkage as the samarium/cobalt ratio is varied, we are forced to conclude that deviations in stoichiometry in this system do not alter the sintering kinetics.

Conclusions

From the data obtained in this study we can conclude that the densification kinetics of SmCo_5 are unaffected by changes in stoichiometry and therefore any correlation of stoichiometry with magnetic properties must be made on the basis of factors other than densification kinetics.

Solid state sintering of SmCo_5 is controlled by more than one transport mechanism, and the most likely mechanisms are grain boundary transport, which accounts for the observed shrinkage, and surface diffusion, which results in interparticle neck formation without densification.

REFERENCES

1. M. G. Benz and D. L. Martin, J. Appl. Phys. 43, 3165 (1972)
2. G. C. Kuczynski, Trans. AIME 185, 169 (1949)
3. W. D. Kingery and M. Berg, J. Appl. Phys. 26, 1205 (1955)
4. R. L. Coble, J. Amer. Ceram. Soc. 41, 55 (1958)
5. D. L. Johnson and I. B. Cutler, J. Amer. Ceram. Soc. 46, 541 (1963)
6. D. L. Johnson, J. Appl. Phys. 40, 192 (1969)
7. K. W. Lay and R. E. Carter, J. Amer. Ceram. Soc. 52, 189 (1969)
8. D. L. Johnson, J. Amer. Ceram. Soc. 52, 562 (1969)
9. K.H.J. Buschow and A. S. Van Der Goot, J. Less-Common Metals 14, 323 (1968)
10. K.H.J. Buschow and F.J.A. Den Broeder, J. Less-Common Metals 33, (1973)
11. K. J. Williams, R. W. Bartlett, and P. J. Jorgensen, to be published.
12. R. W. Bartlett and P. J. Jorgensen, to be published, J. Less-Common Metals
13. W. S. Young and I. B. Cutler, J. Amer. Ceram. Soc. 53, 659 (1970).

VI MATERIALS PROCESSING OF $\text{Sm}_2\text{Co}_{17}$ ALLOYS FOR PERMANENT MAGNETS

Introduction

$\text{Sm}_2\text{Co}_{17}$ has a theoretical BH product equal to 36×10^6 gauss-oersteds, and $\text{Sm}_2\text{Co}_{0.6}\text{Fe}_{0.4}\text{Co}_{17}$ has a theoretical maximum energy product equal to 6×10^6 gauss-oersteds. Practical permanent magnets using these compounds have not been made, because we have not been able to achieve intrinsic coercivities above 2000 Oe. Therefore, a study of the powder-processing parameters of these compounds was begun, with the objective of increasing the intrinsic coercive force, H_M^C . Knowledge obtained in processing of SmCo_5 magnets was used as a guide in this study; therefore hyperstoichiometric, stoichiometric and substoichiometric compounds were formulated for $\text{Sm}_2\text{Co}_{17}$, $\text{Sm}_2(\text{Co}_{0.9}\text{Fe}_{0.1})_{17}$, and $\text{Sm}_2(\text{Co}_{0.6}\text{Fe}_{0.4})_{17}$.

Experimental Procedure

Alloy powders were made for this study by arc-melting the elements. Non-uniformities could be observed in arc melted buttons; therefore the buttons were crushed and remelted. The arc melted alloys were then annealed at 1100°C in an argon atmosphere for four hours, and were individually ground in an iron ball mill for four hours using sodium-gettered hexane as the milling fluid. The average particle size of these powders after milling ranged between 2.5 and $3.5 \mu\text{m}$, as determined by a corrected Fisher analysis.

Samples that would allow the intrinsic coercive force of the as ground powders to be measured were made by blending the individual powders in epoxy and then superimposing a 24,000 gauss magnetic while the epoxy cured.

Sintered permanent magnet samples were fabricated by partially filling 1/2-in. diameter surgical tubing (closed with rubber stoppers) with the powder. The sample was then aligned in a magnetic coil (10,000 gauss) while being subjected to mechanical vibrations. The rubber container was evacuated by means of a hypodermic needle while in the magnetic field, and then the sample was hydrostatically pressed at 50,000 psi.

Densification of the samples was accomplished by sintering in an argon atmosphere at approximately 1200°C for one hour.

The intrinsic coercive force was measured by using a P.A.R. vibrating magnetometer coupled to a 100,000 gauss superconducting magnet.

It is possible that second phase material precipitated within the $\text{Sm}_2\text{Co}_{17}$ grains could act as nuclei for new magnetic domains, and thereby lower the intrinsic coercive force. Therefore, annealing heat treatments were conducted at 900°C for varying lengths of time in an attempt to equilibrate any second phase material at the $\text{Sm}_2\text{Co}_{17}$ grain boundaries.

Results and Discussion

The intrinsic coercivities of the as ground powder samples were independent of stoichiometry with values ranging between 2000 Oe and 3000 Oe. Table VIII lists the measured intrinsic coercivities versus sample composition and temperature.

The powders listed in Table VIII were sintered at 1200°C for times ranging between one hour and six hours. The densities obtained for the $\text{Sm}_2\text{Co}_{17}$ compounds ranged between 8.0 and 8.28 gm/cm³. The substitution of iron for cobalt reduced the final densities achieved in the sintering heat treatment; for example, the densities for the $\text{Sm}_2(\text{Co}_{60}\text{Fe}_{40})_{17}$ samples ranged from 5.53-7.21 gm/cm³, and increasing the sintering time from two to six hours increased the final density less than 1%.

Table VIII

INTRINSIC COERCIVE FORCE OF AS GROUND POWDERS

Compound	Composition	Intrinsic Coercive Force (Oe)	Measurement Temperature ($^{\circ}\text{K}$)
$\text{Sm}_2\text{Co}_{17}$	$\text{Sm}_2\text{Co}_{16.2}$	2500	250
	$\text{Sm}_2\text{Co}_{16.8}$	2500	250
	$\text{Sm}_2\text{Co}_{18.0}$	2500	250
$\text{Sm}_2(\text{Co}_{90}, \text{Fe}_{10})_{17}$	$\text{Sm}_2(\text{Co}_{90}, \text{Fe}_{10})_{16.2}$	2500	272
	$\text{Sm}_2(\text{Co}_{90}, \text{Fe}_{10})_{17.1}$	2700	249
	$\text{Sm}_2(\text{Co}_{90}, \text{Fe}_{10})_{18.0}$	3000	250
$\text{Sm}_2(\text{Co}_{59}, \text{Fe}_{41})_{17}$	$\text{Sm}_2(\text{Co}_{59}, \text{Fe}_{41})_{16.4}$	2000	247
	$\text{Sm}_2(\text{Co}_{59}, \text{Fe}_{41})_{17.3}$	2000	253
	$\text{Sm}_2(\text{Co}_{59}, \text{Fe}_{41})_{18.4}$	2300	260

The intrinsic coercivities measured on the sintered samples are presented in Table IX. These sintered samples did not show an increase in the intrinsic coercive force after sintering; therefore annealing heat treatments were conducted at 900°C for times up to 48 hours. The annealing heat treatments were designed to dissolve second phases occurring within the primary $\text{Sm}_2\text{Co}_{17}$ grains and reprecipitate the second phase material at grain boundaries where the second phase particles could grow in size. Annealing heat treatments at 900°C for 48 hours did not completely remove the second phase material from within the grains, and the annealing did not affect the coercivity of the samples. Table X lists the coercivities of the annealed samples. If it is assumed that equilibrium was achieved in the annealing samples, then the sub-solidus region of the Sm-Co phase diagram pertaining to the $\text{Sm}_2\text{Co}_{17}$ phase is incorrect.* This result indicated the necessity of studying the subsolidus phase equilibria for the $\text{Sm}_2\text{Co}_{17}$ compound, and the results obtained are presented in Section VII of this report.

Conclusions

$\text{Sm}_2\text{Co}_{17}$ powders having an average diameter of two to three microns can be sintered to a closed porosity stage by heating in an argon atmosphere at 1200°C.

The intrinsic coercive force of as ground powders, sintered magnets, and annealed magnet samples did not exceed 3000 Oe.

Metallographic examination of the annealed samples indicated that the sub-solidus region of the Sm-Co phase diagram pertaining to the $\text{Sm}_2\text{Co}_{17}$ phase is incorrect; therefore the homogeneity range of the $\text{Sm}_2\text{Co}_{17}$ phase field was studied in order to provide pertinent data for further research on the coercivity of $\text{Sm}_2\text{Co}_{17}$ magnets.

* K.H.J. Buschow and A. S. Van Der Goot, J. Less-Common Metals, 14, 323 (1968).

Table IX

INTRINSIC COERCIVE FORCE OF SINTERED $\text{Sm}_2\text{Co}_{17}$ MAGNETS

Compound	Composition	Intrinsic Coercive Force (Oe)	Measurement Temperature ($^{\circ}\text{K}$)
$\text{Sm}_2\text{Co}_{17}$	$\text{Sm}_2\text{Co}_{16.2}$	1750	250
	$\text{Sm}_2\text{Co}_{16.8}$	1830	258
	$\text{Sm}_2\text{Co}_{18}$	1800	250
$\text{Sm}_2(\text{Co}_{90}, \text{Fe}_{10})_{17}$	$\text{Sm}_2(\text{Co}_{90}, \text{Fe}_{10})_{16.2}$	200	241
	$\text{Sm}_2(\text{Co}_{90}, \text{Fe}_{10})_{17.1}$	1830	234
	$\text{Sm}_2(\text{Co}_{90}, \text{Fe}_{10})_{18.0}$	1900	250
$\text{Sm}_2(\text{Co}_{60}, \text{Fe}_{40})_{17}$	$\text{Sm}_2(\text{Co}_{59}, \text{Fe}_{41})_{16.4}$	1800	248
	$\text{Sm}_2(\text{Co}_{59}, \text{Fe}_{41})_{17.3}$	1750	247
	$\text{Sm}_2(\text{Co}_{54}, \text{Fe}_{41})_{18.4}$	1830	238

Table X

INTRINSIC COERCIVE FORCE OF ANNEALED $\text{Sm}_2\text{Co}_{17}$ MAGNETS

Compound	Composition	Intrinsic Coercive Force ($\frac{H}{M \cdot C}$)	Measurement Temp. ($^{\circ}\text{K}$)	Annealing Time at 900°C (hours)
$\text{Sm}_2\text{Co}_{17}$	$\text{Sm}_2\text{Co}_{16.2}$	1700	236	4
	$\text{Sm}_2\text{Co}_{16.8}$	2100	228	4
	$\text{Sm}_2\text{Co}_{18}$	1700	222	4
$\text{Sm}_2(\text{Co}_{90}, \text{Fe}_{10})_{17}$	$\text{Sm}_2(\text{Co}_{90}, \text{Fe}_{10})_{16.2}$	1800	256	48
	$\text{Sm}_2(\text{Co}_{90}, \text{Fe}_{10})_{18.0}$	1800	241	48
	$\text{Sm}_2(\text{Co}_{90}, \text{Fe}_{10})_{17.1}$	1800	251	48
$\text{Sm}_2(\text{Co}_{60}, \text{Fe}_{40})_{17}$	$\text{Sm}_2(\text{Co}_{59}, \text{Fe}_{41})_{16.4}$	2100	252	48
	$\text{Sm}_2(\text{Co}_{59}, \text{Fe}_{41})_{17.3}$	1830	234	48
	$\text{Sm}_2(\text{Co}_{59}, \text{Fe}_{41})_{18.4}$	1950	269	48

VII CONTRIBUTION TO THE SAMARIUM COBALT PHASE DIAGRAM

The system samarium-cobalt was studied over the entire concentration range by Buschow and Van Der Goot.¹ Several intermetallic compounds were identified and their structures and lattice parameters were determined. A tentative phase diagram was developed based on thermoanalytical measurements combined with x-ray diffraction and metallography results. Large homogeneous regions were observed at high temperatures for the compounds SmCo_5 and $\text{Sm}_2\text{Co}_{17}$. Recently, Buschow and Den Broeder² determined the homogeneity range in SmCo_5 using metallography. These particular samarium-cobalt intermetallic compounds are of considerable interest for permanent magnet applications. In the present study, solvus compositions for SmCo_5 , $\text{Sm}_2\text{Co}_{17}$ and samarium saturated cobalt were determined down to 800°C by electron beam microprobe analysis of the phases in annealed specimens.

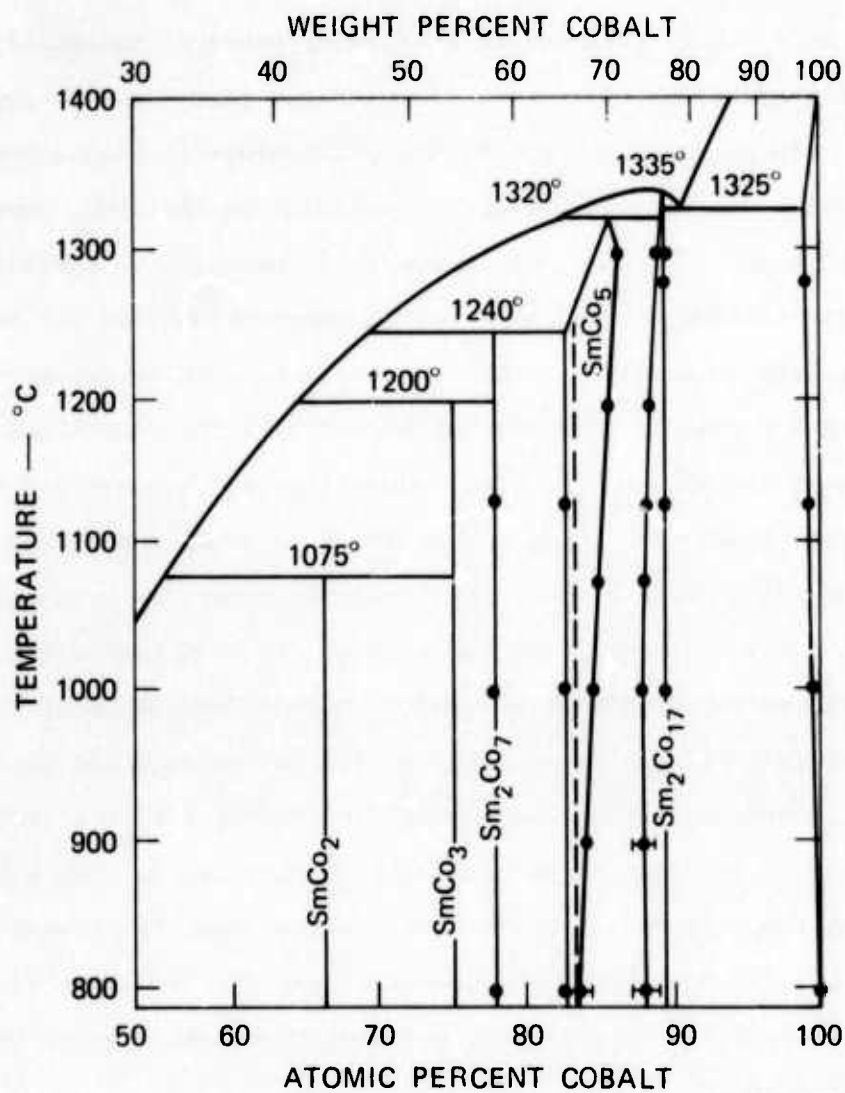
The experimental procedure consisted of arc melting samarium-cobalt alloy buttons on a cold copper hearth using a titanium gettered helium atmosphere. The alloy buttons, which weighed about 100 grams, were crushed to -80 mesh, blended, and remelted. This double melting procedure with intermediate blending was necessary to secure adequately homogeneous alloys. Alloy compositions were selected so that major proportions of two intermetallic compounds were present. Each alloy specimen was annealed at a temperature between 800 and 1300°C for a period sufficient to obtain equilibrium between the phases present. Annealing times increased as the annealing temperature decreased and times of 66 hours were used at 800°C and 900°C. Longer annealing times generally caused a reduction in the variation of measured compositions for alloy phases within the specimens

and shifted the average composition away from solvus compositions at higher temperatures toward the equilibrium compositions for the annealing temperature. The annealing was considered adequate when composition variations were minimal and when average compositions no longer shifted with increasing annealing times.

Phase compositions in the annealing experiments were determined by electron beam microprobe (EBM) analysis, using an Applied Research Laboratories' EMX-SM microprobe. Analyses were made at 15 keV, with sample currents equivalent to 0.03 microamperes on cobalt metal. Standards employed were high purity cobalt and samarium metals, with the latter being freshly polished before each analytical run to remove oxidation products. Although the spatial resolution of the microprobe is high, some difficulty was encountered because of fine grain size, particularly in runs annealed below 1000°C. Analytical areas were selected by metallographic examination and were located during analysis by scanning electron microscopy. In most cases 8 to 10 different grains of each phase were analyzed. Narrow surface zones of oxidation that formed on the surfaces of the samples during annealing or quenching were avoided, and the oxygen content was monitored throughout to ensure that analyses were not made on sporadically distributed oxide inclusions.

Microprobe intensity data were corrected for dead-time losses, background, and instrumental drift and were used to calculate "first-approximation" compositions. These showed a distinct tendency to slightly high analysis totals, mostly in the range 100-103%, and the effect was accentuated rather than offset by standard matrix correction procedures. Calibration against single phase runs indicated that the simple procedure of normalizing "first-approximation" compositions to 100% yielded relative accuracies of $\pm 1\%$, within the homogeneity range of most runs.

A revised samarium-cobalt phase diagram is shown in Figure 41. This



TA-8731-106

FIGURE 41 SAMARIUM-COBALT PHASE DIAGRAM

phase diagram was constructed from the phase diagrams previously^{1,2} published, and from the results of the EBM analyses, which are shown on Fig. 41. Except as indicated by bars, the data circles are larger than a 1-sigma confidence limit.

The SmCo_5 compound shows an increasing range of homogeneity with increasing temperature up to very close to the peritectic temperature of 1320°C .¹ This phase exhibits both hyperstoichiometric and hypostoichiometric compositions. The maximum content of samarium in the SmCo_5 compound is about 1 wt% greater than the stoichiometric composition, corresponding to the composition $\text{SmCo}_{4.8}$, and this solvus composition does not vary significantly with temperature. This result is in good agreement with Buschow and Den Broeder² and fair agreement with the variations in lattice parameters of the SmCo_5 phase with composition and temperature that have been observed by Martin, Benz, and Rockwood.³ A maximum in the coercive force or energy-product of samarium-cobalt permanent magnets occurs at a composition that coincides with the maximum samarium composition in the SmCo_5 phase, which is 82.7 at.% cobalt. Our determination of the cobalt-rich solvus in SmCo_5 is also similar to that of Buschow and Den Broeder.² The $\text{Sm}_2\text{Co}_{17}$ compound melts congruently¹ at 1335°C , and it exhibits a narrow range of homogeneity at temperatures near its melting point. The homogeneity range broadens somewhat as the annealing temperature decreases. This compound is never hyperstoichiometric and the cobalt saturated solvus is an isopleth that coincides with the stoichiometric composition of $\text{Sm}_2\text{Co}_{17}$.

Cobalt dissolves some samarium at high temperatures, about 1 at.% at 1100°C . Measured compositions for the Sm_2Co_7 phase were stoichiometric.

REFERENCES

1. K.H.J. Buschow and A. S. Van Der Goot, "Intermetallic Compounds in the System Samarium-Cobalt," J. Less-Common Metals, 14 (1968) 323.
2. K.H.J. Buschow and F.J.A. Den Broeder, J. Less-Common Metals, 33 (1973) 191.
3. D. L. Martin, M. G. Benz, and A. C. Rockwood, "Cobalt-Samarium Permanent Magnet Alloys: Variation of Lattice Parameters with Composition and Temperature, AIP Conf. Proc., 10 (1973) 583.

APPENDIX

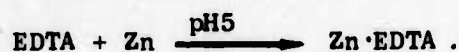
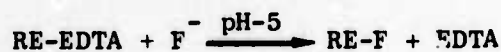
METHODS OF CHARACTERIZATION OF RARE EARTH COBALT ALLOYS AND MAGNET MATERIALS

1. Chemical Analysis of Rare Earth, Cobalt, and Rare Earth-Cobalt Alloys

The following chemical determination includes both elements and is based on the chelometric titration of the total rare earth and cobalt content with ethylene-diaminetetra-acetic acid (EDTA), and the subsequent titration of the liberated EDTA after masking the rare earth content with fluoride. The fundamental reactions are



and



a. Reagents

- (1) Acetate buffer, pH 5: Dissolve 160 g of reagent grade anhydrous sodium acetate or 270 g of the trihydrate in 500 ml water. Add 60 ml of glacial acetic acid and dilute to a liter.
- (2) Xylenol orange indicator: Dissolve 0.1 g of the indicator in 100 ml of deionized water (stable).
- (3) 0.1000 M EDTA: Dissolve 37.23 g of the disodium salt in 800 ml of deionized water in a plastic beaker and dilute to a liter. If the purity of the EDTA is not known, standardize against the zinc standard solution.

- (4) 0.02000 M zinc solution: Dissolve 1.3076 g of the pure metal in a minimum amount of hydrochloric acid and dilute to a liter.

b. Procedure

Approximately 100 to 125 mg of the alloy is weighed into a 400-ml beaker. The alloy is covered with a small quantity of water plus 2 ml of hydrochloric acid, and placed on a hot plate (low temperature) to dissolve the alloy. (Nitric acid is added if any resistance particles remain.) The solution is evaporated to dryness, and 4 ml of the buffer is added to dissolve the salt.

Approximately 300 ml of hot water plus 1/2 ml of pyridine are added, and immediately before titration with EDTA, a few crystals of ascorbic acid and five or six drops of the indicator are added. The solution is titrated to a color change from purple to yellow-orange (Titration 1). Then, approximately 0.3 of solid ammonium bifluoride plus 0.5 g of solid boric acid are introduced and dissolved. The amount of EDTA liberated is titrated with zinc solution (Titration 2). A blank should be run on all reagents. A comparison of EDTA and zinc titrants is made in the same titration beaker that contained all the contents of the determination.

c. Calculations

% Co

$$= \left\{ \left[\text{ml EDTA Titration 1} - \text{m/EDTA equiv. to m/Zn solution Titration 2} \right] \times \left[\text{molarity EDTA} \times 58.933 \text{ mg/m mole} \times 100 \right] \right\} / \text{wt of sample in mg}$$

% RE

$$= \left\{ \left[\text{m/EDTA Titration 2} \right] \times \left[\text{molarity EDTA} \times \text{atomic wt of RE} \times 100 \right] \right\} / \text{wt of sample in mg}$$

2. Procedure for Producing Magnetometer Test Specimens of Powders

Magnetometer samples are prepared by mixing the rare earth-cobalt alloy powders with a fast-setting epoxy binder. The mixture is then placed in a magnetic field for alignment while the epoxy hardens. The binder consists of eight parts by weight of Epon 826, two parts of Epon 812, and one part of Triethylenetetraamine. This mixture is placed in a vacuum dissicator for outgassing. A known quantity of rare earth-cobalt alloy powder is then mixed with the epoxy mixture and outgassed. Polyethylene tubes of 1/8 inch inside diameter and 1/4 inch length are then filled with the mixture of epoxy and KCo_5 .

The ends of the polyethylene tubes are sealed with plastic tape and placed into a sample holder within the air gap of a Varian V4004 4-inch magnet. The samples are subjected to magnetic fields of 14,000 Oe., and the temperature is raised to 40°C. The magnetic field and temperature are held constant for 16 hours to ensure setting of the epoxy. The rare earth-cobalt samples contained in epoxy are then extruded from the polyethylene tubes and are ready for measurement in the vibrating magnetometer.